Diploma Thesis

A comprehensive nanoindentation testing campaign for quantification of the stiffness distribution across tramway rail cross sections

submitted in satisfaction of the requirements for the degree of

Diplom-Ingenieur

of the TU Wien, Faculty of Civil Engineering

Diplomarbeit

Ein umfassendes Testprogramm zur Feststellung der Steifigkeitsverteilung in Querschnitten von Straßenbahnschienen, basierend auf der Methode der Nanoindentation

ausgeführt zum Zwecke der Erlangung des akademischen Grades eines

Diplom-Ingenieurs

eingereicht an der Technischen Universität Wien, Fakultät für Bauingenieurwesen

von

Valentin Jagsch, BSc

Matr.Nr.: 01126525

unter der Anleitung von

Associate Prof. Dipl.-Ing. Dr. techn. **Stefan Scheiner**

Dipl.-Ing. **Patricia Hasslinger**, BSc

Univ. Prof. Dipl.-Ing. Dr. techn. **Christian Hellmich**

Institut für Mechanik der Werkstoffe und Strukturen
Technische Universität Wien
Karlsplatz 13/202, 1040 Wien

Wien, im Oktober 2018

Kurzfassung

Straßenbahnschienen sind vielfach hohen Temperaturen ausgesetzt. Dies betrifft einerseits den Herstellungsprozess, im Zuge dessen die Widerstandsfähigkeit der Schienen gegenüber Abnützung und Ermüdung durch die gezielte Anwendung von Wärmebehandlung verbessert wird. Andererseits beinhalten Instandsetzungsmaßnahmen von im Betrieb befindlichen Schienen üblicherweise Schweißarbeiten. Letztere führen zu signifikanten, lokal einwirkenden Temperaturgradienten. Es ist bekannt, dass hohe Temperaturen zu Gefügeänderungen im Stahl führen, weswegen sich die Frage stellt, ob diese Gefügeänderungen entsprechende Steifigkeitsänderungen implizieren. Dies ist die Forschungsfrage, mit der sich die gegenständliche Arbeit beschäftigt (und welche im Rahmen eines Projekts, das vom Institut für Mechanik der Werkstoffe und Strukturen der Technischen Universität Wien in Kooperation mit der Wiener Linien GmbH & Co KG umgesetzt wird, aufgeworfen wurde).

Um die Steifigkeitsverteilung in repräsentativen Schienenstücken zu ermitteln, wurden sowohl Querschnitte aus einer neuen Schiene als auch solche von Schienen, welche im Zuge von Instandsetzungsarbeiten ersetzt wurden, herangezogen. Außerdem wurden Querschnitte untersucht, welche bei diesen Instandsetzungsarbeiten durch Hitzeeinwirkung wesentlich beeinflusst wurden und andererseits solche, bei denen dies nicht der Fall war. Des Weiteren wurden in jedem Querschnitt sechs über den Querschnitt verteilte Proben extrahiert. Zur Ermittlung der Steifigkeitsverteilungen auf den untersuchten Oberflächen der Probekörper bzw. der Verteilungen des hierfür repräsentativen Elastizitätsmoduls wurde die Methode der Nanoindentation angewendet. Zu diesem Zweck wurde für jeden der insgesamt 42 Probekörper ein Netz von 20×20 Indentationen herangezogen.

Auf den einzelnen Probekörpern zeigten sich lokal signifikant variierende Elastizitätsmoduln, was auf die unterschiedlichen Gefügearten im Schienenstahl zurückgeführt werden kann. Allerdings hat sich herausgestellt, dass keine bemerkenswerten Unterschiede zwischen Schienenstählen unterschiedlichen Alters, unterschiedlicher Vorgeschichte und unterschiedlicher Position bestehen. Daraus kann gefolgert werden, dass die Steifigkeitsverteilungen in Straßenbahnschienen homogen und zeitunabhängig sind. Es ist aber anzumerken, dass der resultierende Elastizitätsmodul von im Durchschnitt $\approx 256\,\mathrm{GPa}$ wesentlich höher ist als der üblich angenommene Richtwert von $210\,\mathrm{GPa}$.

Zukünftig werden die in dieser Studie erlangten Erkenntnisse eine wichtige Datenbasis für Strukturmodelle darstellen, welche im Rahmen der Stabtheorie entwickelt werden und zur Untersuchung des (elastischen) mechanischen Verhaltens von Straßenbahnschienen bei repräsentativen Belastungszuständen dienen.

Abstract

During their lifetime, tramway rails are subjected to heat treatment on several occasions. On the one hand, heat treatment is applied intentionally during the production process in order to make the rails more resistant to wear and fatigue. On the other hand, once installed in the tramway network, maintenance works often involve welding, leading to significant local temperature gradients. Considering that the exposure to high temperatures potentially induces changes in the steel microstructure, the question arises if and to which extent the stiffness is affected; and this is the research question dealt with in this thesis (which is an outgrowth of a collaboration of the Institute for Mechanics of Materials and Structures of the Vienna University of Technology and the Wiener Linien GmbH & Co KG).

In order to quantify the stiffness distributions across representative parts of the tramway network, cross sections have been extracted from a new tramway rail, as well as from tramway rails which had been in operation for several years and which were replaced in the course of maintenance works. Thereby, sections were extracted from both within and outside of the zone that was considerably exposed to heat. Furthermore, within each of these cross sections, six samples were considered, distributed across the cross sections, in order to study whether the stiffness exhibits significant cross-sectional variations. For quantifying the Young's modulus distribution across all samples (which was deemed representative for the stiffness, given that steel can be assumed to be isotropic) a comprehensive nanoindentation testing campaign was implemented, in the course of which a grid of 20×20 indentations was considered on each of the in total 42 samples.

On individual samples the nanoindentation-derived Young's modulus distributions do exhibit variations, which can be attributed to the material phases steel is composed of. Nevertheless, there are no significant variations across samples of different age, different history, or different location, allowing for the conclusion that the stiffness tramway rail steel is more or less homogeneous and time-invariant. However, it should be noted, that on average the Young's modulus of the tramway rail steel studied in this work amounted to $\approx 256\,\mathrm{GPa}$, which is much higher than the usually assumed ballpark figure of $210\,\mathrm{GPa}$.

In the future, the results gained in this study will serve as valuable input database for beam theory-based structural models of tramway rails, for studying their (elastic) mechanical behavior under representative loading conditions.

Danksagung

Die vorliegende Arbeit entstand im Rahmen eines Kooperationsprojekts des Instituts für Mechanik der Werkstoffe und Strukturen der Technischen Universität Wien und der Wiener Linien GmbH & Co KG. Deswegen möchte ich mich beim Projektleiter seitens der Wiener Linien GmbH & Co KG, Herrn Dipl.-Ing. Thomas Hammer (Abteilung B64, Bahnbau - Strecke Süd), für die grundsätzliche Ermöglichung dieser Arbeit, sowie insbesondere bei Herrn Karl Diehs (Abteilung B64o, Oberbauwerkstätte), der die untersuchten Schienenstücke zur Verfügung gestellt hat, bedanken.

Ebenso bedanke ich mich für die tatkräftige Unterstützung durch die MitarbeiterInnen der Technischen Universität Wien. Dabei darf ich das Institut für Mechanik der Werkstoffe und Strukturen hervorheben. Insbesondere hat mich Dipl.-Phys. Dr. techn. Olaf Lahayne tatkräftig bei der Ausführung der Nanoindentation unterstützt. Die Betreuung dieser Arbeit erfolgte durch Univ. Prof. Dipl.-Ing. Dr. techn. Christian Hellmich, Dipl.-Ing. Patricia Hasslinger, BSc und Associate Prof. Dipl.-Ing. Dr. techn. Stefan Scheiner. Durch deren Fachkompetenz und strukturierte Anweisungen war es mir erst möglich, das Themengebiet dieser Arbeit zu erschließen und erfolgreich zu erforschen. Ich bedanke mich für jegliche Bemühung in Bezug auf diese Arbeit.

Ganz besonderen Dank spreche ich dem Institut für Werkstoffwissenschaft und Werkstofftechnologie aus. Frau Edith Asiemo unterstützte mich bei den Aufbereitungsarbeiten der Stahlproben und den metallurgischen Begutachtungen der einzelnen Stahloberflächen.

Zu guter Letzt bedanke ich mich von ganzem Herzen bei meiner Familie und meinen Freunden. Die moralische Unterstützung bei der Bearbeitung solch komplexer Themengebiete, die viel Zeit und Energie benötigt, ist ein wesentlicher Punkt, um die Forschung auch erfolgreich durchführen zu können. Tausend Dank an meine Eltern, meine Geschwister und meine Freundin.

Contents

Chapter 1

Introduction

1.1 Motivation

Currently, the Institute for Mechanics of Materials and Structures of the Vienna University of Technology is involved in a research project initiated and sponsored by the Wiener Linien GmbH & Co KG (in the following, for the sake of conciseness, referred to as Wiener Linien), which is the company providing and maintaining the Viennese public transport network. This project, entitled "Investigation of the failure mechanisms relevant to the grooved rails used in the Viennese tramway network", focuses on the calculation of the mechanical stresses occurring in such rails during operation, and on finding out which loading conditions eventually lead to the development of typical crack patterns, see Fig. 1.1 for two respective examples. To that end, a numerical simulation tool is under development, conceptually based on one of *the* fundamental concepts of (civil) engineering

Fig. 1.1: Typical crack patterns occurring in grooved rails of the Viennese tramway network; (a) transverse crack in the rail head; and (b) crack pervading the rail in longitudinal direction; by courtesy of Wiener Linien

mechanics, namely on beam theory, see (Hasslinger et al., 2018) for a first outcome of these efforts.

Importantly, the aforementioned beam theory-based models require, as input quantities, the distributions of the material properties relating to the respectively studied mechanical features. For example, when studying, by means of theoretical models, the elastic material behavior, the (fourth-order) stiffness tensor of the steel of which the rails are made is the key model input quantity.[1] Considering that steel is usually regarded as isotropic material (Patnaik and Hopkins, 2004; Hellmich et al., 2015), the stiffness tensor is fully defined by the material's Young's modulus, E_{st}, and the Poisson's ratio, ν_{st}. In Kelvin-Mandel-type matrix notation, the isotropic stiffness tensor of steel reads then as (Salençon, 2012; Hellmich et al., 2015)

$$\mathbb{C}_{st} = \frac{1}{(1+\nu_{st})} \begin{pmatrix} \frac{(1-\nu_{st})E_{st}}{1-2\nu_{st}} & \frac{\nu_{st}E_{st}}{1-2\nu_{st}} & \frac{\nu_{st}E_{s}}{1-2\nu_{st}} & 0 & 0 & 0 \\ \frac{\nu_{st}E_{st}}{1-2\nu_{st}} & \frac{(1-\nu_{st})E_{st}}{1-2\nu_{st}} & \frac{\nu_{st}E_{st}}{1-2\nu_{st}} & 0 & 0 & 0 \\ \frac{\nu_{st}E_{st}}{1-2\nu_{st}} & \frac{\nu_{st}E_{st}}{1-2\nu_{st}} & \frac{(1-\nu_{st})E_{st}}{1-2\nu_{st}} & 0 & 0 & 0 \\ 0 & 0 & 0 & E_{st} & 0 & 0 \\ 0 & 0 & 0 & 0 & E_{st} & 0 \\ 0 & 0 & 0 & 0 & 0 & E_{st} \end{pmatrix}. \quad (1.1)$$

Considering now the sequence of the various processing steps rails are undergoing during the production process, as well as the maintenance measures rails are subjected to during their service life, the question arises whether the stiffness of the rail steel is position- and age-dependent or not, or, in other words whether $\mathbb{C} = \mathbb{C}(\mathbf{x}, t)$, with $\mathbf{x}$ denoting the position vector and with t donating the time variable, or $\mathbb{C} =$ constant. This is the main research question of this thesis. In the remainder of Chapter 1 some fundamental metallurgical aspects are recalled (in Section 1.2), and the particular objectives, as well as the structure of this thesis, are defined (in Section 1.3).

[1] In the simplest case, the stiffness tensor relates the stress tensor $\boldsymbol{\sigma}$ and the strain tensor $\boldsymbol{\varepsilon}$, both of which are second-order tensors, in linear fashion, through $\boldsymbol{\sigma} = \mathbb{C} : \boldsymbol{\varepsilon}$, with : denoting a second-order tensor contraction. This mathematical relation is usually called Hooke's law (Hooke, 1678; Hellmich et al., 2015), going back to the British polymath Robert Hooke (1635-1703).

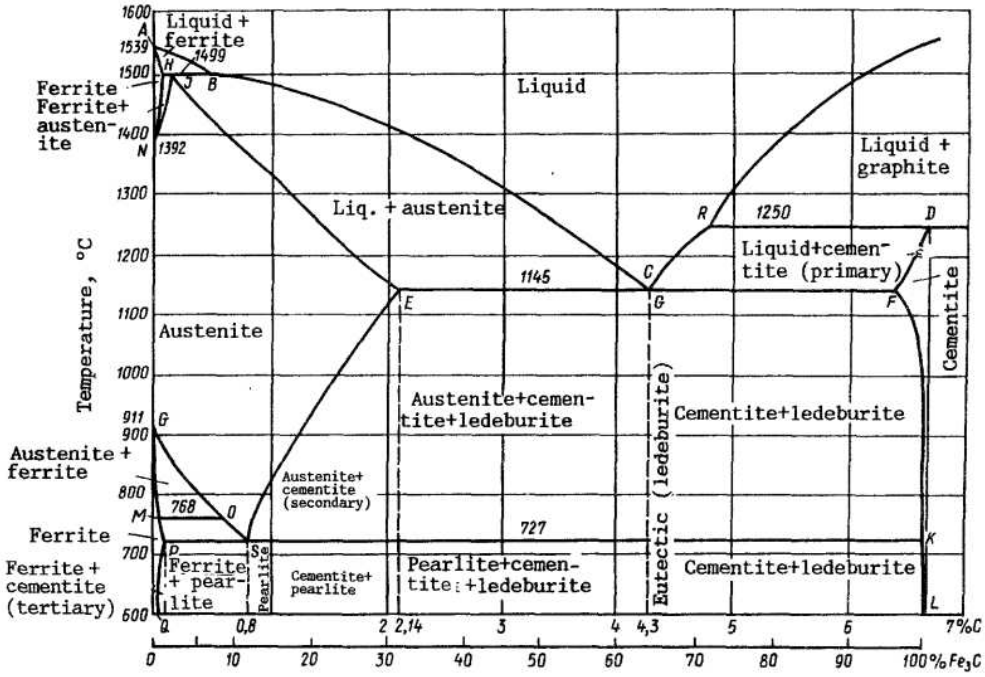

Fig. 1.2: Iron-carbon diagram, illustrating the phase composition of steel as function of the iron and carbon content, as well as of the temperature; taken from (Gulyaev, 1990)

1.2 Relevant aspects of metallurgy

This section is devoted to summarizing the metallurgical processes grooved rails are subjected to during their lifetime. Both the production process of grooved rails, as well as the quality of the final product, are standardized in ÖNORM EN 14811 2010-05-01 (Pointner et al., 2006; Austrian Standards Institute, 2010). Importantly, six steel grades are described, differing from each other in terms of chemical composition, in terms of mechanical properties and in terms of the question whether additional hardening of the rail head has been carried out, see Tab. 1.1 and 1.2. It is furthermore stated that oxygen converter steel or electric arc furnace steel is to be used as raw material for the production of the grooved rails. When using electric arc furnace steel, some secondary metallurgical processing must be performed by means of a ladle furnace; for example, steels for head-hardened grooved rails must be subjected to vacuum degassing. The rails used in the Viennese tramway network (see Tab. 1.1) are made of hypo-eutectoid steel which contains less than 0.8 wt. % carbon, see Fig. 1.2.

Next, the production process is briefly described. Standardly, the liquid steel is poured into rectangular casting blocks in continuous casting plants. These are kept at a temperature of 500-600°C, and heated to 1250°C over 2-3 hours in a walking beam furnace. The glowing block is then transported by roller conveyers to the roughing stand, where several gangways through roller pairs diminish the cross section. In the finishing stand, the final

Tab. 1.1: Chemical composition ranges defined for steel grades R200, R220G1, R260, R260GHT, R290GHT and R340GHT (which are recommended for grooved rails), according to EN 14811 2010-05-01 (Austrian Standards Institute, 2010)

steel grade	steel state	C [wt.%]	Si [wt.%]	Mn [wt.%]	P [wt.%]	S [wt.%]	H [10^{-4}wt.%]
R200	melted	0.40-0.60	0.15-0.58	0.70-1.20	<0.035	<0.035	3.0
	solid	0.38-0.62	0.13-0.60	0.65-1.25	<0.040	<0.040	3.0
R220G1	melted	0.50-0.65	0.15-0.58	1.00-1.25	<0.025	<0.025	3.0
	solid	0.48-0.67	0.13-0.60	0.95-1.30	<0.030	<0.030	3.0
R260	melted	0.62-0.80	0.15-0.58	0.70-1.20	<0.025	<0.025	2.5
	solid	0.60-0.82	0.13-0.60	0.65-1.25	<0.030	<0.030	2.5
R260GHT	melted	0.40-0.60	0.15-0.58	0.70-1.20	<0.035	<0.035	2.5
	solid	0.38-0.62	0.13-0.60	0.65-1.25	<0.040	<0.040	2.5
R290GHT	melted	0.50-0.65	0.15-0.58	1.00-1.25	<0.025	<0.025	2.5
	solid	0.48-0.67	0.13-0.60	0.95-1.30	<0.030	<0.030	2.5
R340GHT	melted	0.62-0.80	0.15-0.58	0.70-1.20	<0.025	<0.025	2.5
	solid	0.60-0.82	0.13-0.60	0.65-1.25	<0.030	<0.030	2.5

Tab. 1.2: List of mechanical properties for the steel grades R200, R220G1, R260, R260GHT, R290GHT and R340GHT (which are recommended for grooved rails), according to EN 14811 2010-05-01 (Austrian Standards Institute, 2010)

steel grade	tensile strength [MPa]	failure strain [%]	hardness on the running table [HBW]
R200	>680	>14	200-240
R220G1	>780	>12	220-260
R260	>880	>10	260-300
R260GHT	>880	>12	260-300
R290GHT	>960	>10	290-330
R230GHT	>1175	>9	340-390

profile is formed. The ends of long rails are cut afterwards, if needed, the rail head is hardened by quenching it, by making use of a water-polymer bath (where the temperature is reduced to 60°C). Then, the rail is straightened in the vertical and horizontal direction in a roller straightening machine. Finally, the rail is subjected to ultrasonics and eddy current testing, in order to examine it for internal faults. Furthermore, the shape of the profile and the surface are automatically checked for irregularities.

Iron is a polymorphic metal. This means that it occurs in different crystalline phases, see Fig 1.3. At a temperature of 1538°C, it solidifies forming crystals with a body-centered cubic (BCC) lattice. Such iron is called δ-iron, also called δ-ferrite. At 1394°C, a lattice transformation occurs to face-centered cubic (FCC) crystals, called γ-iron, or austenite. Further quenching leads to a final grid conversion. At 912°C, face-centered cubic α-iron, also called ferrite, is formed. This structure remains as the temperature continues to decrease. Furthermore, there is a inflection point at 770°C, after which α-iron becomes ferromagnetic, while at higher temperatures it is paramagnetic. The mentioned

breakpoint temperatures are valid only for very slow temperature changes and will shift significantly if the cooling process occurs fast (Weißbach, 2012).

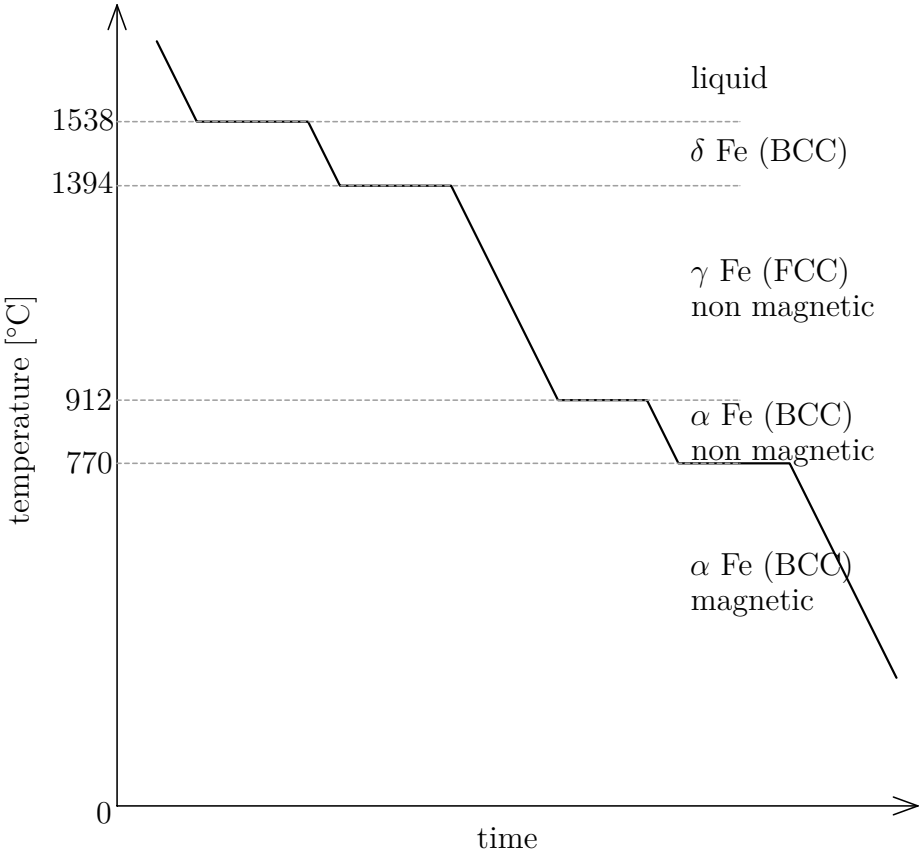

Fig. 1.3: Cooling or quenching curve of pure iron, reproduced based on (Weißbach, 2012)

Steel, in turn, is an alloy of iron and carbon (and other elements), with the phase composition defined in the so-called iron-carbon diagram, see Fig 1.2. Upon cooling of the steel, the FCC structure of the austenitic-ferritic mixture will retransform to the BCC ferritic structure. More and more ferrite lamellae grow into the austenitic body. As a result, the carbon no longer fits within the FCC structure. This results in an excess of carbon. The precipitation of the carbon is accompanied by the formation of lamellar cementite. Due to this coupled reaction of conversion and elimination the carbon saves long diffusion paths. This phase of BCC iron has so little carbon that it resembles ferrite. This lamellar structure is called pearlite. At room temperature, pearlite, which is composed of cementite and ferrite in bound form, as well as of free proeutectoidal ferrite, is then found in the structure. From a mechanical viewpoint, ferrite is soft and ductile. Additionally, it is a magnetic material. Cementite, on the other hand, is very hard but brittle. Pearlite, in turn, has ferromagnetic properties and is described as semi-hard. This suggests that ferrite is responsible for the ductility and cementite is responsible for the

strength of the rail steel (Berns, 1993; Svensson, 1994; Bhadeshia and Honeycombe, 2006; Weißbach, 2012).

Maintenance works on steel structures – and this includes also tramway rails – often involve welding. The weldability depends on the carbon content and the alloying elements. A higher carbon content is accompanied by a reduced weldability (Lippold, 2014). During the welding, a high temperature effect occurs, which decisively changes the microstructure in regions close to the actual welding site; and this potentially entails changing steel properties. The vicinity of the welding site is classified according to the temperature to which the certain site is heated up during the welding. At a temperature higher than approximately 1500°C, the steel transforms back to austenite and possibly further to δ-ferrite. This happens in regions close to the welding site. At this high temperature it may happen that this zone becomes partially melted and then resolidifies afterwards without bonding with the rest of the welded material. Further away from the welding site, the so-called heat-affected zone (HAZ) or coarse-grained zone is located. This zone is subjected to temperatures ranging from 1100 up to 1500°C. In the HAZ, a distinctive growth of the grains can be observed during the transformation to austenite. The steel behaves quite differently even further away from the welding zone, with temperatures ranging from 900 to 1100°C. Here, the grain size is relatively small and uniformly distributed. Therefore, this area is called fine-grained zone, exhibiting regular mechanical properties. Up to this zone, the high temperature results in a fully reaustenitized region. However, at temperatures around 700 to 900°C, the steel only partially transforms directly to austenite. Parts of ferrite retain, and the mechanical properties can be adversely affected. Since the transformation is only partial, the related region is called the intercritically heated zone. Finally below 700°C, there is no conversion to austenite at all – the subcritically heated zone. Below this peak temperature the area is only tempered (Hrivnak, 1992; Svensson, 1994; Hernandez et al., 2010).

A critical issue is the mechanical behavior of steel in the HAZ. It is known that strength and toughness are substantially affected (Svensson, 1994), whereas information on the influence of the HAZ on the stiffness cannot be found in literature. The strength is strongly linked to the volume fraction of martensite. Hernandez et al. (2010) claim that softening of tempered marteniste is observed, and the hardness of a ferritic phase seems to be reduced as well. Furthermore, elements in solid solution, precipitation of particles and grain size can influence the hardness of the steel. In many investigations the hardening measurements are used as an alternative to test the strength, since in most cases it is referred to as a good correlation between these two properties, see for example (Akselsen et al., 1989). Toughness has more irregularities. It is much more difficult to describe the course of toughness, which is important to prevent cracking and fracture. Knott (1973)

shows that increasing the strength arises from decreasing the toughness, although this is not always the case. For example, with smaller grain sizes, both strength and toughness are improved. This is evident by the yield strength and fracture stress. Similarly, alloys which refine the structure of the grain size have a positive effect on both properties. Furthermore, a reduction of the carbon can cause the toughness to increase while maintaining the same strength (Svensson, 1994).

Some methods influence the structure of the steel in retrospect, such as hardening. The typical procedure for hardening steel is to impose quenching, thereby inducing the formation of martensite (Haušild et al., 2011). Thereafter, tempering procedures are usually carried out. This is supposed to increase the toughness while sacrificing only little strength. To achieve this, the steel has to be quenched relatively quickly in order to not support the disintegration of austenite to ferrite, pearlite and bainite. The geometry of the head, as well as the composition of the steel, influence this process the most. Therefore, if a large diameter of a steel cross section is present, the penetration depth of the cooling will not progress as in the case of a smaller sample. So the small object would support the formation of martensite faster. The alloying elements influence not only the steel's thermal conductivity, but also the peak points of the time-temperature-transformation (TTT) curve, so that the decomposition of austenite is changed. A consequence of an inappropriate use of the cooling curve can be that the martensite formation on the surface is strongly advanced, but in the deeper regions the slower cooling leads to the accumulation of ferrite, pearlite and bainite more frequently (Bhadeshia and Honeycombe, 2006). The quenching should be carried out as fast as necessary for curing, but as slow as possible due to the otherwise impeding warpage and risk of cracks. Depending on the hardenability, the cooling process can be carried out in water, oils, or air, and may also involve cooling agents (Berns, 1993).

Apart from the so far reviewed fundamentals of metallurgy, contemporary studies in the field have revealed a large number of characteristics in steels, all of which may be relevant in the context of the mechanical behavior of grooved rails. In the following, some exemplary results are briefly summarized:

- Ray and Mondal (1991) have studied the strength of pearlite in an eutectoid steel. It appears that the strength increases while the interlamellar spacings decrease.
- Debehets et al. (2014) have shown that the different crystal types to be found in steel exhibit location varying properties. For example, the hardness of ferrite depends on the orientation of the crystals with respect to the cementite lamellae, and may, therefore, vary significantly. On the other hand, ferrite has turned out to be harder and stiffer than austenite, while both crystalline types exhibit similar yield strengths (Gadelrab et al., 2012).

- Wang et al. (2007) claim that heat treatment may affect the stiffness and the hardness of austenite and ferrite.
- Haušild et al. (2011) have revealed that compressing steel leads to a significant increase of the hardness.
- Ogi et al. (2008) have investigated duplex steels consisting of ferrite and austenite based on contact mechanics and on inducing vibrational excitation of the sample. It appears that ferrite exhibits a lower Young's modulus than austenite.
- Jirásková et al. (2005) examine, by means of microscopic methods, the structural change of rails depending on their load history. They reveal that the formation of microcracks, as well as austenitization, may occur at the originally pearlitic steel, as consequence of service conditions, including plastic deformations and local heating effects.

While the above summarized studies show only a very narrow view on the large amount of pertinent studies, it is deemed obvious that also grooved rails can be expected to undergo microstructural changes during their service life.

1.3 Objectives and structure of this thesis

For studying if and to which extent the various factors tramway rails are influenced by affect the Young's modulus distribution, a comprehensive experimental campaign was initiated. Out of the many experimental modalities available for determining elastic material properties in general, and the Young's modulus in particular, nanoindentation was considered to be the most suitable method, due to the sophistication this method has meanwhile reached, on the one hand, and due to the fact that the exact cross-sectional distribution of the Young's modulus can be derived, on the other hand. The specific objectives of this thesis are

1. Design of a reliable nanoindentation protocol;
2. Implementation of a nanoindentation campaign allowing for studying the effects of steel age, exact location, as well as history (in terms of maintenance measures) of the tested rail; and
3. Interpretation of the results in terms of the implications for beam theory-based mechanical models of grooved rails that are currently also being developed at the Institute for Mechanics of Materials and Structures of the Vienna University of Technology.

Accordingly, the remainder of this thesis is organized as outlined in the following: Chapter 2 of this thesis focuses on a brief review of nanoindentation. Chapter 3 contains the core contribution of this thesis, presented in the format of a scientific paper, entitled "Nanoindentation reveals uniform stiffness throughout grooved rails", and authored by Valentin Jagsch, Patricia Hasslinger, Olaf Lahayne, Christian Hellmich, and Stefan Scheiner, which is to be submitted to the journal "Materials Science and Engineering A – Structural Materials: Properties, Microstructure and Processing".[2] In Chapter 4, additional results are presented, which, due to the conciseness that is required in the aforementioned scientific paper, could not be considered therein. The results of this thesis are also discussed in Chapter 3, while the thesis is rounded off by some concluding remarks in Chapter 5.

[2]See https://www.journals.elsevier.com/materials-science-and-engineering-a.

Chapter 2

Nanoindentation in a nutshell

2.1 Fundamentals

The nowadays widespread method of nanoindentation originates from the classical hardness tests, with the methods according to Brinell, Vickers, Rockwell, or Meyer as most prominent examples (Broitman, 2017). Basically, these classical tests involve indentation on the macroscopic level, or, in other words, macroindentation. So-called microindentation methods can be considered as intermediate step between macro- and nanoindentation, comprising the micro-Vickers, the Knoop, and the Buchholz testing modalities (Broitman, 2017). While all tips used in indentation testing are, of course, very hard, consequently composed of mostly diamond-like materials (with well-defined mechanical properties), the experimental setups of the mentioned (and similar) methods differ from each other mainly in terms of the shape of the indenter tip – including spherical, spheroconical, and pyramid-like shapes. Irrespective of the employed method, the material hardness H follows from the following mathematical relation (Broitman, 2017):

$$H = \frac{P_{max}}{A_r}\,, \tag{2.1}$$

where A_r is the residual indentation area, and P_{max} is the maximum force applied during the indentation protocol. Notably, A_r is determined based on inspecting the indented region visually, by means of light microscopy. Hence, due to varying resolutions of different light microscopes, the accuracy of hardness measurements varies accordingly.

Nanoindentation protocols, in turn, have been refined such that the obtained results are considered to be extremely accurate. In particular, usually a Berkovich-tip is used (Berkovich, 1951), being of the shape of a three-sided pyramid. Given that the geometry of the tip is well-defined, and that the indentation depth (with a characteristic length in the range of 10^{-6} to 10^{-9} m) is recorded very precisely, the indentation area can be calculated precisely as well. Furthermore, the applied force is typically in the range of

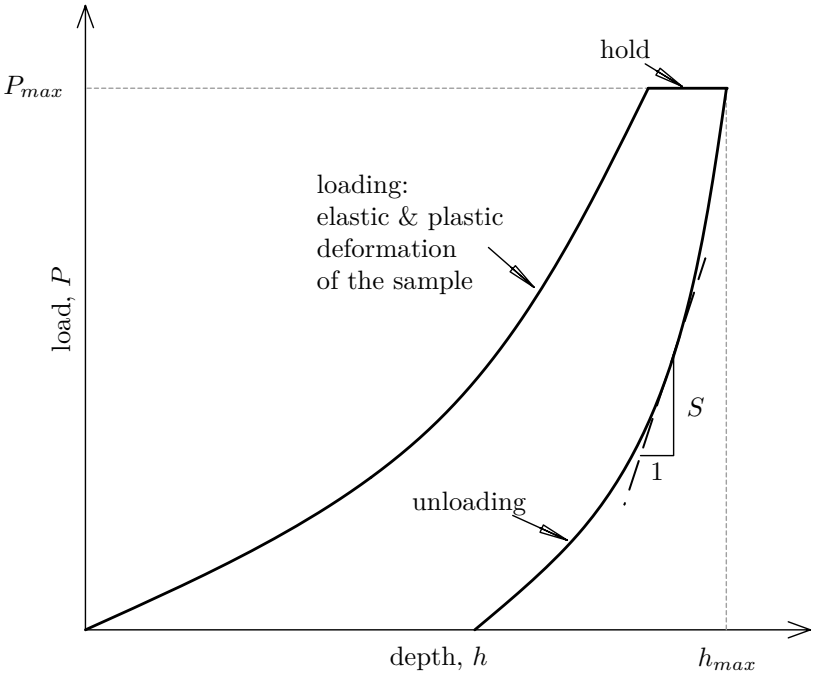

Fig. 2.1: A typical load-displacement curve considered in nanoindentation tests, reproduced based on Hou et al. (2016)

several 10^{-3} N. Due to the small characteristic lengths of the nanoindents, it is possible to determine the spatial distribution of material properties across the studied samples.

2.2 Classical analysis of nanoindentation results

Correct analysis of nanoindentation tests has kept the field busy for quite some time, see, for example, the seminal works of (Sneddon, 1965; Doerner and Nix, 1986; Oliver and Pharr, 1992). Eventually, Oliver and Pharr have presented a method which has been readily embraced by the scientific community ever since (Pharr and Bolshakov, 2002; Oliver and Pharr, 2004). Namely, considering a typical nanoindentation protocol, see Fig. 2.1, the unloading path of the load-displacement curve is considered, in order to calculate the contact stiffness S (Hou et al., 2016),

$$S = \frac{\mathrm{d}P}{\mathrm{d}h}\,, \tag{2.2}$$

where P is the applied force, h the penetration depth, and d the differential operator. Based on the contact stiffness, the so-called reduced Young's modulus E_r can be determined (Oliver and Pharr, 2004),

$$S = \beta\frac{2}{\sqrt{\pi}}E_r\sqrt{A_p(h_c)}\,, \tag{2.3}$$

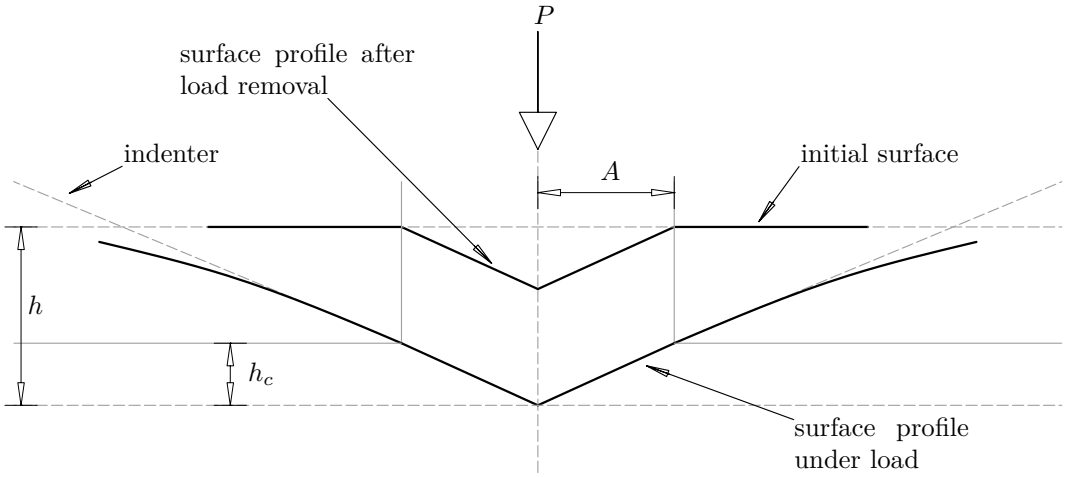

Fig. 2.2: Schematic illustration of an indent, reproduced from Oliver and Pharr (1992)

where β is a geometrical constant, h_c is the contact depth, see Fig. 2.2, and $A_p(h_c)$ is the projected area relating to the contact depth. Obviously, Eq. (2.3) can be straightforwardly rearranged for determination of E_r,

$$E_r = \frac{S\sqrt{\pi}}{2\sqrt{A_p(h_c)}}, \tag{2.4}$$

with S following from analysis of nanoindentation data, according to Eq. (2.2). Notably, the *reduced* Young's modulus takes into account that both the tip and the tested material show elastic behavior, through the following relation (Oliver and Pharr, 2004):

$$\frac{1}{E_r} = \frac{1-(\nu_{sample})^2}{E_{sample}} + \frac{1-(\nu_{tip})^2}{E_{tip}}, \tag{2.5}$$

where E_{sample} and ν_{sample} are the Young's modulus and the Poisson's ratio of the tested sample, whereas E_{tip} and ν_{tip} are the Young's modulus and the Poisson's ratio of the indentation tip. For a standard diamond tip, the latter values read as $E_{tip} = 1140\,\mathrm{GPa}$ and $\nu_{tip} = 0.07$. Rearranging Eq. (2.5) yields

$$E_{sample} = \frac{1-\nu_{sample}^2}{\dfrac{1}{E_r} - \dfrac{1-\nu_{tip}^2}{E_{tip}}}. \tag{2.6}$$

2.3 Statistical analysis of nanoindentation results

Next, it is considered now that not just one but many nanoindentation tests have been carried out for studying the Young's modulus within a predefined area, thereby considering a respective grid of nanoindents. Such an approach, apart from providing the

spatial distribution of Young's moduli, calls for utilizing statistical methods, in order to improve the significance of the gained results. This strategy was driven forward mainly by Ulm an co-workers (Constantinides et al., 2006; Constantinides and Ulm, 2007; Ulm et al., 2007), and later also by other groups, see, for example (Kim et al., 2012), whereas the works of Kariem et al. (2015) and Furin et al. (2016), building on the basis laid by Ulm and co-workers, presented new ideas in terms of interpretation of the results. Section 3.5 contains a brief summary of the concept of statistical nanoindentation, as utilized in this thesis.

2.4 Further application modes

Besides the Young's modulus, nanoindentation can also be utilized for calculating the hardness distribution across the tested sample, by evaluating Eq. (2.1), with the contact area following from atomic force microscopy or scanning electron microscopy.

Furthermore, nanoindentation has been used to determine the hardness as function of the depth (Oliver and Pharr, 1992). Then, the relevant test parameters are recorded quasi-continuously. Varying parameters such as loading and unloading speed allows to reveal certain hardness characteristics (Ladani et al., 2013). Moreover, nanoindentation has been shown to be utilizable for studying the plastic flow behavior of materials (Chatterjee et al., 2014), the yield strength (Juliano et al., 2007), the viscoelastic material behavior (Jäger, 2008), and even for determination of residual stresses (Dean et al., 2011; Boccaccio et al., 2013).

Chapter 3

Scientific paper to be submitted to *Materials Science and Engineering A*

Chapter 3 of this thesis presents a scientific paper, entitled "Nanoindentation reveals uniform stiffness throughout grooved rails", and authored by Valentin Jagsch, Patricia Hasslinger, Olaf Lahayne, Christian Hellmich, and Stefan Scheiner, which is to be submitted to the journal "Materials Science and Engineering A – Structural Materials: Properties, Microstructure and Processing".[1]

3.1 Introduction

Before being installed in tramway, underground, or railroad networks, rails undergo a series of processing steps. Often, these processing steps include heat treatment (Svensson, 1994; Bhadeshia and Honeycombe, 2006; Weißbach, 2012), in order to improve certain characteristics of the rail (by correspondingly influencing its microstructure), such as the toughness or the hardness (Akselsen et al., 1989; Svensson, 1994; Hernandez et al., 2010), and to thereby reduce the susceptibility of the rail to wear. Furthermore, rails are subjected, in the course of their lifetime, to maintenance works, in order to repair damaged areas, or to even replace whole sections of a rail track by new rails. In many cases, these measures involve welding. The thereby applied high temperatures may also lead, in the vicinity of the welding site, to microstructural changes in the rail (Hrivnak, 1992; Svensson, 1994; Hernandez et al., 2010).

One of the most important mechanical properties of structural members in general, and of rails in particular, is the mechanical stiffness (as this is the property governing the extent of elastic deformations occurring in response to mechanical loading). The question arises whether and to which extent the aforementioned, temperature-induced microstructural changes in the rail steel influence the stiffness of the rail steel. Restricting ourselves to

[1] See https://www.journals.elsevier.com/materials-science-and-engineering-a.

tramway rails, this is actually the research question which is addressed in the present paper.

Considering the nowadays available experimental methods which could be utilized for quantifying the spatial distribution of the stiffness in structures such as (tramway) rails, nanoindentation appears to be a reasonable (if not the obvious) choice. Actually, nanoindentation has been applied in the (recent) past in similar studies. For example, Pham et al. (2014) managed to distinguish, based on nanoindentation, between the different material phases of which SS400 steel is composed. Interestingly, Pham et al. (2014) found distinctive stiffness differences between tested regions and the therein contained material phases; they report Young's moduli ranging from 206 to 358 GPa, see also (Pham and Kim, 2015a; Pham and Kim, 2015b). Hence, their results somehow contradict the standard textbook specification in terms of the stiffness of the different crystal types encountered in steel (Brenner, 1956; Schröder, 1985; Bhadeshia and Honeycombe, 2006; Kim and Johnson, 2007; Totten, 2008), which typically vary within a much narrower range, namely between 208 to 214G̃Pa.

In this paper we study the stiffness distributions across samples extracted from tramway rails of different age, from different sites, and with different histories. The selection and preparation of the samples studied by means of nanoindentation are described in Section 3.2.1. The applied experimental methods, namely light microscopy, nanoindentation, and scanning probe microscopy, are presented in sufficient detail in Sections 3.2.2 to 3.2.4. The results are presented in Section 3.3 and discussed in Section 3.4, including also some concluding remarks.

3.2 Materials and methods

3.2.1 Sample selection and preparation

In this study exclusively grooved rails of profile 210/95+80(60R3) and steel grade S800/R220G1 (Austrian Standards Institute, 2010) were considered. In particular, approximately 1 cm thick sections were cut out by means of a Jet MBS-910CS bandsaw, from four, approximately 1 m long rail sections. Three of the latter were extracted from the Viennese tramway network in the course of maintenance works (cut out by means of a TMJ semi-automatic bandsaw PP 620DG), and one from a factory-fresh rail (by means of oxyacetylene cutting). In order to study the effects of previous maintenance measures on the corresponding stiffness distributions, two sections were extracted from each of the rail pieces that have been in operation before; one located in the heat-affected zone (HAZ), and one located outside the HAZ. The differences between the rail sections that were con-

sidered for the subsequently presented tests are summarized in Tab. 3.1. Six samples were cut out of each of the rail sections defined in Tab. 3.1, by means of a precision diamond saw, see Fig. 3.1 for the locations of the samples. In the following, specimens are referred to in the format section number-sample number; for example, specimen II-4 relates to sample 4 (see Fig. 3.1) of rail section II (see Tab 3.1).

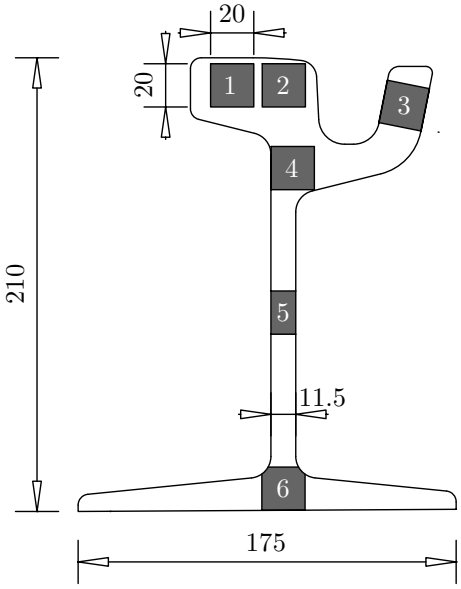

Fig. 3.1: Locations of investigated samples, distributed across 1 cm thick rail sections (as defined in Tab. 3.1) of profile 210/95+80(60R3)

First, the studied surfaces of the samples were coarsely ground, using abrasive belts and grinding wheels with grain sizes of 60 to 180, in order to remove surface irregularities. Subsequently, the surfaces were ground and polished, respectively, by means of a Struers RotoPol 31 grinder/polisher. In order to adequately mount the samples in the polisher, the samples were embedded in a LevoFast resin. The grinding of the sample surfaces

Tab. 3.1: Definition of the investigated rail sections, clarifying age, previous maintenance measures the rail was subjected to whether the particular section was located in the heat-affected zone (HAZ) or not, and the eventual cause of removal; rail section V was factory-fresh

section #	age [years]	maintenance	location	cause of removal
I	45	manual welding	not HAZ	crack in the head
II	45	manual welding	HAZ	crack in the head
III	10	thermite welding	not HAZ	crack in the head
IV	10	thermite welding	HAZ	crack in the head
V	-	-	-	-
VI	39	thermite welding	not HAZ	crack in the web
VII	39	thermite welding	HAZ	crack in the web

Tab. 3.2: Grinding steps carried out sequentially for preparing sample surfaces

grain size	time [min]	direction of rotation	rotations per minute	force [N]
80	3	counter-clockwise	300	150
120	3	clockwise	300	150
180	3	clockwise	300	150
320	4	clockwise	300	180
500	4	clockwise	150	180
1000	2	clockwise	150	180

Tab. 3.3: Polishing steps carried out sequentially for preparing sample surfaces

grain size [μ]	suspension metering	lubricant metering	time [min]	force [N]	direction of rotation	rotations per minute
9 Allegro	5	12	6	200	counter-clockwise	150
9 Lagro	8	16	6	180	clockwise	150
6 Dur	7	14	6	180	clockwise	150
3 Mol	7	14	10	150	clockwise	150
1 Nap	7	14	10	130	clockwise	150

was carried out as step-wise process, see Tab. 3.2 for the respective specification of each grinding step. Between the grinding steps, the samples were cleaned using a water/soap solution in an ultrasonic bath, after which the surfaces were sealed using ethanol, in order to minimize surface corrosion. Eventually, the surfaces underwent a polishing sequence, by means of diamond-impregnated polishing cloths, using also suspension and lubricant. The polishing was again carried out in step-wise fashion, see Tab. 3.3 for the specifications of each polishing step. Between all grinding and polishing steps, the respectively strived after fineness was carefully checked by means of a light microscope.

3.2.2 Microstructure evaluation by means of light microscopy

In order to visually assess the sample surfaces, the surfaces were first etched by means of nital, a solution of alcohol and nitric acid (whereby the latter was added at 2 wt. %). The such prepared surfaces were mounted into a Zeiss Axio Imager M2m microscope, and magnification factors were set within a range of 5 to 100. The recording of the images was performed by means of a Zeiss AxioCam MRc5 camera.

3.2.3 Nanoindentation testing

3.2.3.1 Experimental protocol

Nanoindentation was carried out on the unetched sample surfaces, prepared as described in Section 3.2.1, by means of a Hysitron Triboindenter TI900, using a Berkovich diamond

tip. In order to ensure optimal comparability, with respect to previously performed, similar studies (Pham et al., 2014; Pham et al., 2015; Pham and Kim, 2015a; Pham and Kim, 2015b; Zhu et al., 2010; Hernandez et al., 2010), the nanoindentation was carried out in the following way: The samples were indented in load-controlled fashion, at a load rate of 0.2 mN/s, until a maximum load of 6 mN was reached. After holding the maximum load for 3 s, unloading was performed, again at a rate of 0.2 mN/s, see Fig. 3.2 for an exemplary load history and load-displacement diagram.

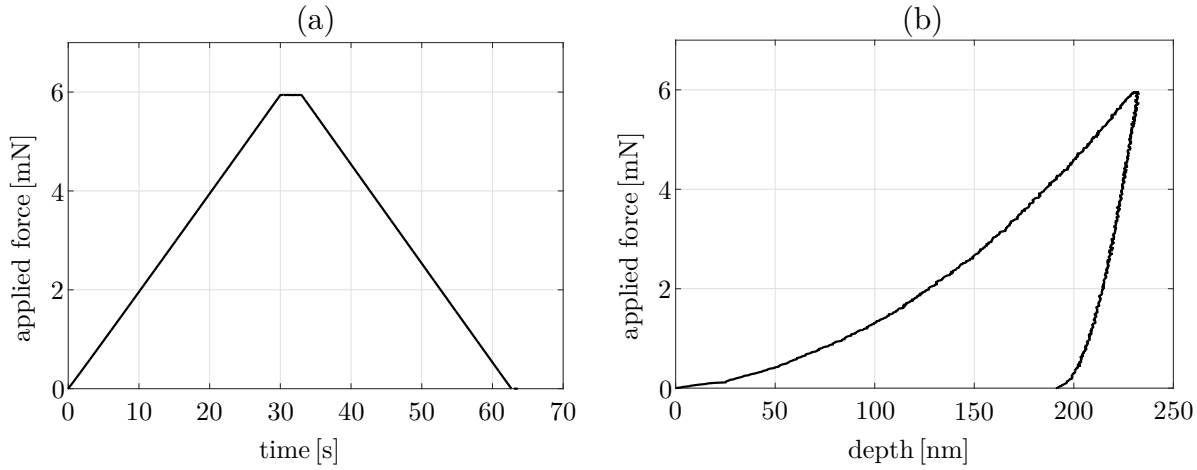

Fig. 3.2: (a) Load history and (b) load-displacement curve of one exemplary indentation test (carried out on specimen I-4) of this nanoindention testing campaign

The above-desired loading protocol was carried out on a grid of 20 × 20 indents, considering a grid spacing of 0.5 mm. In order to minimize the impact of potential boundary effects the grid of indents was positioned centrally on the sample surfaces, see Fig. 3.3.

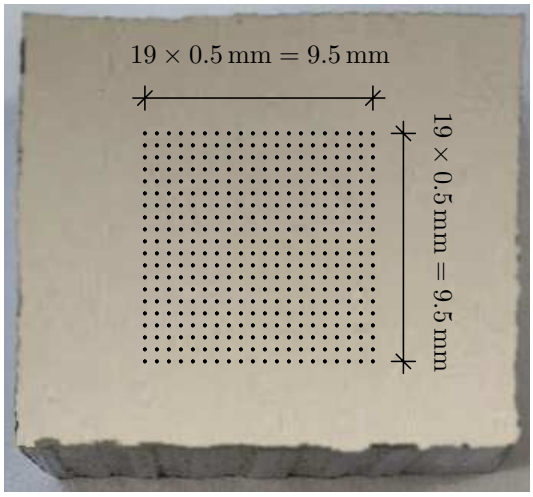

Fig. 3.3: Distribution of the indents on the specimen, according to a regular 20 × 20 grid

3.2.3.2 Analysis of nanoindentation data

In this work, the classical approach of Oliver and Pharr (1992) was utilized, yielding from each nanoindentation test a corresponding Young's modulus of the sample at grid point i, $E_{sample,i}$; hence $i = 1...N_{sample} = 400$. Considering the such obtained Young's moduli of all 400 grid points per sample, a corresponding probability density distribution can be derived.

Inspired by the pioneering works in the field of grid or statistical nanoindentation (Constantinides et al., 2006; Constantinides and Ulm, 2007; Ulm et al., 2007), and following more recent interpretations thereof (Kariem et al., 2015; Furin et al., 2016), a probability density function of the acquired Young's moduli was interpreted as superposition of several Gaussians, each of which represents a specific material phase (whereby a material phase can be also interpreted as certain degree of material damage). To that end, making use of an evolution algorithm (Schwefel, 1977; Weicker, 2007; Jaindl et al., 2009) was implemented. The underlying concept is briefly summarized in Section 3.5 of this paper.

3.2.4 Analysis of roughness

The Hysitron Triboindenter TI900 also allows to determine the surface roughness of the indented samples, based on scanning probe microscopy, see, for example, Gadelmawla et al. (2002) or Furin et al. (2016) for details.

3.3 Results

Before presenting the nanoindentation-derived distributions of Young's moduli, it should be emphasized that the roughness scans have revealed that the surface roughness is, throughout all tested surfaces, at least forty times below the penetration depth of the indenter. Hence, it can be assumed that all surfaces were sufficiently fine, according to the commonly applied criterion (Laurent-Brocq et al., 2015) that the ratio of the surface roughness over the nanoindentation depth should be lower than 0.05.

Next, the results gained for one particular, exemplary specimen are described in detail. For that purpose, specimen V-6 is considered, see Fig. 3.1 and Tab. 3.1. The direct output of the nanoindentation tests is the hardness distribution across the tested area, and, following the work of Oliver and Pharr (1992), the corresponding distribution of Young's moduli, see Fig. 3.4. Alternatively, the distribution of Young's moduli shown in Fig. 3.4 can be illustrated in terms of the corresponding probability density function, see the bar-type probability distribution in Fig. 3.5. Making use of the concept of statistical nanoindentation analysis, see Section 3.5, the corresponding cumulative distribution

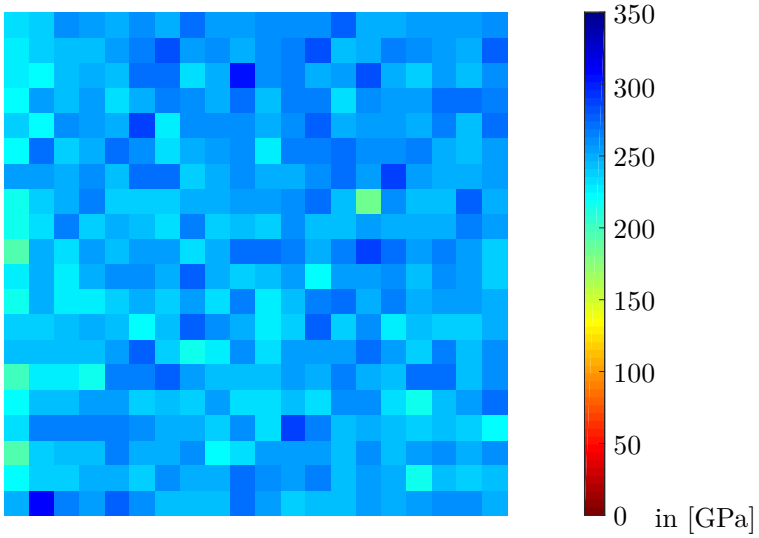

Fig. 3.4: Nanoindentation-derived distribution of the Young's modulus across specimen VII-3

function is then fitted based on one or the sum of several Gaussian distributions. Fig. 3.5 shows the result of this fitting procedure. On the one hand, the red solid line represents the probability density function related to one Gaussian distribution (with a mean value of $\mu_{VII\text{-}3}^{1peak} = 249.9\,\mathrm{GPa}$, a standard deviation $\sigma_{VII\text{-}3}^{1peak} = 14.9\,\mathrm{GPa}$, and a relative error of

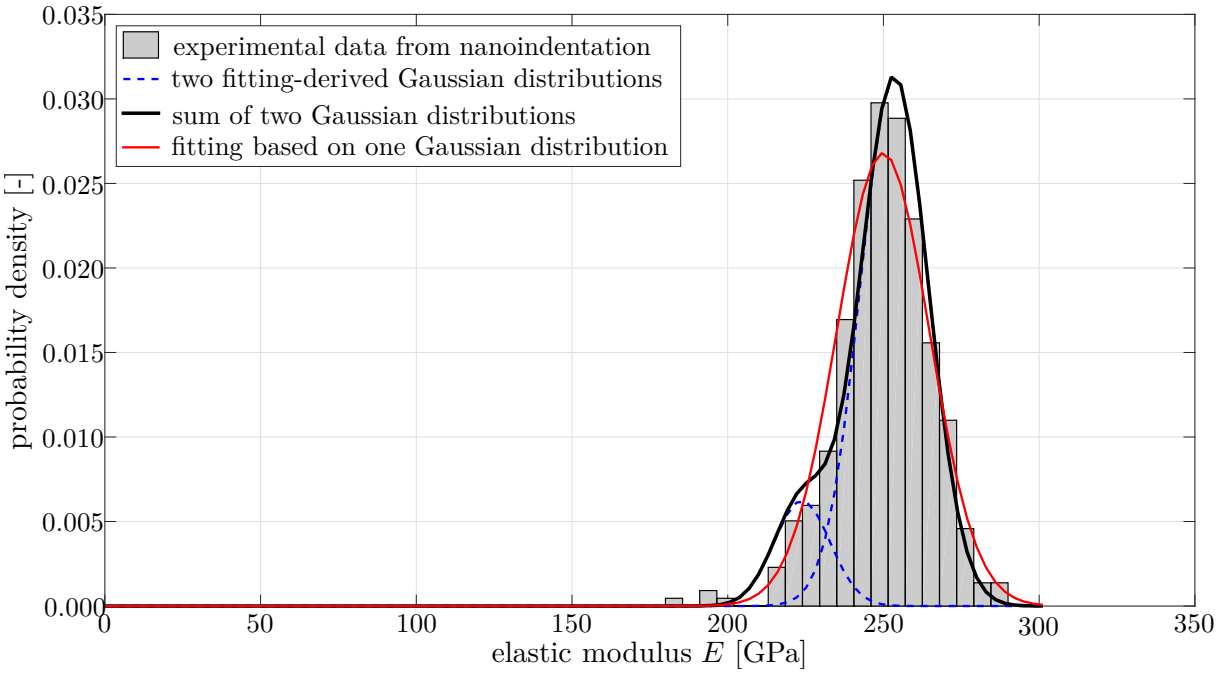

Fig. 3.5: Probability density function of the Young's moduli obtained by means of nanoindentation on specimen VII-3, sorted into 5.45 GPa-wide groups (grey bars); the optimal theoretical fit of the experimental data follows from summing up two Gaussian distributions, see Section 3.5 – the best overall fit is shown as solid black line, while the underlying Gaussian distributions are shown as dashed blue lines – and the fit of the experimental data by just one Gaussian distribution is shown as solid red line

$\mathcal{E}^{1peak}_{rel,VII\text{-}3} = 1.534$). On the other hand, the thin dashed lines represent the optimal fit, comprising in this particular case 2 Gaussian distributions, and the thick solid line represents the sum of these 2 distributions. Thereby, the first distribution is characterized by a mean value of $\mu_{VII\text{-}3,1} = 223.9\,\text{GPa}$, a standard deviation of $\sigma_{V\text{-}6,1} = 9.0\,\text{GPa}$, and a weighing factor of $f_{VII\text{-}3,1} = 0.141$, whereas the second distribution is characterized by a mean value of $\mu_{VII\text{-}3,2} = 253.5\,\text{GPa}$, a standard deviation of $\sigma_{VII\text{-}3,2} = 10.9\,\text{GPa}$, and a weighing factor of $f_{VII\text{-}3,2} = 0.859$). The overall mean value amounts to $\bar{\mu}_{VII\text{-}3} = 253.5\,\text{GPa}$, the standard deviation to $\bar{\sigma}_{VII\text{-}3} = 10.9\,\text{GPa}$, and the corresponding relative error of $\bar{\mathcal{E}}_{rel,VII\text{-}3} = 0.353$.

Analogously, we proceeded with each of the tested specimens. For the sake of conciseness, we present the obtained results in tabular format, see Tab. 3.4, 3.5 and 3.6, but omit presenting the underlying probability density functions.

Furthermore, the same analysis modality was applied to the following groups and specific subsets of Young's moduli among all performed nanoindentation tests:

- seven subsets each of which represents one specific cross section;
- six subsets each of which represents one specific sample;
- three subsets one of which comprises all results from cross sections I and II, one all results from cross sections III and VI, and one all results from cross sections VI and VII;
- two subsets distinguishing between samples located in the HAZ and not located in the HAZ; and
- the entirely of all nanoindentations at once.

The obtained results are summarized in Tab. 3.7 as well as in Figs. 3.6 and 3.7.

Tab. 3.4: Number of Gaussians needed to obtain optimal fit, N_{ph}, see Section 3.5, the overall mean value of the specimen-specific Young's modulus, $\bar{\mu}_{k\text{-}l}$, the corresponding standard deviation, $\bar{\sigma}_{k\text{-}l}$, and the relative error related to the optimal fit, $\bar{\mathcal{E}}_{rel,k\text{-}l}$; index k denotes the section number, $k = I, ..., VII$, and index l the sample number $l = 1, ..., 6$

specimen	N_{ph}	$\bar{\mu}_{k\text{-}l}$ [GPa]	$\bar{\sigma}_{k\text{-}l}$ [GPa]	$\bar{\mathcal{E}}_{rel,k\text{-}l}$ [%]
I-1	3	277.5	8.0	0.483
I-2	2	236.9	44.3	0.301
I-3	2	261.5	42.9	1.490
I-4	2	248.1	12.6	0.430
I-5	3	245.9	11.6	0.223
I-6	2	264.9	11.2	0.034
II-1	4	261.8	11.4	0.406
II-2	3	264.7	9.2	0.139
II-3	2	236.7	24.1	0.013
II-4	2	256.5	19.2	0.076
II-5	3	247.7	11.0	0.184
II-6	3	256.2	10.0	0.177
III-1	4	245.7	6.5	0.352
III-2	3	243.7	16.2	1.906
III-3	2	254.1	12.4	0.089
III-4	3	259.1	76.4	0.043
III-5	3	272.3	10.8	0.061
III-6	3	256.7	9.6	0.217
IV-1	4	251.5	8.4	0.334
IV-2	3	251.3	16.2	0.376
IV-3	4	236.1	10.6	0.576
IV-4	3	249.2	10.1	0.135
IV-5	3	237.5	9.6	0.454
IV-6	4	236.1	10.6	0.241
V-1	4	257.0	7.2	0.824
V-2	2	244.0	28.2	0.787
V-3	2	237.0	37.2	0.291
V-4	2	238.9	42.3	0.593
V-5	2	256.6	49.9	0.036
V-6	2	229.6	13.5	0.136
VI-1	2	274.7	39.9	0.344
VI-2	3	307.1	18.4	0.106
VI-3	3	272.3	12.3	0.509
VI-4	4	279.1	8.2	0.100
VI-5	2	257.7	15.7	1.504
VI-6	2	265.3	41.7	0.049
VII-1	2	255.4	16.2	0.044
VII-2	4	262.8	12.1	0.183
VII-3	2	253.5	10.9	0.353
VII-4	2	252.6	28.5	0.768
VII-5	3	267.8	10.7	0.020
VII-6	2	271.6	12.9	0.155

Tab. 3.5: Mean values ($\mu_{k\text{-}l,j}$), standard deviations ($\sigma_{k\text{-}l,j}$), and weighing factors ($f_{k\text{-}l,j}$) obtained for all tested specimens through the fitting procedure described in Section 3.5, and relating to the overall mean values, standard deviations, and relative errors given in Table 3.4; index k denotes the section number, $k = I, ..., VII$, index l the sample number $l = 1, ..., 6$, and index j the Gaussian distribution, $j = 1, ..., N_{ph}$

specimen	$\mu_{k\text{-}l,j}$ [GPa]				$\sigma_{k\text{-}l,j}$ [GPa]				$f_{k\text{-}l,j}$ [GPa]			
I-1	214.6	255.4	277.5		7.7	7.8	8.0		0.034	0.416	0.549	
I-2	124.4	236.9			44.3	18.3			0.007	0.993		
I-3	87.1	261.5			42.9	19.8			0.001	0.999		
I-4	214.6	248.1			12.6	11.8			0.171	0.829		
I-5	164.9	219.5	245.9		11.4	11.6	9.3		0.030	0.237	0.733	
I-6	235.1	264.9			11.2	10.5			0.223	0.777		
II-1	186.5	217.4	240.7	261.8	11.4	6.8	8.1	7.3	0.019	0.139	0.606	0.235
II-2	202.0	241.2	264.7		9.0	8.5	9.2		0.024	0.319	0.657	
II-3	160.2	236.7			24.1	16.4			0.028	0.972		
II-4	177.6	256.5			19.0	19.2			0.009	0.991		
II-5	180.5	214.3	247.7		6.1	9.7	11.0		0.030	0.245	0.724	
II-6	202.7	230.6	256.2		3.1	10.0	8.9		0.025	0.436	0.538	
III-1	186.5	207.4	227.7	245.7	3.6	6.5	6.4	6.0	0.041	0.137	0.612	0.211
III-2	102.6	185.7	243.7		11.2	16.2	12.7		0.022	0.035	0.944	
III-3	224.9	254.1			12.4	11.1			0.286	0.714		
III-4	93.9	194.2	259.1		76.4	4.1	16.1		0.015	0.011	0.974	
III-5	203.3	243.1	272.3		10.8	9.9	10.0		0.085	0.527	0.388	
III-6	193.6	235.2	256.7		9.6	7.9	8.1		0.060	0.537	0.403	
IV-1	174.3	196.4	229.1	251.5	2.6	7.1	8.4	8.3	0.051	0.051	0.398	0.493
IV-2	171.8	220.9	251.3		16.2	12.1	10.9		0.012	0.211	0.777	
IV-3	147.4	168.7	210.2	236.1	9.3	10.6	9.7	9.7	0.033	0.033	0.401	0.533
IV-4	187.2	224.4	249.2		5.9	10.1	9.4		0.015	0.358	0.627	
IV-5	175.8	212.3	237.5		4.9	9.0	9.6		0.031	0.283	0.686	
IV-6	147.3	168.6	208.7	236.1	9.3	10.6	9.9	9.5	0.016	0.020	0.421	0.542
V-1	193.3	216.3	238.4	257.0	5.0	7.2	6.6	5.6	0.066	0.136	0.507	0.291
V-2	136.8	244.0			28.2	17.7			0.023	0.977		
V-3	55.7	237.0			37.2	16.7			0.001	0.999		
V-4	92.9	238.8			42.3	19.8			0.006	0.994		
V-5	119.3	256.6			49.9	20.0			0.005	0.995		
V-6	200.7	229.6			13.5	9.9			0.198	0.802		
VI-1	59.9	274.7			39.9	21.3			0.017	0.983		
VI-2	227.4	252.3	307.1		4.9	9.1	18.4		0.031	0.018	0.951	
VI-3	196.9	246.2	272.3		12.3	8.7	9.8		0.044	0.497	0.459	
VI-4	198.4	229.9	257.0	279.1	5.5	8.2	8.0	6.9	0.073	0.146	0.532	0.250
VI-5	207.9	257.7			15.7	14.1			0.115	0.885		
VI-6	150.8	265.3			41.7	18.0			0.001	0.999		
VII-1	198.7	255.4			6.0	16.2			0.031	0.969		
VII-2	183.4	212.3	240.0	262.8	12.1	7.4	8.9	7.7	0.064	0.152	0.504	0.280
VII-3	223.9	253.5			9.0	10.9			0.141	0.859		
VII-4	94.3	252.6			28.5	17.5			0.005	0.995		
VII-5	195.9	240.7	267.8		9.8	10.0	10.7		0.050	0.268	0.682	
VII-6	230.0	271.6			12.9	12.9			0.117	0.883		

Tab. 3.6: Mean values ($\mu_{k\text{-}l}^{1peak}$), standard deviations ($\sigma_{k\text{-}l}^{1peak}$), and relative errors ($\mathcal{E}_{k\text{-}l}^{1peak}$) for all tested specimens through the fitting procedure described in Section 3.6, when restricting the fitting to only one Gaussian distribution; index k denotes the section number, $k = I, ..., VII$, and index l the sample number $l = 1, ..., 6$

specimen	$\mu_{k\text{-}l}^{1peak}$ [GPa]	$\sigma_{k\text{-}l}^{1peak}$ [GPa]	$\mathcal{E}_{rel,k\text{-}l}^{1peak}$ [%]
I-1	265.4	18.7	0.627
I-2	234.8	25.0	1.697
I-3	258.8	30.6	9.295
I-4	243.0	17.2	2.204
I-5	238.1	20.8	2.254
I-6	258.7	16.5	0.284
II-1	240.5	21.4	3.710
II-2	255.9	17.2	5.668
II-3	234.1	22.4	2.440
II-4	253.5	25.2	3.818
II-5	237.3	24.6	6.316
II-6	242.8	23.2	6.712
III-1	226.3	21.4	5.081
III-2	238.5	25.4	13.359
III-3	246.4	17.7	0.117
III-4	254.8	29.0	5.586
III-5	251.1	22.9	1.761
III-6	241.4	18.2	2.767
IV-1	236.0	25.6	7.783
IV-2	244.2	20.1	6.854
IV-3	221.3	23.2	5.327
IV-4	239.4	17.6	5.062
IV-5	229.2	17.0	3.054
IV-6	221.8	21.1	5.694
V-1	239.0	16.3	4.712
V-2	242.4	22.9	2.307
V-3	234.5	27.5	7.938
V-4	236.2	29.5	1.490
V-5	254.3	27.4	0.756
V-6	224.5	17.5	1.501
VI-1	266.2	36.3	3.466
VI-2	298.1	36.7	2.194
VI-3	255.4	21.7	4.541
VI-4	254.8	23.6	2.574
VI-5	252.3	21.4	7.322
VI-6	263.1	25.6	2.022
VII-1	253.3	20.3	1.524
VII-2	239.1	24.2	3.381
VII-3	249.9	14.9	1.534
VII-4	250.4	26.8	6.721
VII-5	257.0	25.9	4.433
VII-6	265.5	25.5	2.808

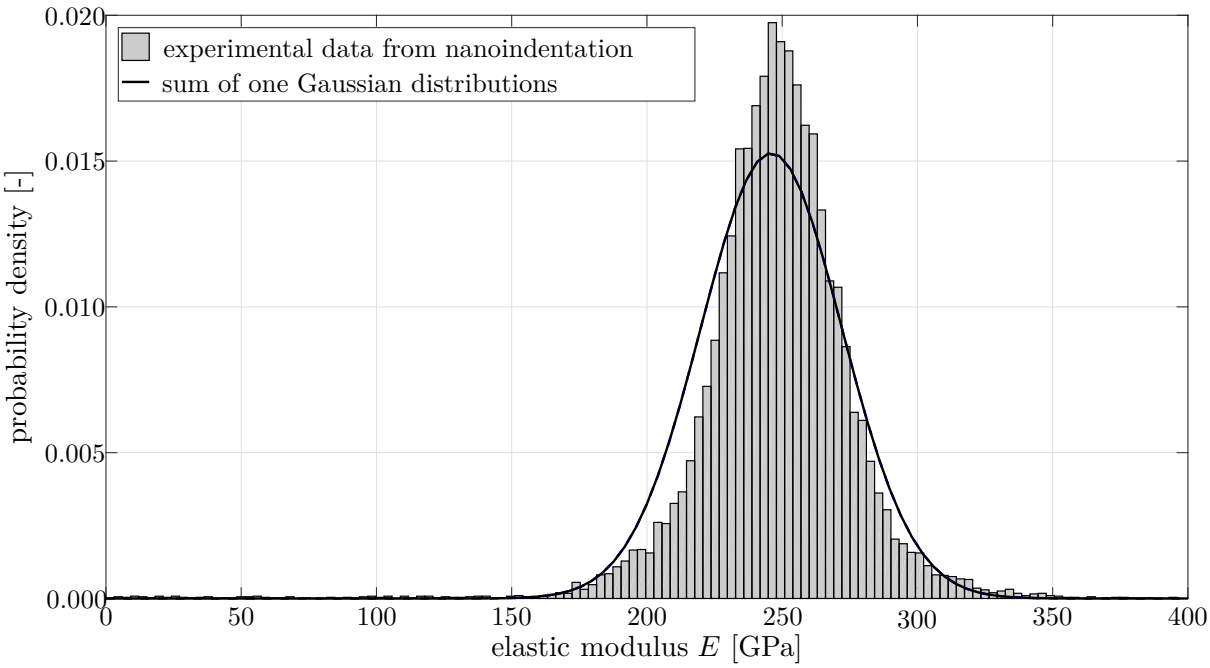

Fig. 3.6: Probability density function of the Young's moduli obtained by means of nanoindentation on all specimens, sorted into 3.02 GPa-wide groups (grey bars); the optimal theoretical fit of the experimental data follows from one Gaussian distribution, see Section 3.5

Tab. 3.7: Number of indents performed in this group, N_{NI}, number of Gaussians needed to obtain optimal fit, N_{ph}, see Section 3.5, and the overall mean value of the group-specific Young's modulus, $\bar{\mu}$, the corresponding standard deviation, $\bar{\sigma}$, and the relative error related to the optimal fit, $\bar{\mathcal{E}}_{rel}$

subset #	description	N_{NI}	N_{ph}	$\bar{\mu}$ [GPa]	$\bar{\sigma}$ [GPa]	$\bar{\mathcal{E}}_{rel}$ [%]
1	Section I	2400	1	249.0	25.6	0.102
2	Section II	2400	1	244.2	24.0	0.609
3	Section III	2400	1	243.2	24.6	0.339
4	Section IV	2400	1	234.2	22.5	0.939
5	Section V	2400	1	238.6	25.7	0.160
6	Section VI	2400	2	265.9	42.5	1.214
7	Section VII	2400	1	252.5	24.6	0.475
8	Sample 1	2800	1	246.2	27.1	0.484
9	Sample 2	2800	2	247.5	39.2	1.162
10	Sample 3	2800	1	243.0	26.3	0.761
11	Sample 4	2800	1	247.5	25.6	0.289
12	Sample 5	2800	1	245.7	25.1	0.203
13	Sample 6	2800	1	245.3	27.0	0.262
14	Section I and II	4800	1	246.8	25.0	0.078
15	Section III and IV	4800	1	239.2	24.1	0.081
16	Section VI and VII	4800	2	258.2	43.1	0.760
17	HAZ	7200	1	244.2	24.9	0.095
18	not-HAZ	7200	1	250.4	26.4	0.886
19	all	16800	1	246.0	26.1	0.457

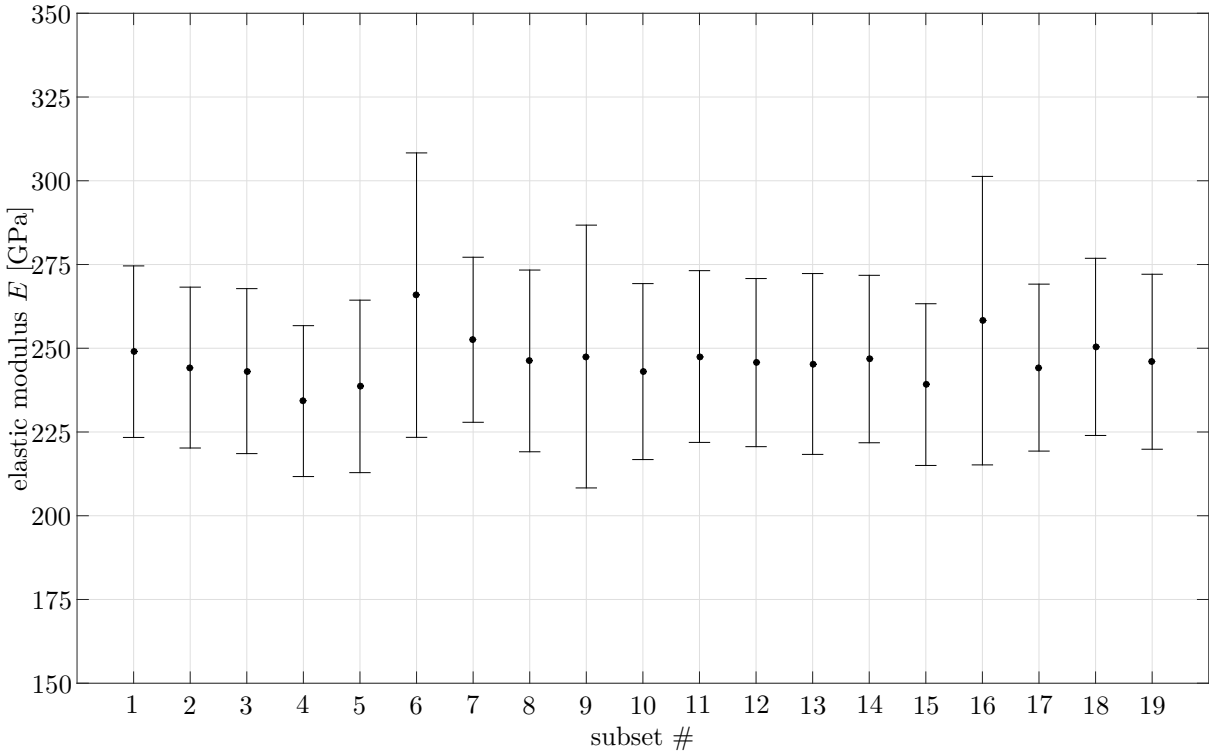

Fig. 3.7: Comparison of the mean value and standard deviation of all subsets, according Tab. 3.7

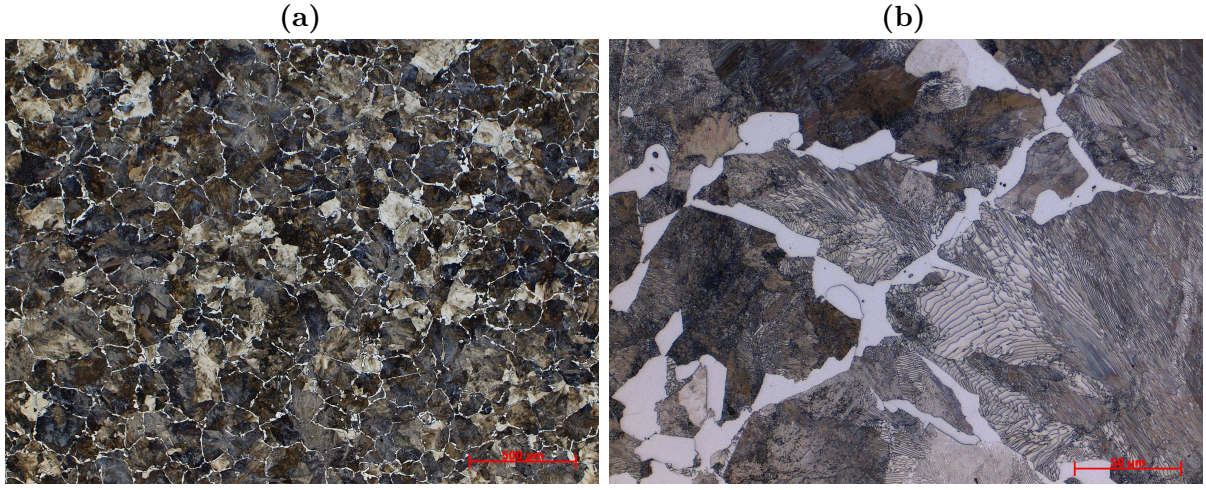

Fig. 3.8: Etched surface of sample III-2 at (a) 5-fold and (b) 50-fold magnification, revealed by light microscopy

3.4 Discussion

3.4.1 Sample irregularities

A large amount of the samples contained one or several outliers, meaning that the analysis of single indentations sometimes resulted in very low Young's moduli of less than 100 GPa. Clearly, such Young's moduli are not representative for steel. In a few cases, these irregularities were even reflected in the statistical evaluation of the results, see, for example, the first peaks of specimens V-3 and V-4 in Tab. 3.5. However, It should be emphasized that the related weighing factors turned out as very low (< 0.01), implying that these outliers do not significantly affect the overall results. Still, it seems due to discuss possible reasons for the unexpectedly low Young's moduli occurring rarely but consistently throughout all tested specimens.

For that purpose, we consider light microscopy images of (unetched) specimen surfaces, see Fig. 3.9. On these images, little black dots are discernible. These dots represent manganese sulphide inclusions, which are actually typical for ferritic steels. Indenting into these inclusion would, on the one hand, indeed lead to Young's moduli which are significantly smaller than the Young's moduli that should be expected for regular steel. On the other hand, the very small size of these inclusions, as compared to the area of an indentation, renders the solidity of this argument (at least) questionable.

A second attempt of explaining the Young's modulus outliers concerns the "cleanliness" of the test implementation. While the tests were performed as careful as possible, it simply cannot be avoided that the tested surfaces are from time to time contaminated by

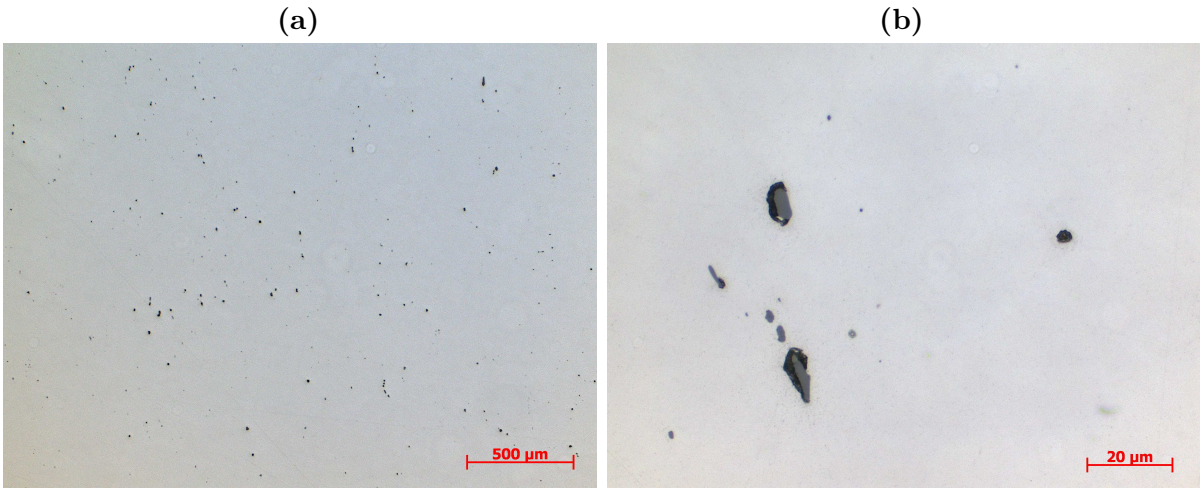

Fig. 3.9: Surface condition of the sample V-4 at (a) a fivefold magnification and at (b) a hundredfold magnification

little dust or dirt particles. Indenting into such particles would likely also lead to reduced Young's moduli.

Nevertheless, reiterating from the first paragraph of this section, it is safe to assume that the overall results are not distorted by the occurrence of a few outliers.

3.4.2 Interpretation of results

First, the Young's moduli obtained for each of the tested specimens, see Tab. 3.4, are considered. The mean values vary between 229.6 and 307.1 GPa, with mean $(\bar{\mu}_{k-l}) = 255.56 \pm 15.0$ GPa. In most cases, the fitting was very accurate, documented by relative errors between the probability density functions obtained by fitting and the experimental ones of less than 1 %. The number of peaks following from the fitting procedure described in Section 3.5 of this paper was in the range of 2 to 4, with a mean value of 2.74 ± 0.77. Tying in with the finding presented in (Pham et al., 2014; Pham and Kim, 2015a; Pham and Kim, 2015b), we conclude that the different peaks may relate to material phases encountered in steel. However, the fact that the stiffnesses between the different material phases significantly overlap makes it very difficult to clearly distinguish between the phases in each and every specimen, resulting in the specimen-specific, varying peak numbers.

Fig. 3.8 shows the (etched) surface of one exemplary specimen in 5- and 50-fold magnification, acquired by means of light microscopy, confirming the expected microheterogeneity of steel. In particular, the individual pearlite grains can be discerned, surrounded by a white ferrite coat (the latter formed during the cooling phase, by replacing the formerly present austenite). In addition, the cementite lamellae are visible in the pearlite grains, with the distances of the lamellae depending on the respective quenching times, and being indicative for how much ferrite is contained. Furthermore, its seems that the overall appearance of the microstructure is also a function of the history the steel has undergone is the region from which the respective sample has been extracted. The sample shown in Fig. 3.8 was taken from the rail web, and the mechanical forces applied for eventually yielding the slim, elongated shape of the web led to an corresponding alignment of the microstructure. This becomes particularly apparent when comparing the microstructures of such samples with the microstructures from samples extracted from different locations (not shown in this paper).

It is also interesting to note that analyzing the nanoindentation test results as described in Section 3.5, that is assuming that the overall probability density function of the Young's moduli is composed of several, phase-specific distributions, leads to an increase of the overall mean value of the Young's modulus, as compared to considering only one distribution which takes all indentations of one specimen into account. This character-

istic becomes apparent when comparing the results shown in Tab. 3.4 to the ones shown in Tab. 3.6. Furthermore, grouping the results, see Tab. 3.7 shows that increasing the number of considered indentations implies a certain smearing effect. Hence, the number of peaks representing the best fit to the experimental data reduce in almost all cases to one. This would mean that the discernibility of the contained material phases decreases with an increasing number of nanoindentations considered in the analysis.

In summary, the results presented in this paper show that the influence of age, location, and maintenance history on the Young's modulus of tramway rail steel in negligible. The observed variations correspond most likely to the material phases typically encountered in steel but significant differences between subsets of all nanoindentations cannot be observed. It is however remarkable that the overall mean value of the results, $255.56 \pm 15.0\,\mathrm{GPa}$, is much higher than the usually assumed ballpark figure of 210 GPa.

3.4.3 Concluding remarks

The comprehensive nanoindentation campaign presented in this paper unambiguously shows that the stiffness distribution across tramway rails is more or less homogeneous. While the derived distributions of Young's moduli exhibit local variations due to the possibly varying stiffnesses of the phases of which steel is composed, the corresponding mean values do not vary significantly when comparing specimens extracted from different locations across tramway cross sections, as well as from rails that underwent different histories (in terms of age and maintenance measures).

In conclusion, coming back to the question posed in the Introduction of this paper, namely whether the stiffness of tramway rails varies with location and age or not, the results presented in Section 3.3 clearly suggest that the answer is "no". However, it should be emphasized that this conclusion is only valid for the stiffness of tramway rails, and not necessarily for other, equally important, properties, such as their strength or resistance against fatigue.

3.5 Paper appendix: Concept of statistical nanoindentation

In the framework of statistical or grid nanoindentation, the measured Young's moduli E_i^{NI}, with index i representing one particular nanoindentation test, $i = 1, \ldots, N_{NI}$, where N_{NI} denotes the total number of indentations, is first sorted into reasonably chosen groups. Thereby, the rule of thumb for the latter is the so-called "square root-rule" – meaning that the width of one group is equal to the square root of the total number of indents.

The Gaussian Cumulative Distribution Function (CDF) relating to the experimental data follows then from

$$D_E^{NI}(E_i^{NI}) = \frac{i}{N_{NI}} - \frac{1}{2N_{NI}}\,. \tag{3.1}$$

It is hypothesized that the experimental CDF follows from superposition of several CDFs. Each of the latter is considered to represent a specific material phase, which may be distinguishable from other material phases based on the chemical composition, or based on various degrees of damage. The aim of statistical nanoindentation is to fit the phase-specific CDFs by means of corresponding Gaussian cumulative distributions, defined through

$$D_{E,j}^{model}\left(E^{NI},\mu_j,\sigma_j\right) = \frac{1}{\sigma_j\sqrt{2\pi}}\int_{-\infty}^{E^{NI}} \exp\left(\frac{-(u-\mu_j)^2}{2\sigma_j^2}\right)\mathrm{d}u\,, \tag{3.2}$$

where μ_j is the mean value of distribution j, $j = 1,\ldots,N_{ph}$, N_{ph} denoting the number of material phases, and σ_j is the corresponding standard deviation. Considering the phase-specific volume fractions f_j, $\sum_j^{N_{ph}} f_j = 1$, as weighing factors, the modeled overall CDF reads as

$$D_E^{model}\left(E^{model}\right) = \sum_j^{N_{ph}} f_j D_{E,j}^{model}\left(E^{NI},\mu_j,\sigma_j\right)\,. \tag{3.3}$$

Finding the phase-specific CDFs that fit to the experimentally found distribution of Young's moduli in the best possible way is an optimization task. Among the many methods available for that purpose, the most common one is based on minimization of the sum of squared errors between the experimentally obtained Young's moduli and the corresponding modelled values, $\mathcal{E}_{SSE}$:

$$\mathcal{E}_{SSE} = \sum_{i=1}^{N_{NI}}\left[D_E^{model}\left(E_i^{model}\right) - D_E^{NI}(E_i^{NI})\right]^2 \rightarrow \min. \tag{3.4}$$

Additionally, as suggested in (Kariem et al., 2015; Furin et al., 2016), the relative error between the experimentally obtained Young's moduli and the corresponding modeled values, $\mathcal{E}_{rel}$, is calculated, defined through

$$\mathcal{E}_{rel} = \frac{100}{\max\left(E^{NI}\right) - \min\left(E^{NI}\right)} \int_{\min(E^{NI})}^{\max\left(E^{NI}\right)} \left[D_E^{model}\left(E_i^{model}\right) - D_E^{NI}(E_i^{NI})\right]\mathrm{d}E\,, \tag{3.5}$$

where $\max(E^{NI})$ and $\min(E^{NI})$ are the maximum and minimum values of the elastic moduli gained from the nanoindentation tests, and $[\max(E^{NI}) - \min(E^{NI})]$ is the total range of the moduli. This additional quantity allows for definition of a termination criterion of the optimization. Starting from $N_{ph} = 1$, increasing N_{ph} can be expected to

imply a reduced relative error, up to the optimal number of material phases. The latter is assumingly reached at the first local minimum of $\mathcal{E}_{rel}$; meaning that $N_{ph} = N_{optimal}$ if $\mathcal{E}_{rel}(N_{ph}) < \mathcal{E}_{rel}(N_{ph} + 1)$.

Chapter 4

Additional results

Due to the conciseness required for scientific papers, Section 3 does not contain all (but only exemplary) results obtained from the analysis of the nanoindentation results. This section is devoted to completing the presentation of the results that have accumulated during implementation of the research project presented in this thesis.

4.1 Further analyses

In order to optimize the visualization the distribution of the Young's moduli obtained for a single specimen, the corresponding gradients and fluctuation lengths were calculated. The gradient is defined through

$$\operatorname{grad} E = \begin{pmatrix} \dfrac{\partial E}{\partial x} \\ \dfrac{\partial E}{\partial y} \end{pmatrix}_{\mathbf{e}_x, \mathbf{e}_y} , \tag{4.1}$$

where $\mathbf{e}_x$ and $\mathbf{e}_y$ are the unit vectors of a two-dimensional Cartesian base system, while x and y are the corresponding coordinates. Eq. (4.1) is computed numerically, based on Fig. 4.1, through

$$X = \frac{E_{right} - E_{left}}{x_{right} - x_{left}} \quad \text{and} \quad Y = \frac{E_{top} - E_{bottom}}{y_{top} - y_{bottom}} . \tag{4.2}$$

The fluctuation length allows for better comparability between different specimens, and can be considered as some kind of normalization. It is defined through

$$l_{fluctuation} = \frac{E}{||\operatorname{grad} E||} , \tag{4.3}$$

with operation $||(\cdot)||$ being the Euclidean norm of vector $(\cdot)$.

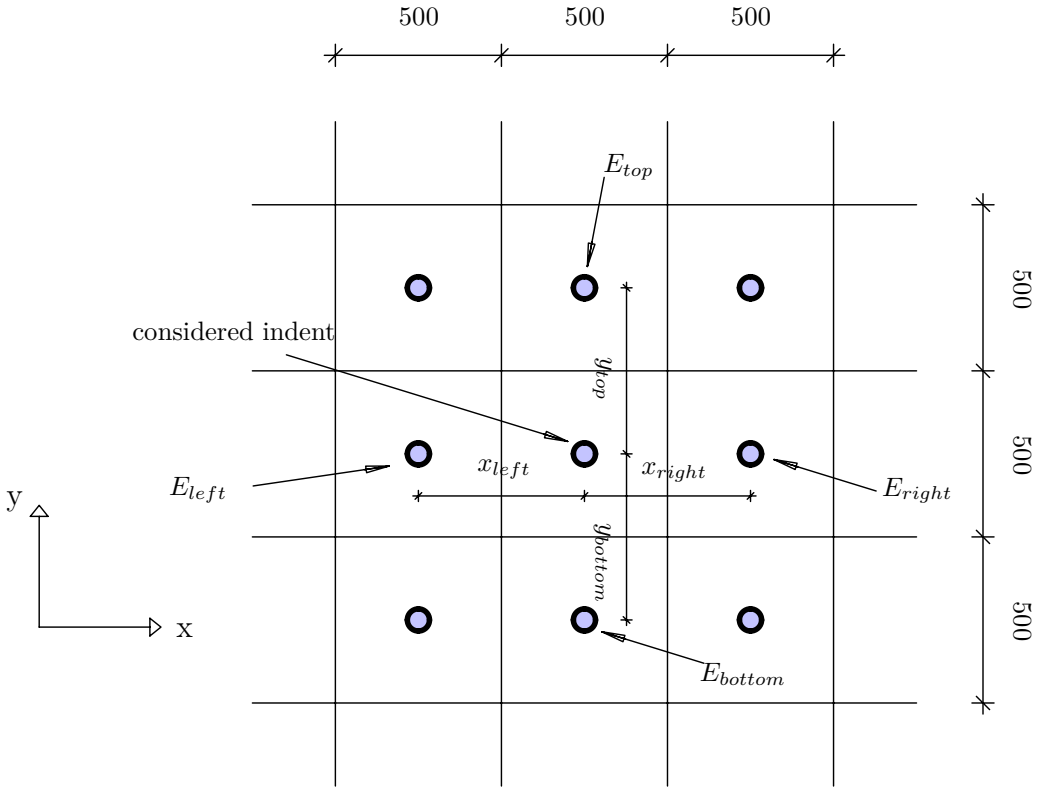

Fig. 4.1: Definition of the indices needed for evaluation of Eqs. (4.2)

4.2 Collection of nanoindentation results

This section presents all results acquired in the nanoindentation campaign, see Figs. 4.2 to 4.43. The corresponding interpretations and conclusions have already been presented in Section 3.4 of this thesis.

4.3 Light microscopy images

This section presents a representative collection of the light microscopy images acquired in this study, allowing for comparison of the microstructures of different specimens, see Figs. 4.44 and 4.45.

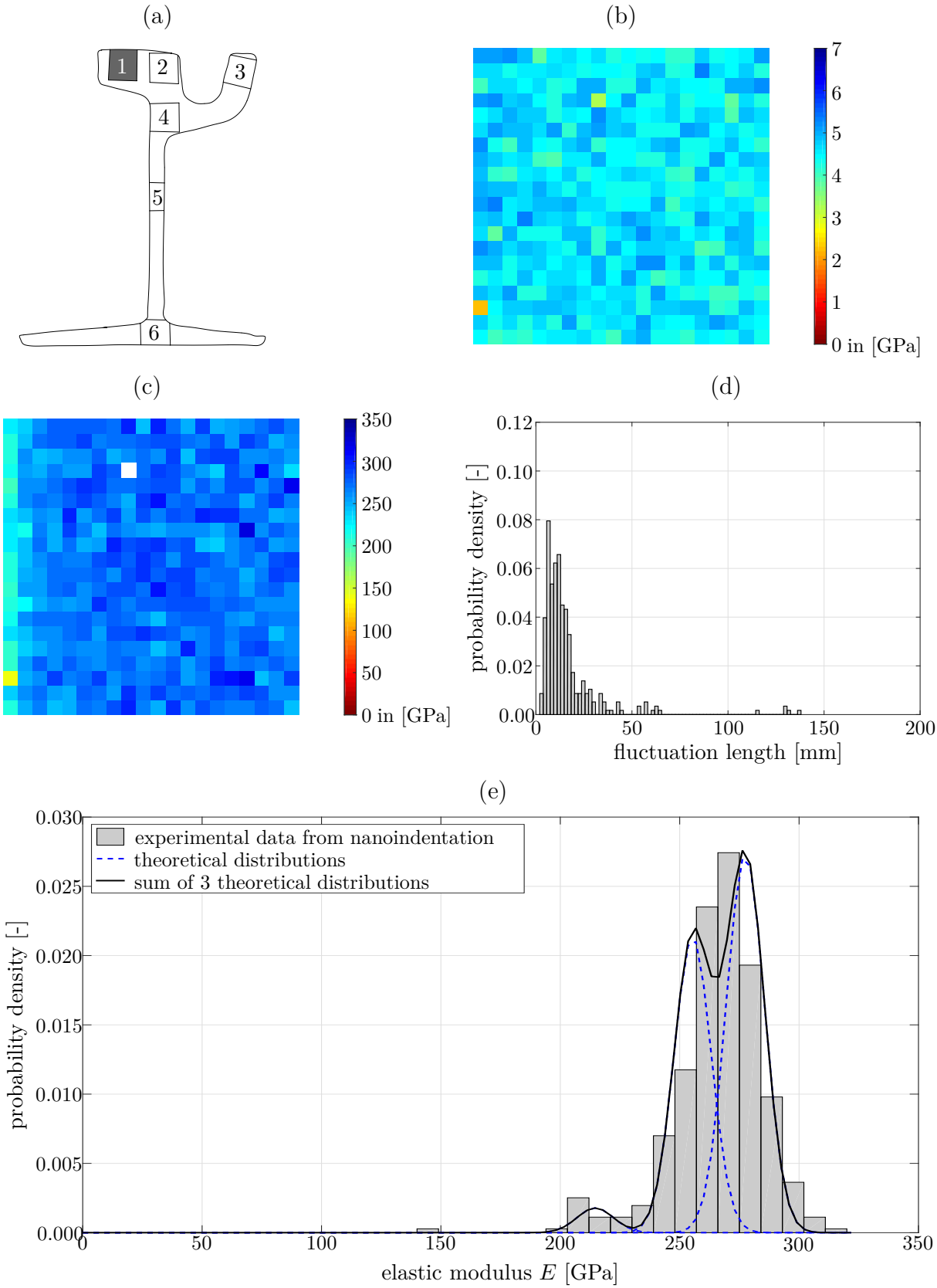

Fig. 4.2: Nanoindentation results for specimen I-1; (a) definition of specimen position; (b) hardness and (c) Young's modulus distributions across the tested area; (d) histogram showing the fluctuation length of the Young's modulus; (e) probability density function of the Young's modulus, as well as fitting of the data by means of 3 Gaussian (theoretical) distribution

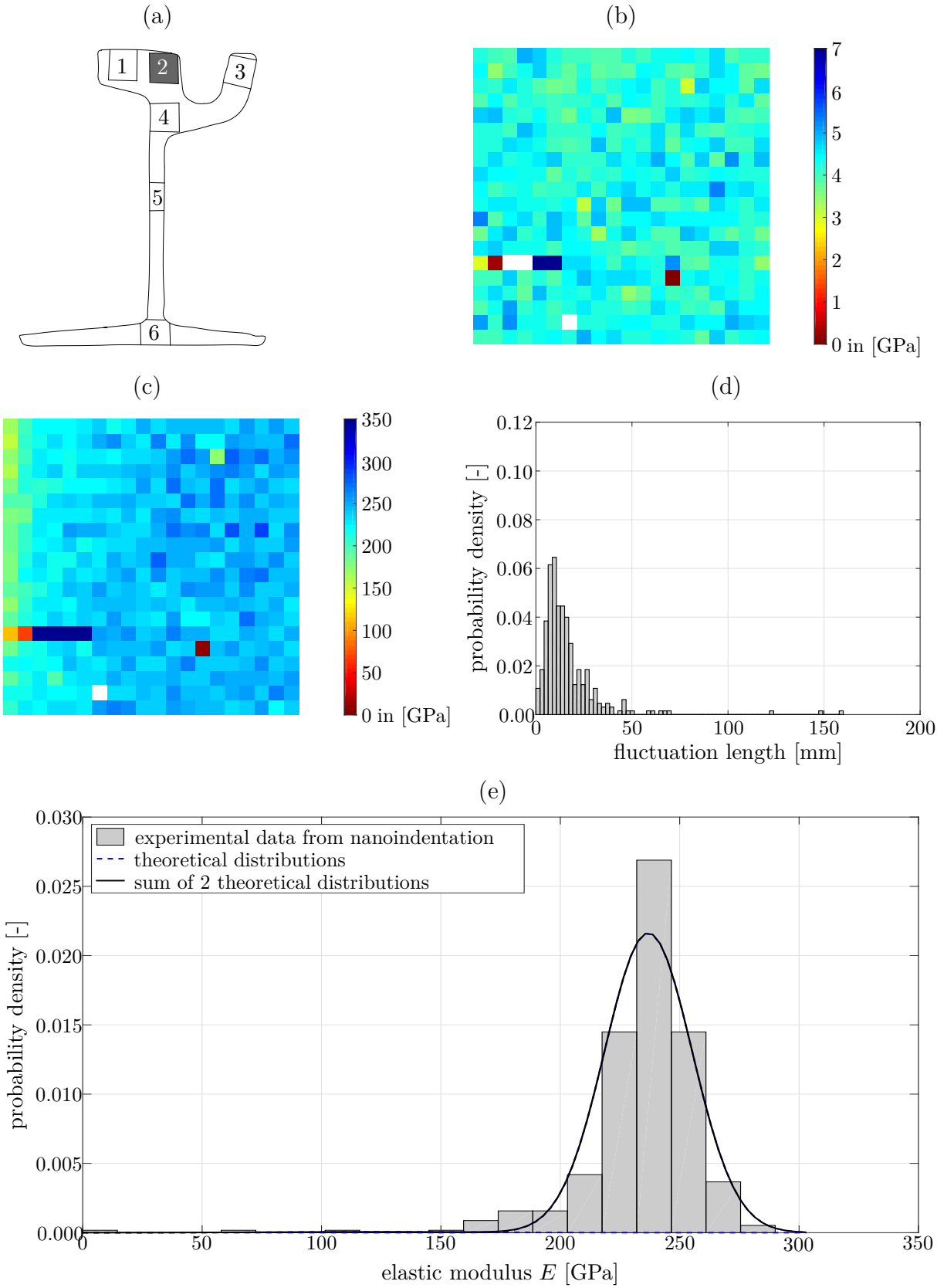

Fig. 4.3: Nanoindentation results for specimen I-2; (a) definition of specimen position; (b) hardness and (c) Young's modulus distributions across the tested area; (d) histogram showing the fluctuation length of the Young's modulus; (e) probability density function of the Young's modulus, as well as fitting of the data by means of 2 Gaussian (theoretical) distribution

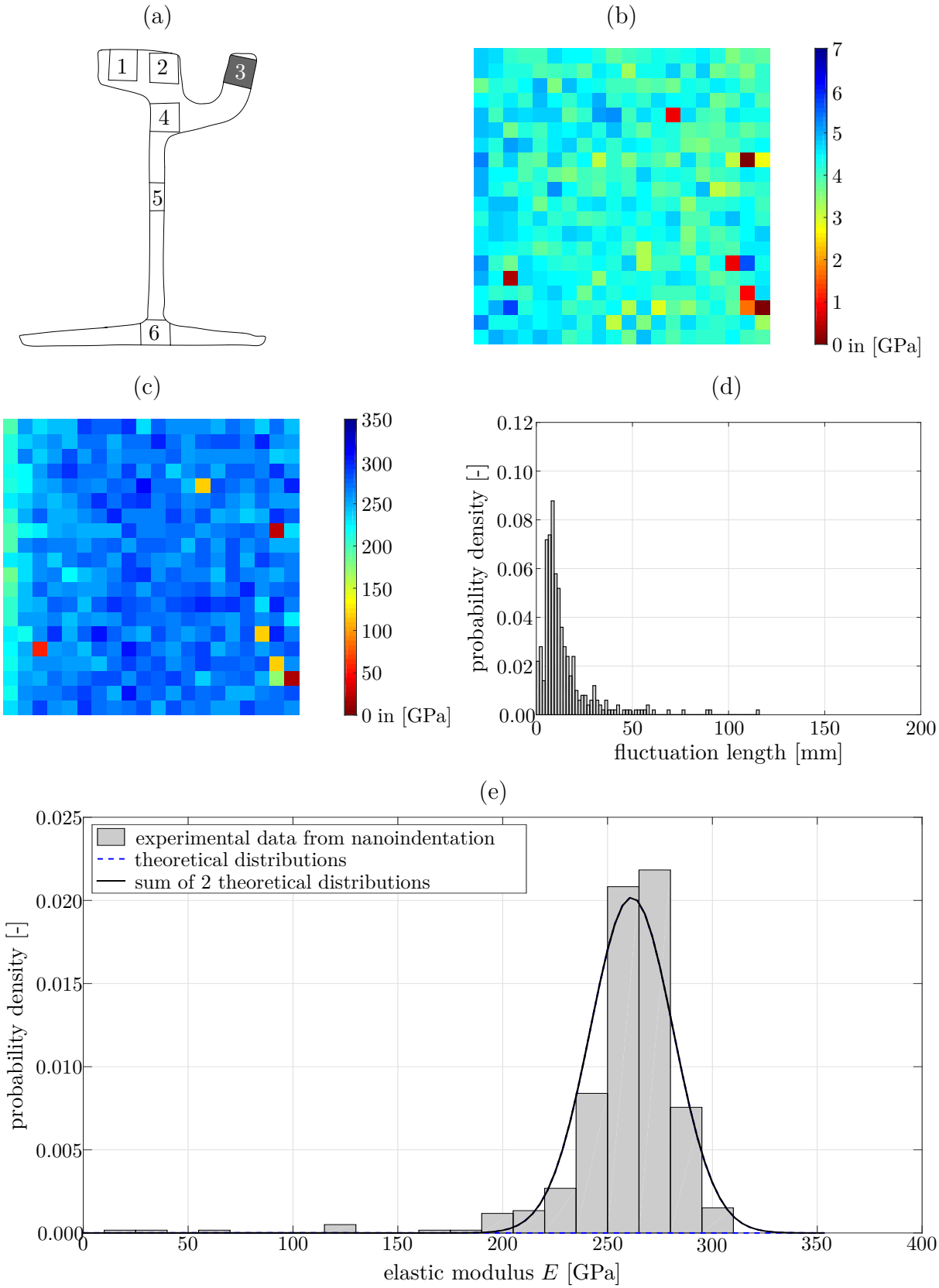

Fig. 4.4: Nanoindentation results for specimen I-3; (a) definition of specimen position; (b) hardness and (c) Young's modulus distributions across the tested area; (d) histogram showing the fluctuation length of the Young's modulus; (e) probability density function of the Young's modulus, as well as fitting of the data by means of 2 Gaussian (theoretical) distribution

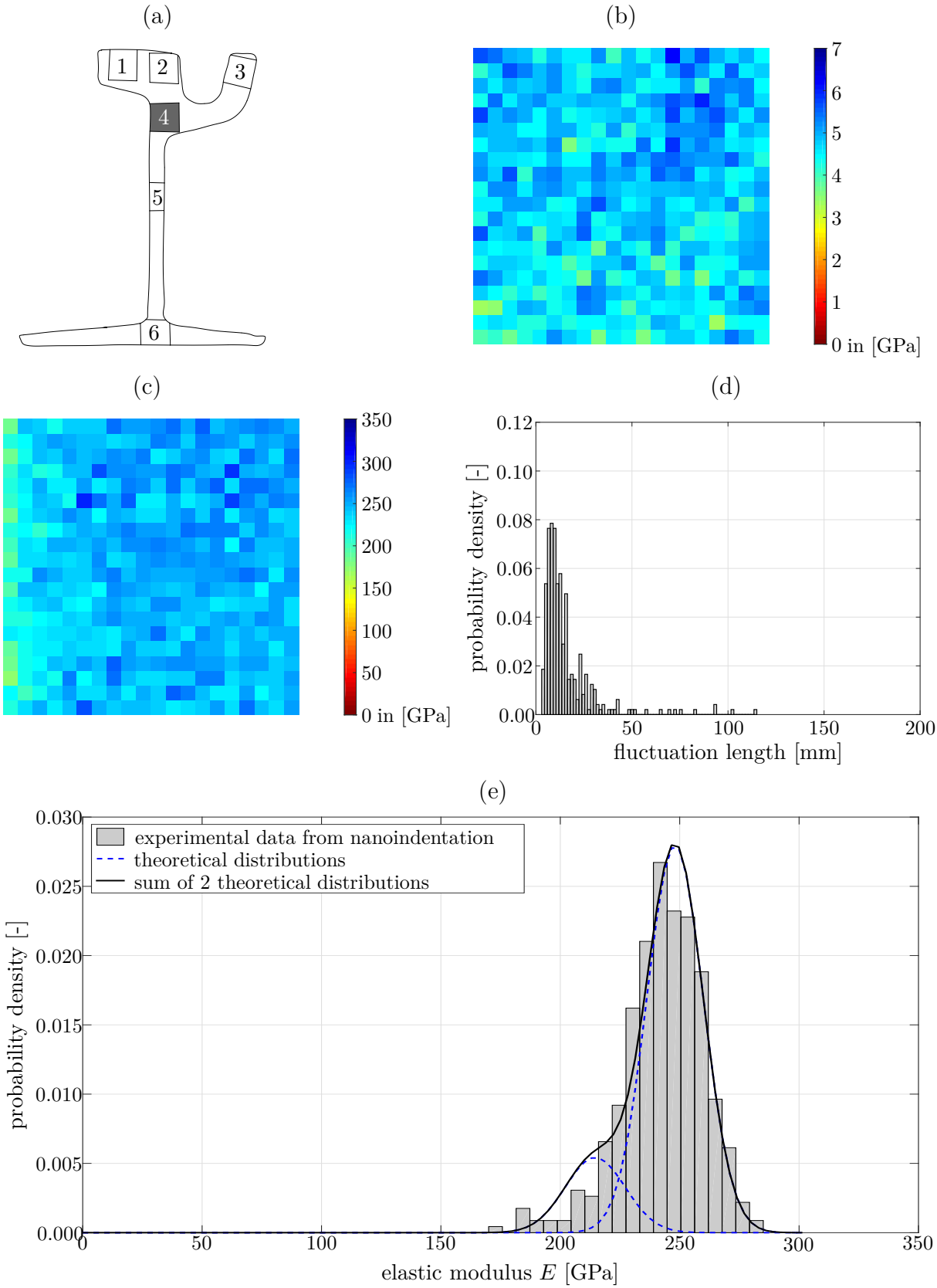

Fig. 4.5: Nanoindentation results for specimen I-4; (a) definition of specimen position; (b) hardness and (c) Young's modulus distributions across the tested area; (d) histogram showing the fluctuation length of the Young's modulus; (e) probability density function of the Young's modulus, as well as fitting of the data by means of 2 Gaussian (theoretical) distribution

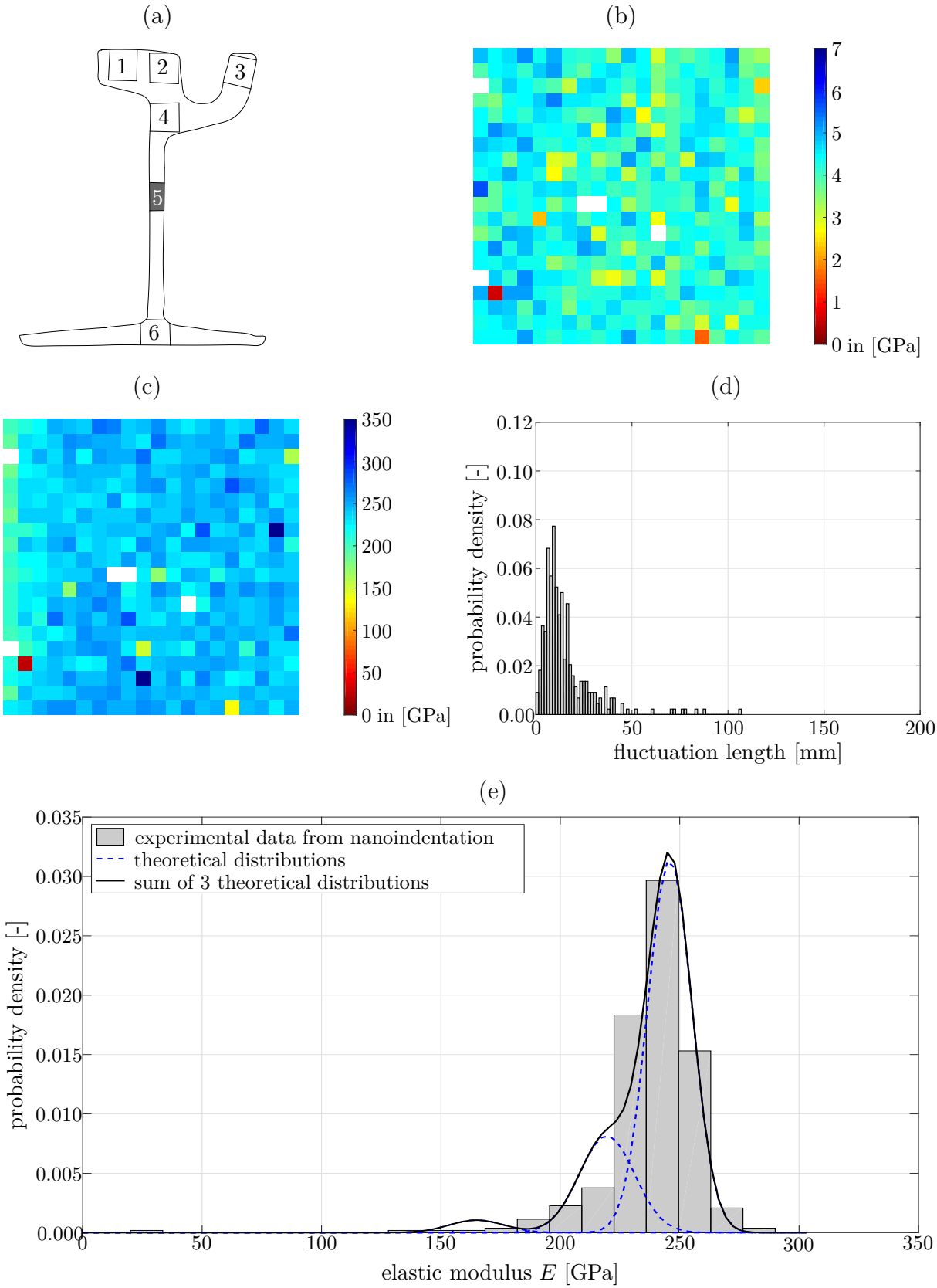

Fig. 4.6: Nanoindentation results for specimen I-5; (a) definition of specimen position; (b) hardness and (c) Young's modulus distributions across the tested area; (d) histogram showing the fluctuation length of the Young's modulus; (e) probability density function of the Young's modulus, as well as fitting of the data by means of 3 Gaussian (theoretical) distribution

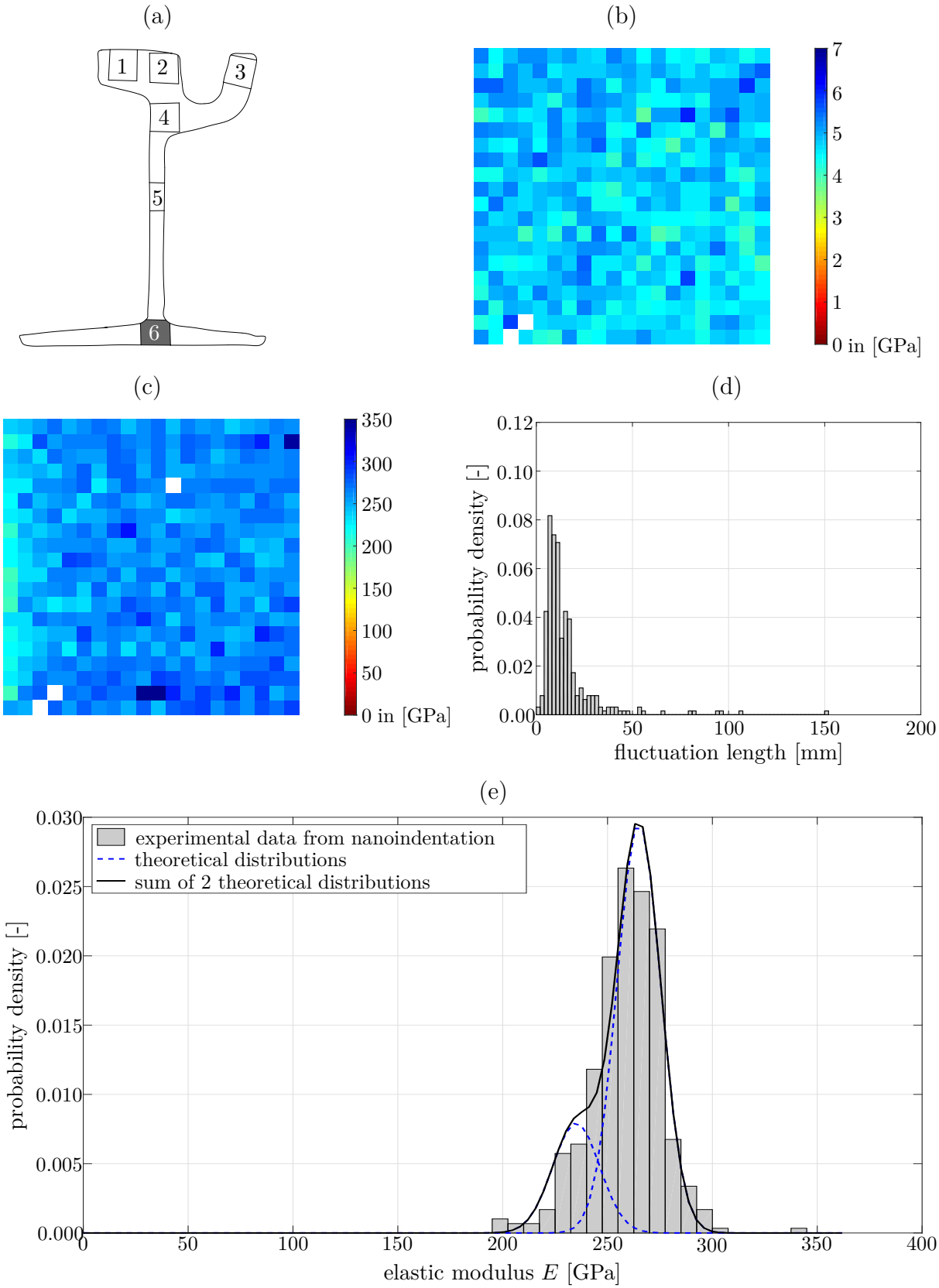

Fig. 4.7: Nanoindentation results for specimen I-6; (a) definition of specimen position; (b) hardness and (c) Young's modulus distributions across the tested area; (d) histogram showing the fluctuation length of the Young's modulus; (e) probability density function of the Young's modulus, as well as fitting of the data by means of 2 Gaussian (theoretical) distribution

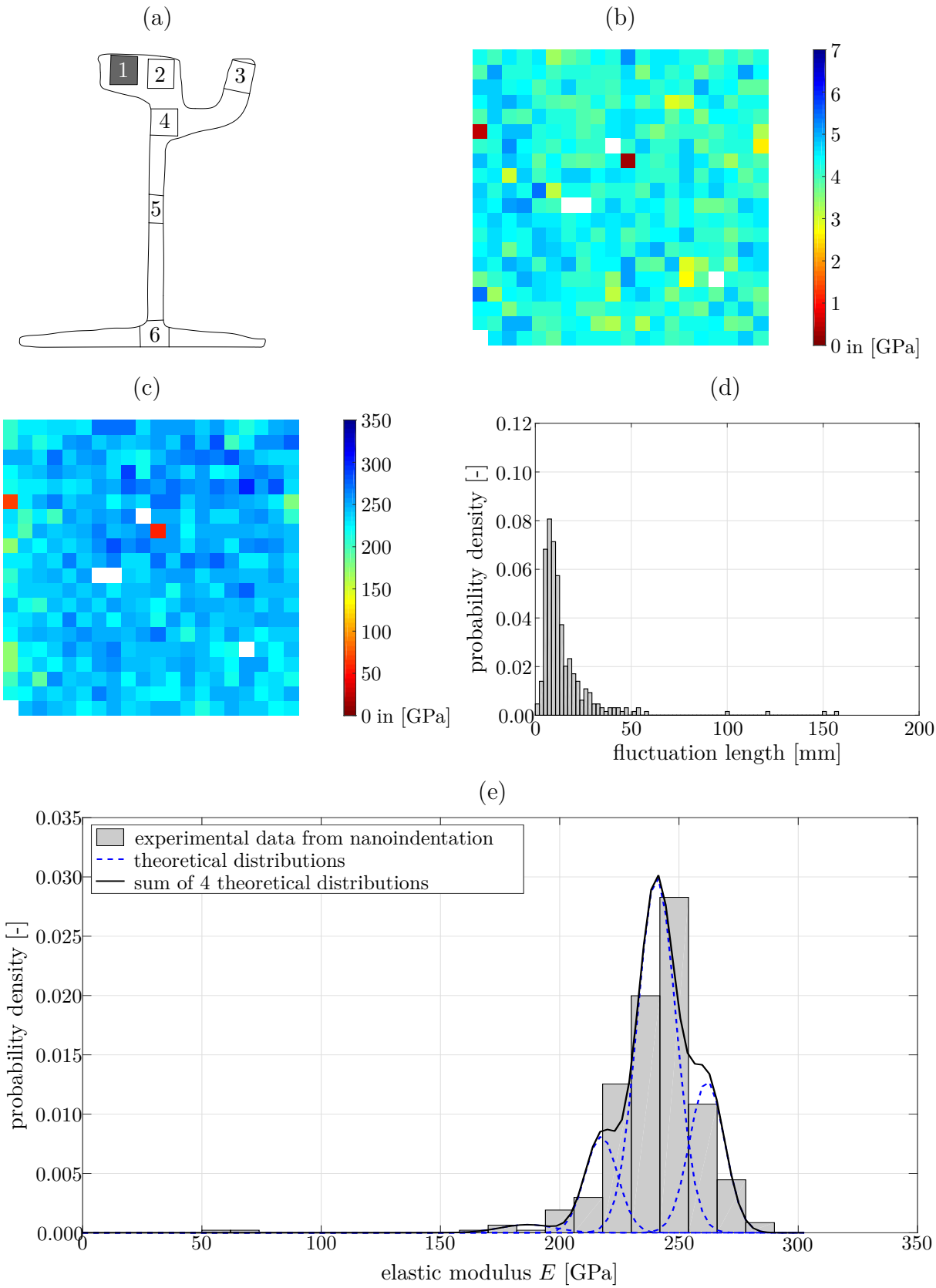

Fig. 4.8: Nanoindentation results for specimen II-1; (a) definition of specimen position; (b) hardness and (c) Young's modulus distributions across the tested area; (d) histogram showing the fluctuation length of the Young's modulus; (e) probability density function of the Young's modulus, as well as fitting of the data by means of 4 Gaussian (theoretical) distribution

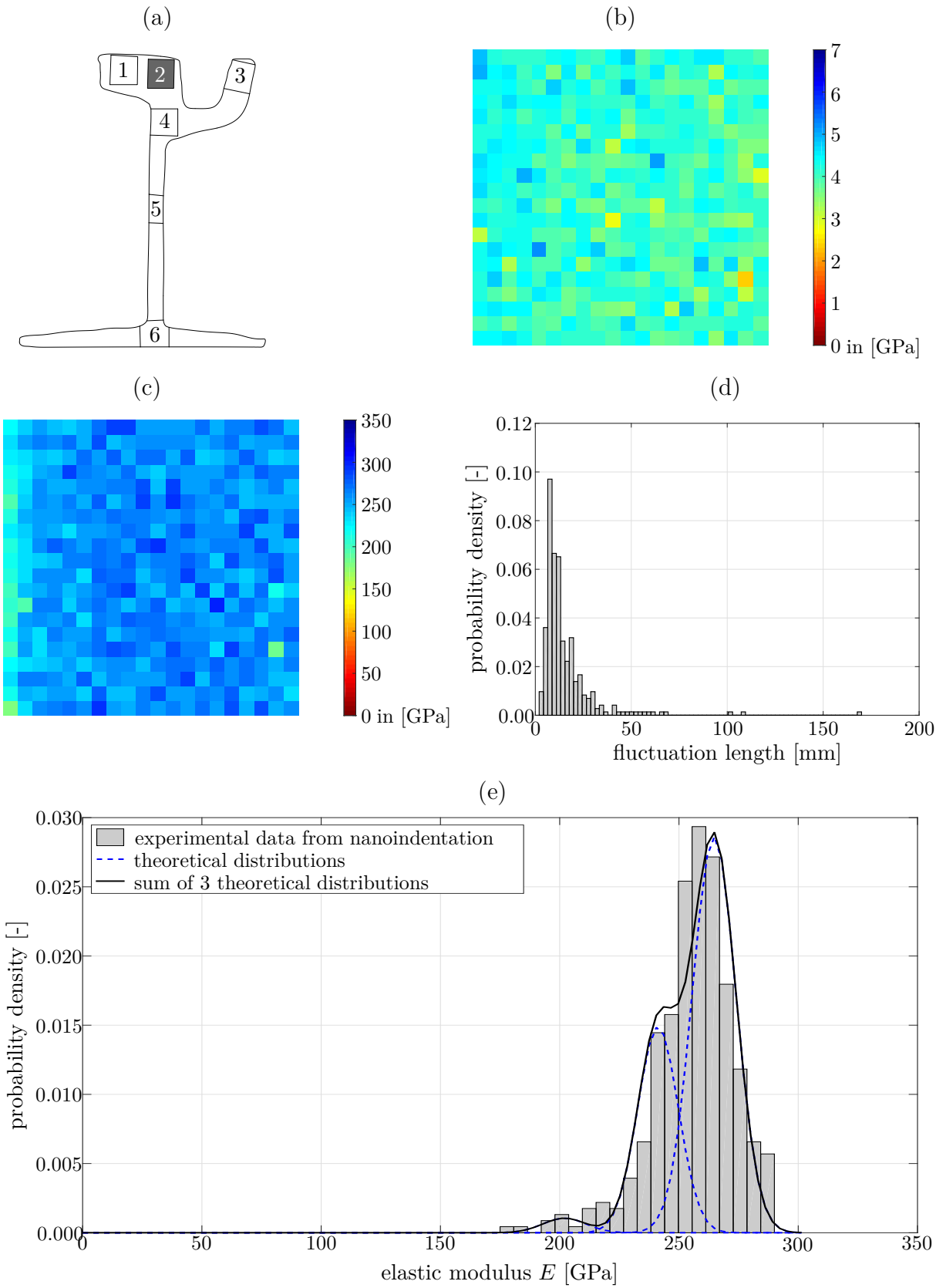

Fig. 4.9: Nanoindentation results for specimen II-2; (a) definition of specimen position; (b) hardness and (c) Young's modulus distributions across the tested area; (d) histogram showing the fluctuation length of the Young's modulus; (e) probability density function of the Young's modulus, as well as fitting of the data by means of 3 Gaussian (theoretical) distribution

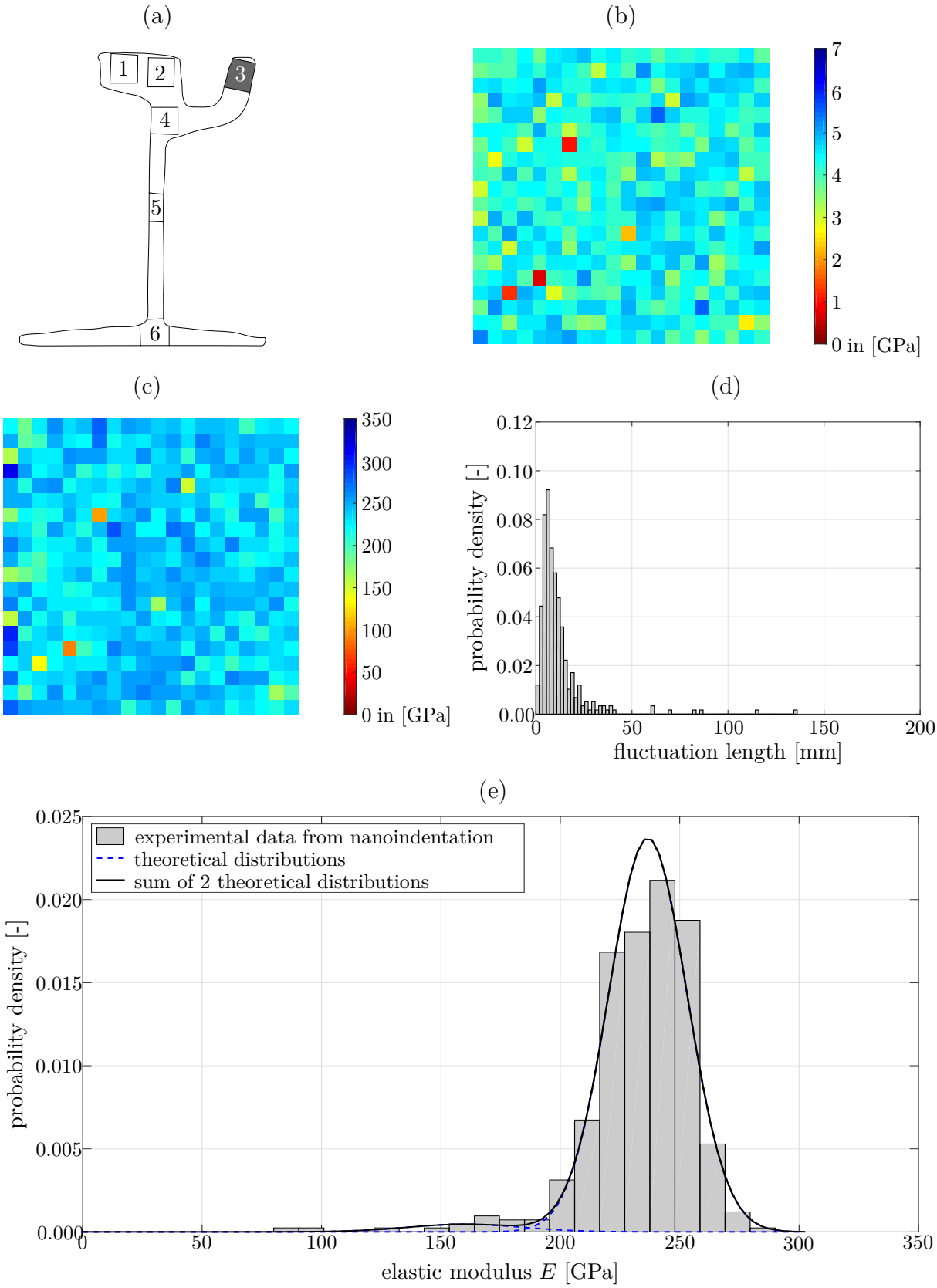

Fig. 4.10: Nanoindentation results for specimen II-3; (a) definition of specimen position; (b) hardness and (c) Young's modulus distributions across the tested area; (d) histogram showing the fluctuation length of the Young's modulus; (e) probability density function of the Young's modulus, as well as fitting of the data by means of 2 Gaussian (theoretical) distribution

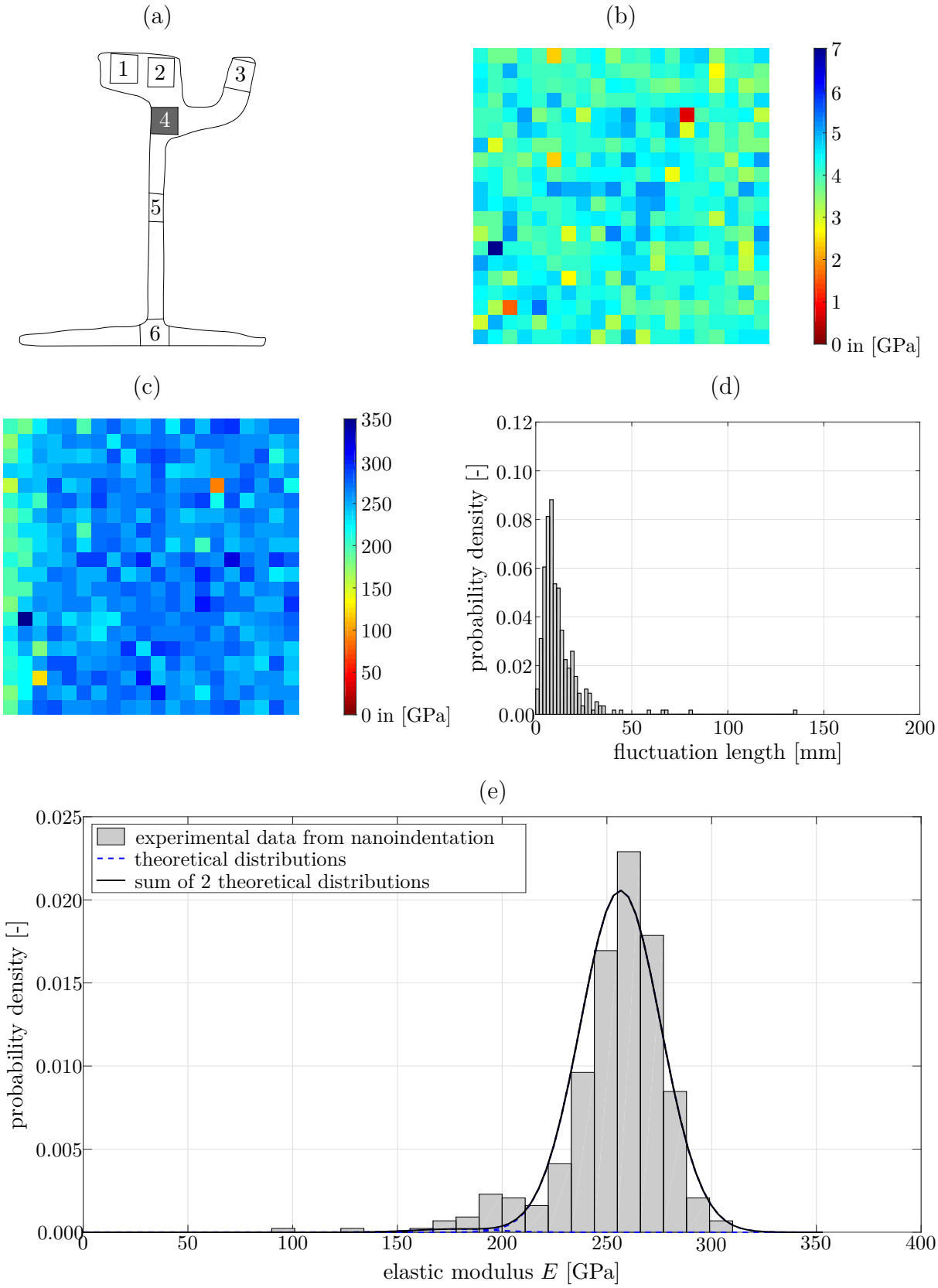

Fig. 4.11: Nanoindentation results for specimen II-4; (a) definition of specimen position; (b) hardness and (c) Young's modulus distributions across the tested area; (d) histogram showing the fluctuation length of the Young's modulus; (e) probability density function of the Young's modulus, as well as fitting of the data by means of 2 Gaussian (theoretical) distribution

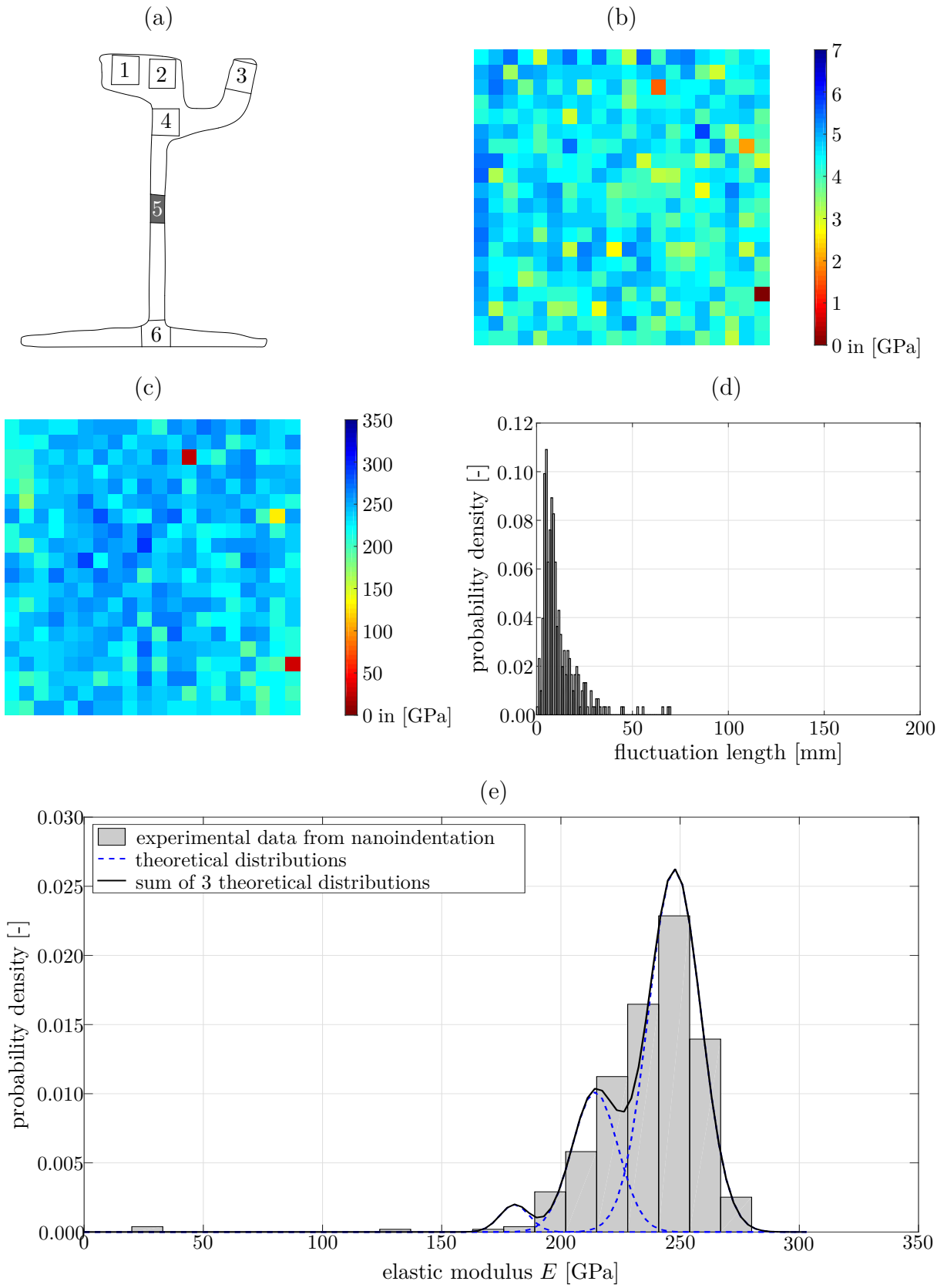

Fig. 4.12: Nanoindentation results for specimen II-5; (a) definition of specimen position; (b) hardness and (c) Young's modulus distributions across the tested area; (d) histogram showing the fluctuation length of the Young's modulus; (e) probability density function of the Young's modulus, as well as fitting of the data by means of 3 Gaussian (theoretical) distribution

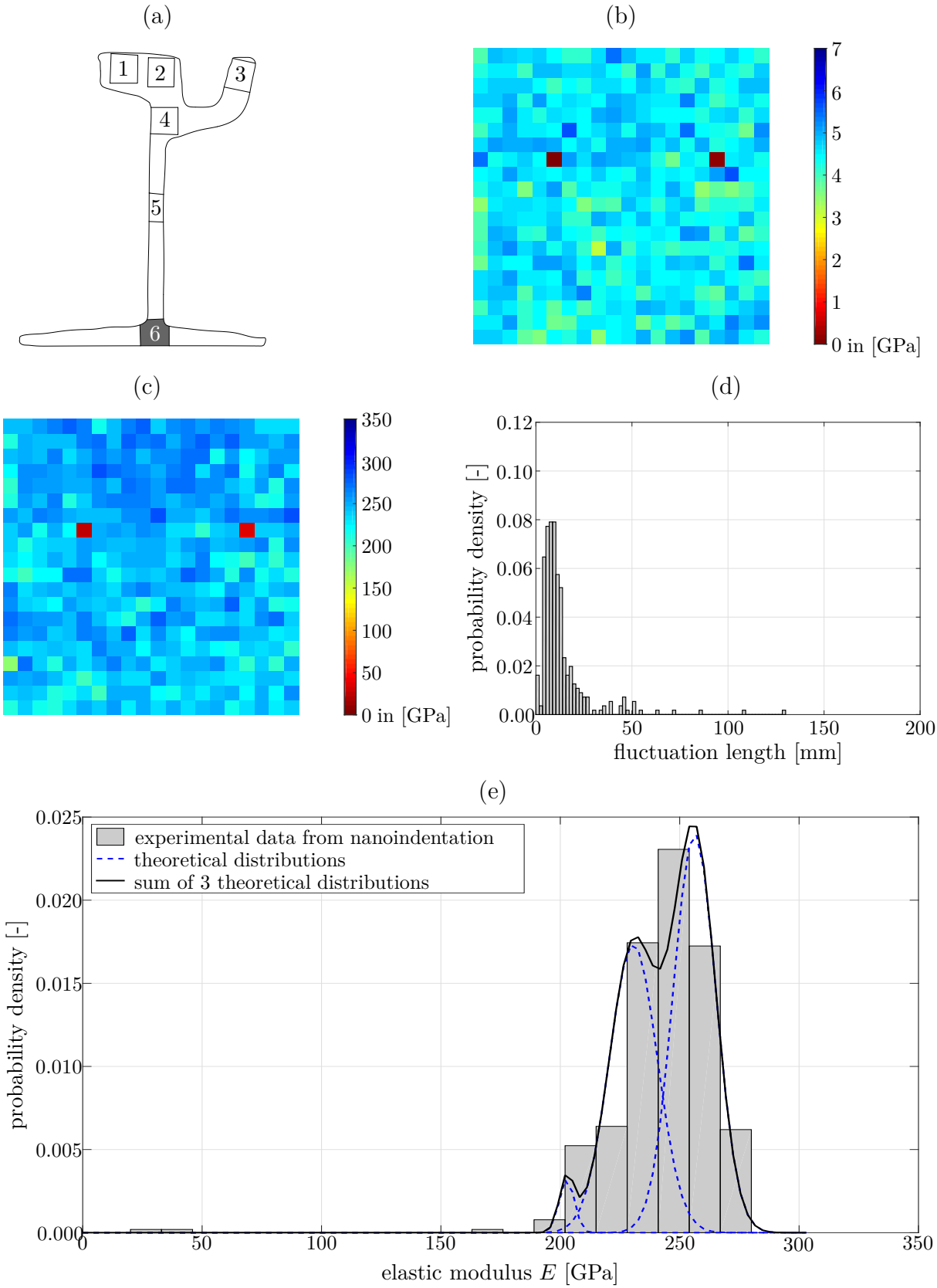

Fig. 4.13: Nanoindentation results for specimen II-6; (a) definition of specimen position; (b) hardness and (c) Young's modulus distributions across the tested area; (d) histogram showing the fluctuation length of the Young's modulus; (e) probability density function of the Young's modulus, as well as fitting of the data by means of 3 Gaussian (theoretical) distribution

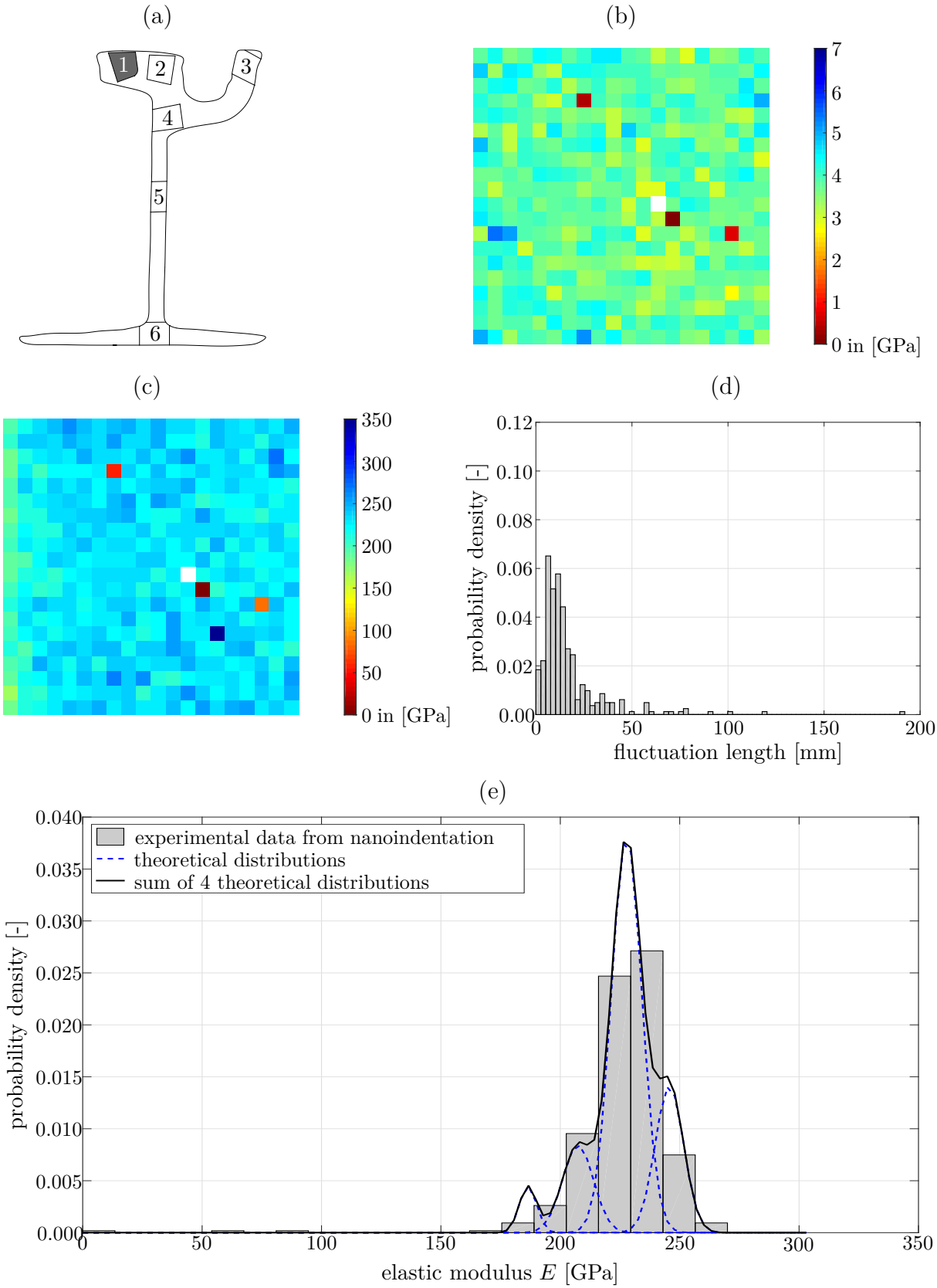

Fig. 4.14: Nanoindentation results for specimen III-1; (a) definition of specimen position; (b) hardness and (c) Young's modulus distributions across the tested area; (d) histogram showing the fluctuation length of the Young's modulus; (e) probability density function of the Young's modulus, as well as fitting of the data by means of 4 Gaussian (theoretical) distribution

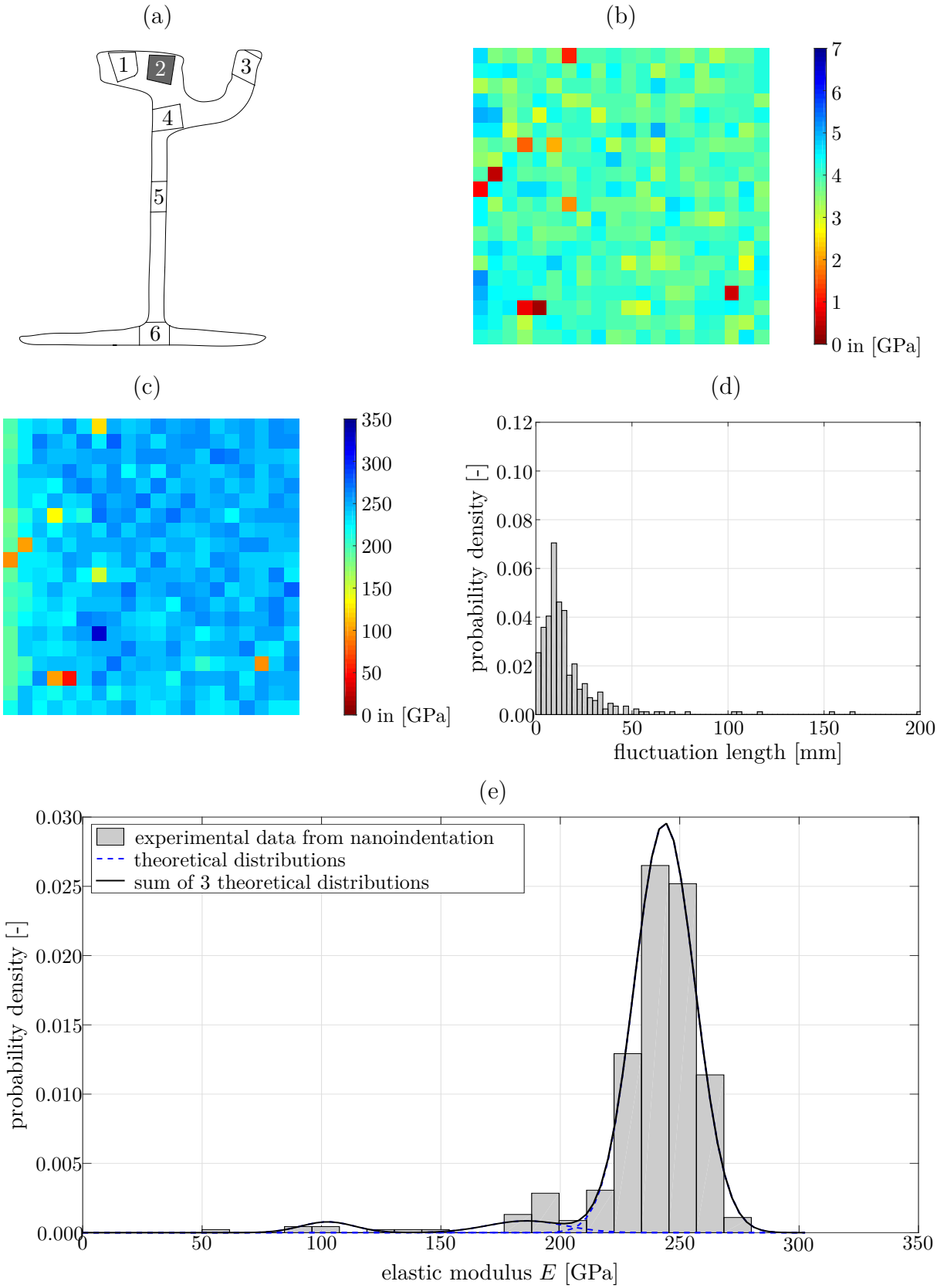

Fig. 4.15: Nanoindentation results for specimen III-2; (a) definition of specimen position; (b) hardness and (c) Young's modulus distributions across the tested area; (d) histogram showing the fluctuation length of the Young's modulus; (e) probability density function of the Young's modulus, as well as fitting of the data by means of 3 Gaussian (theoretical) distribution

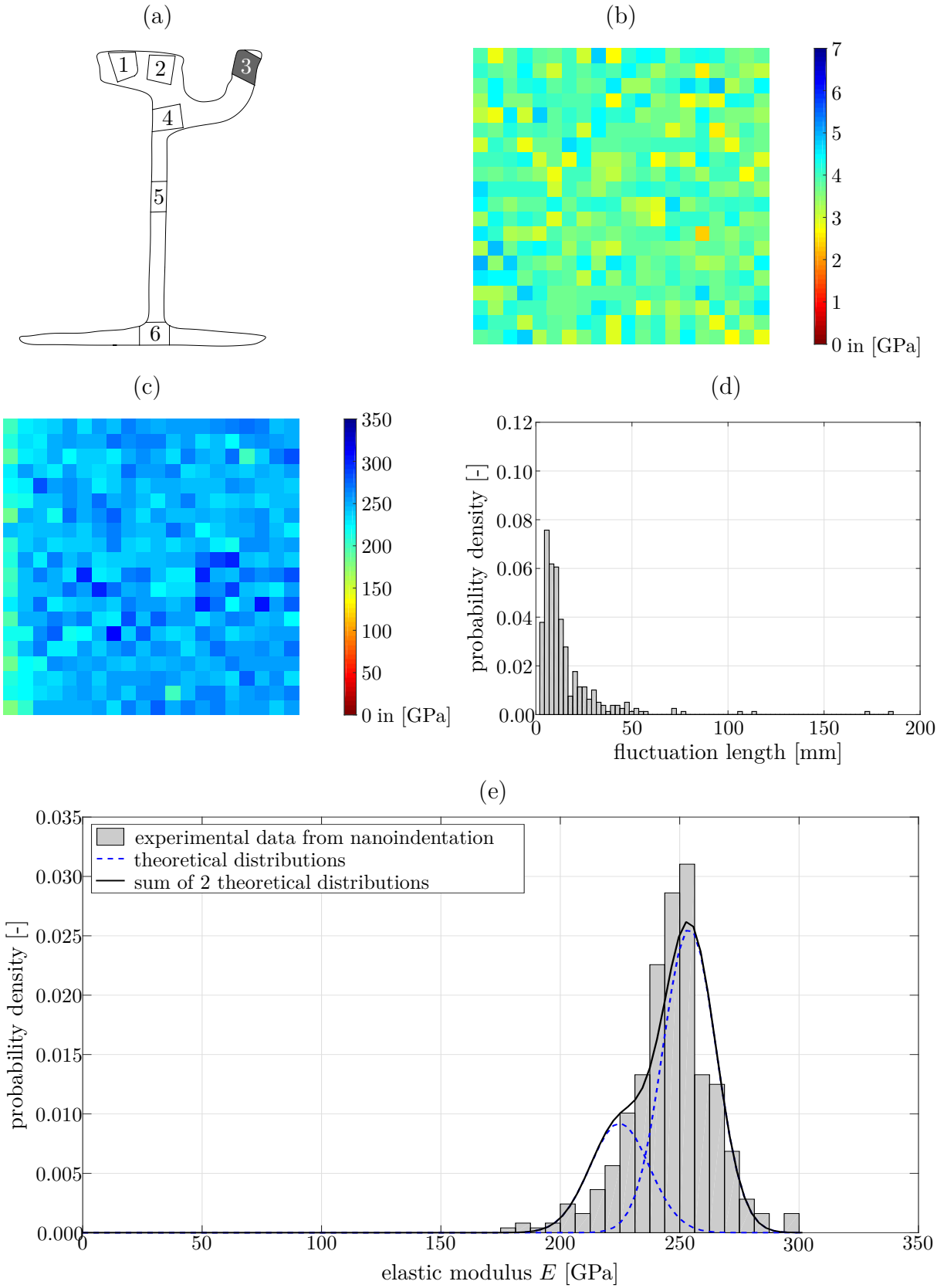

Fig. 4.16: Nanoindentation results for specimen III-3; (a) definition of specimen position; (b) hardness and (c) Young's modulus distributions across the tested area; (d) histogram showing the fluctuation length of the Young's modulus; (e) probability density function of the Young's modulus, as well as fitting of the data by means of 2 Gaussian (theoretical) distribution

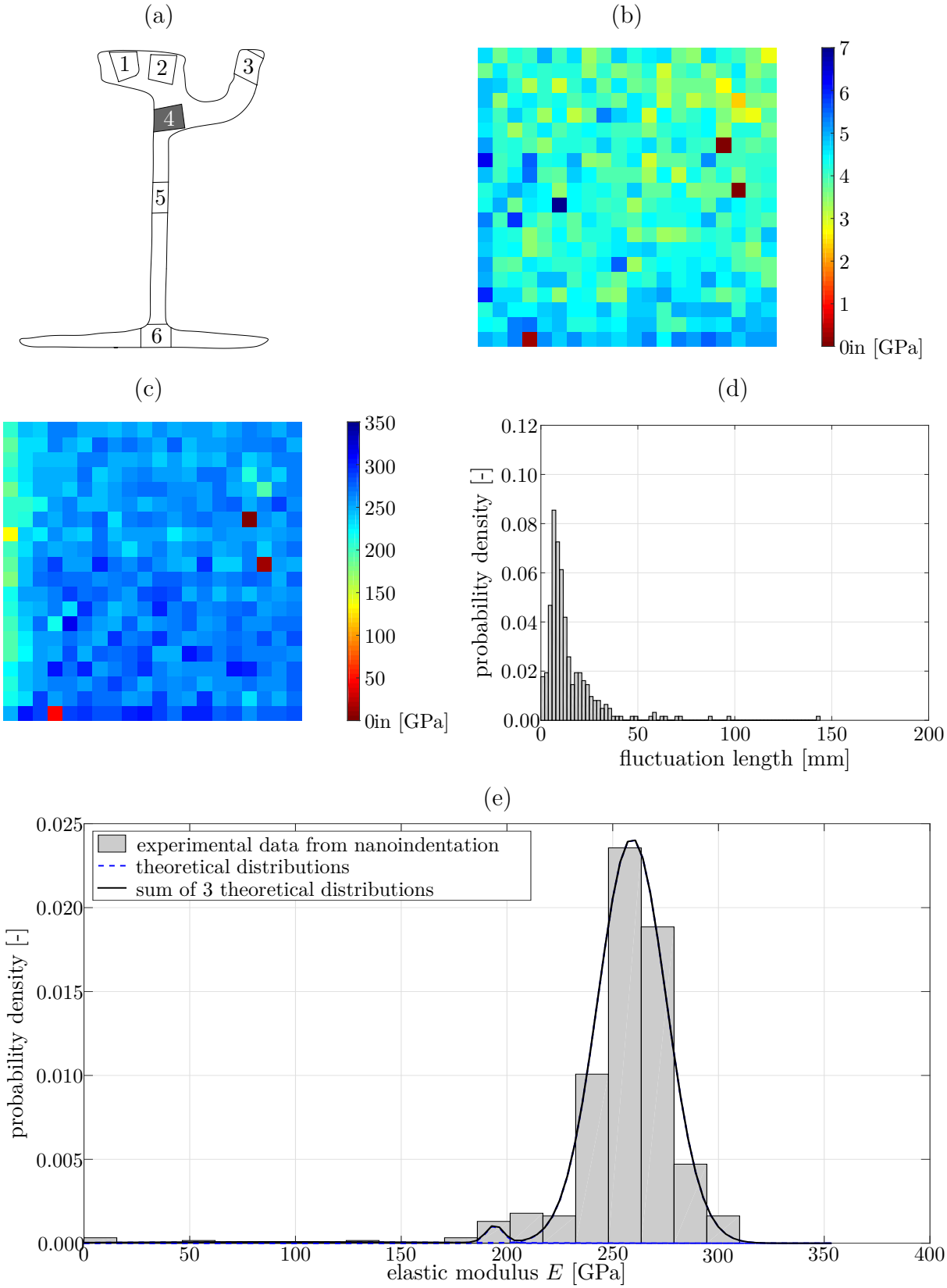

Fig. 4.17: Nanoindentation results for specimen III-4; (a) definition of specimen position; (b) hardness and (c) Young's modulus distributions across the tested area; (d) histogram showing the fluctuation length of the Young's modulus; (e) probability density function of the Young's modulus, as well as fitting of the data by means of 3 Gaussian (theoretical) distribution

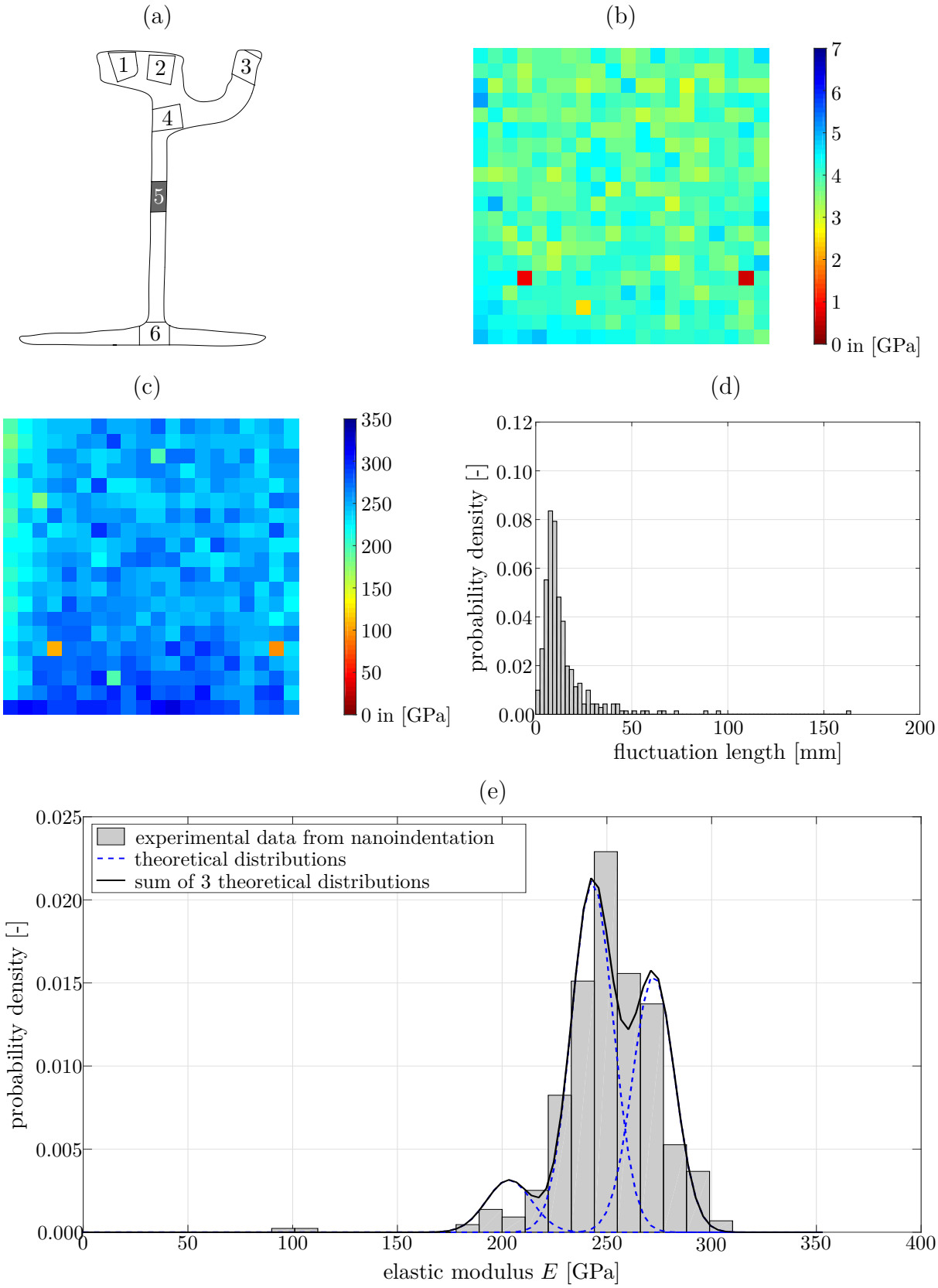

Fig. 4.18: Nanoindentation results for specimen III-5; (a) definition of specimen position; (b) hardness and (c) Young's modulus distributions across the tested area; (d) histogram showing the fluctuation length of the Young's modulus; (e) probability density function of the Young's modulus, as well as fitting of the data by means of 3 Gaussian (theoretical) distribution

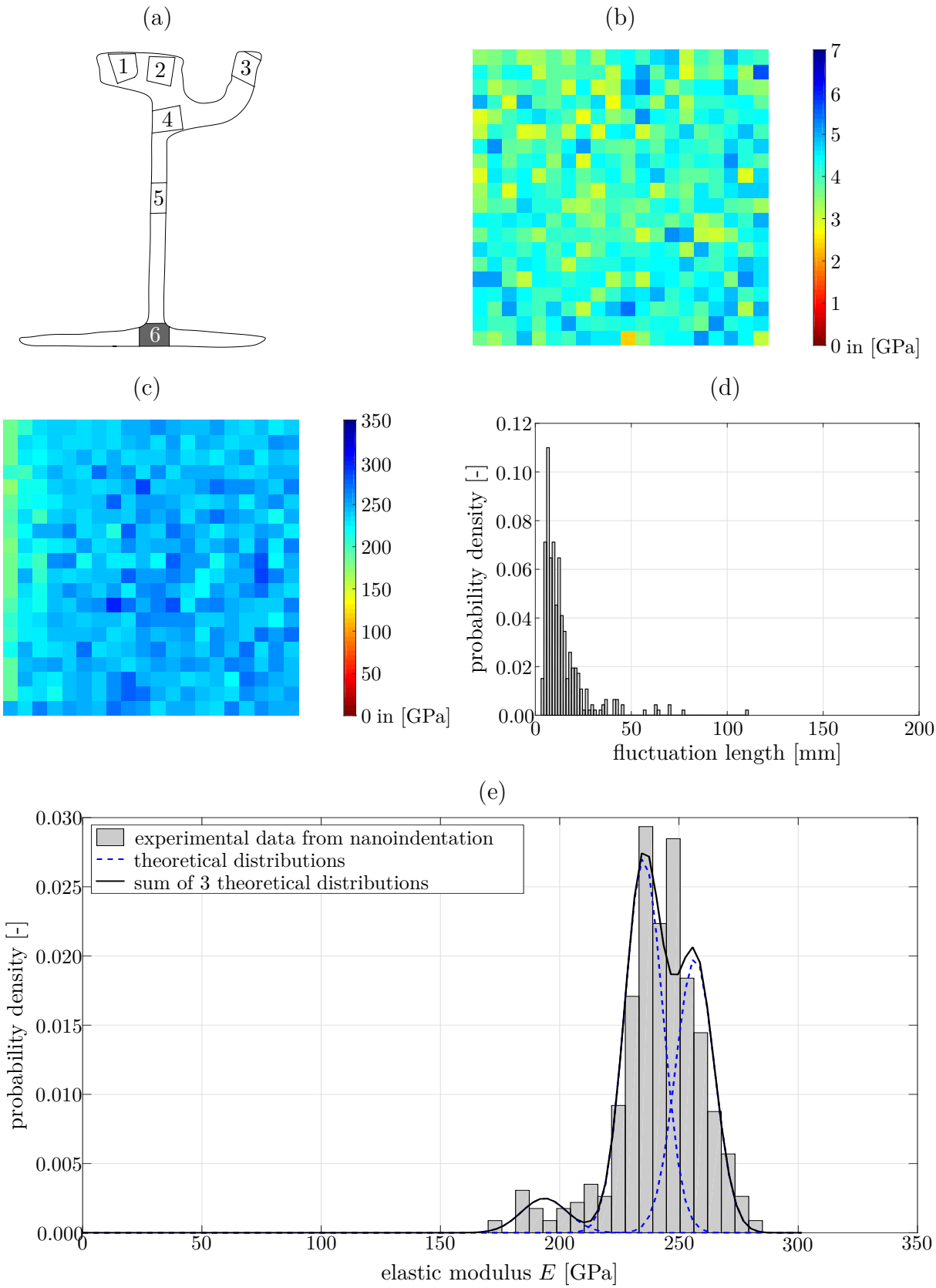

Fig. 4.19: Nanoindentation results for specimen III-6; (a) definition of specimen position; (b) hardness and (c) Young's modulus distributions across the tested area; (d) histogram showing the fluctuation length of the Young's modulus; (e) probability density function of the Young's modulus, as well as fitting of the data by means of 3 Gaussian (theoretical) distribution

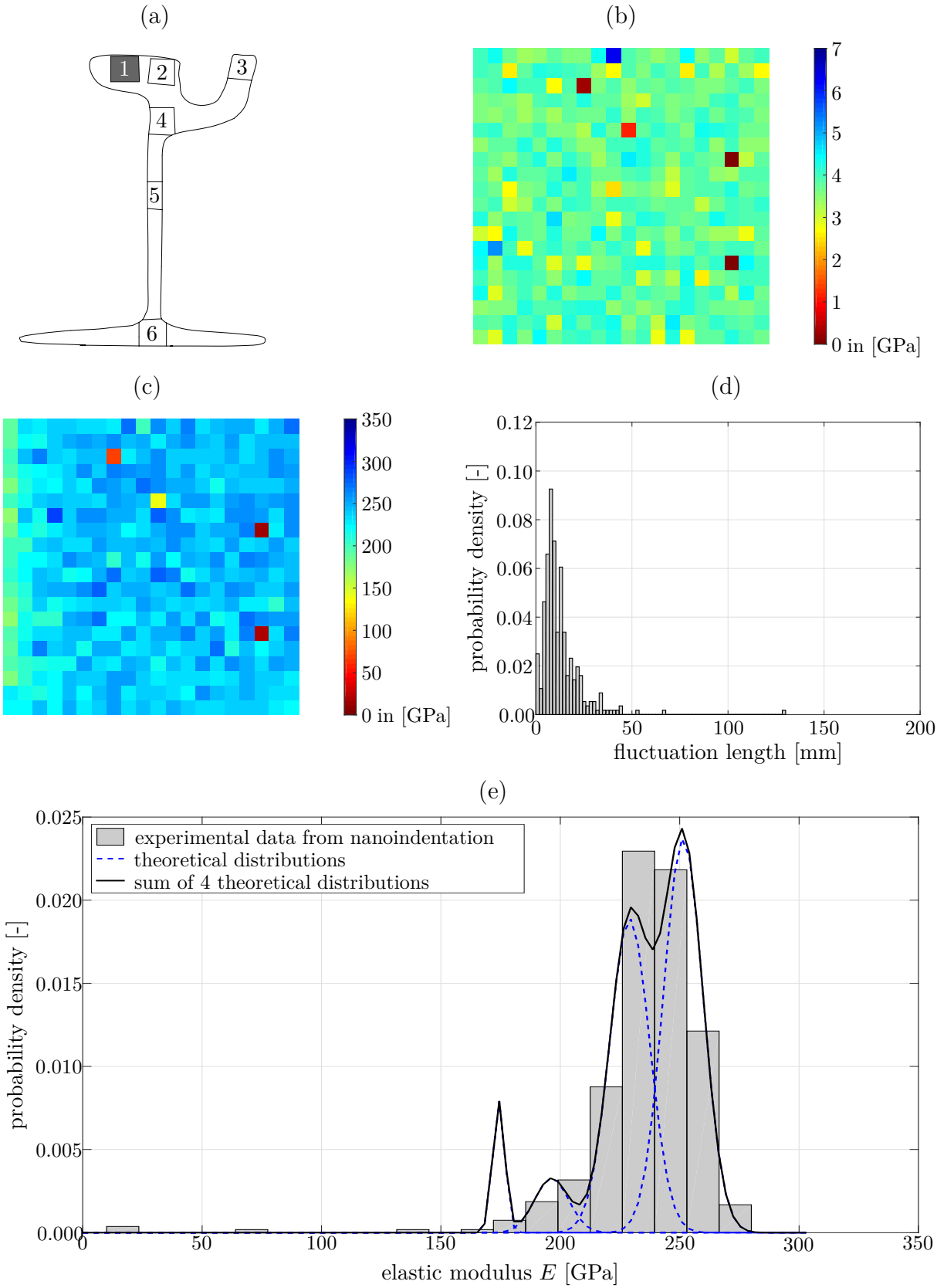

Fig. 4.20: Nanoindentation results for specimen IV-1; (a) definition of specimen position; (b) hardness and (c) Young's modulus distributions across the tested area; (d) histogram showing the fluctuation length of the Young's modulus; (e) probability density function of the Young's modulus, as well as fitting of the data by means of 4 Gaussian (theoretical) distribution

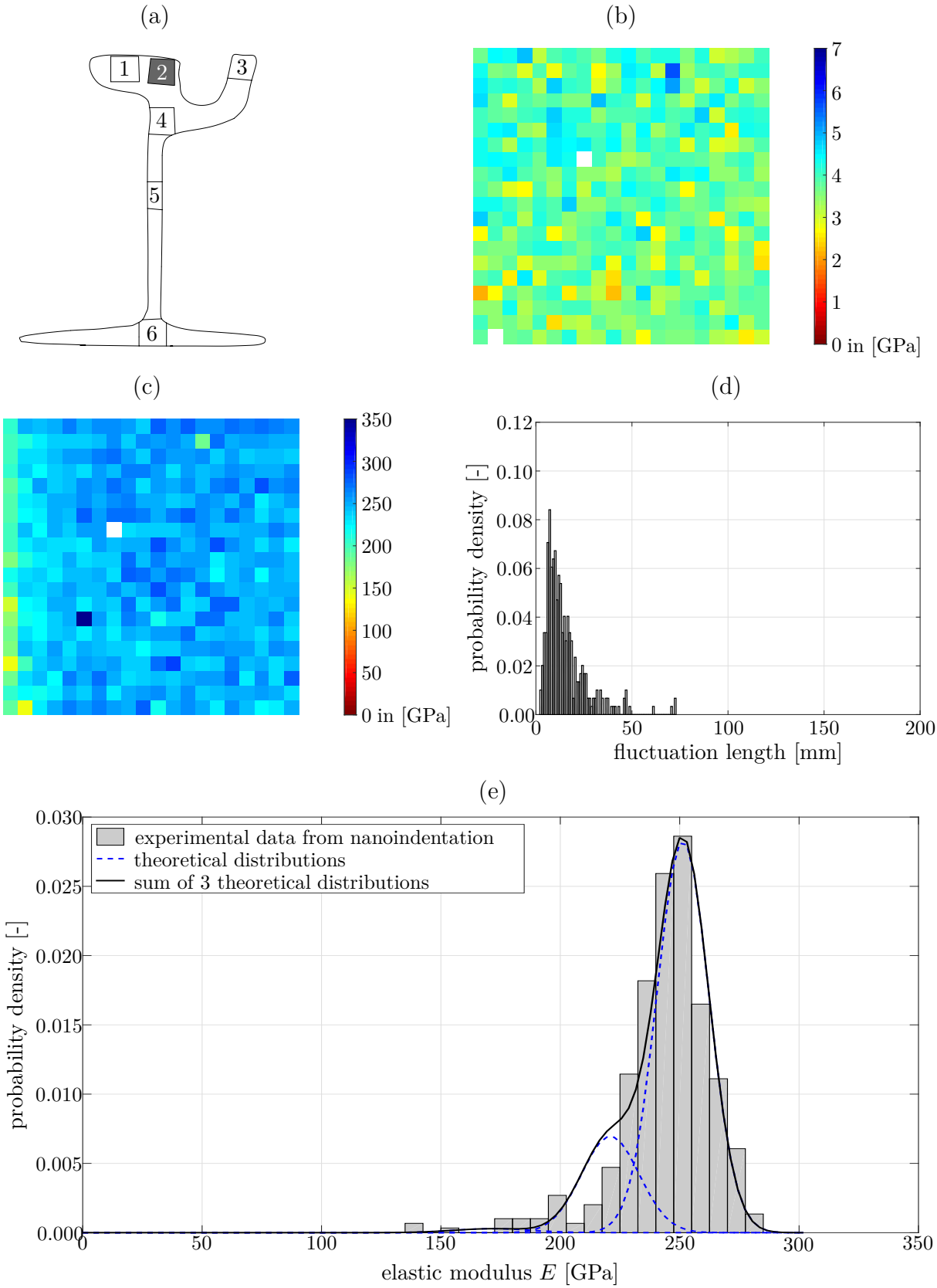

Fig. 4.21: Nanoindentation results for specimen IV-2; (a) definition of specimen position; (b) hardness and (c) Young's modulus distributions across the tested area; (d) histogram showing the fluctuation length of the Young's modulus; (e) probability density function of the Young's modulus, as well as fitting of the data by means of 3 Gaussian (theoretical) distribution

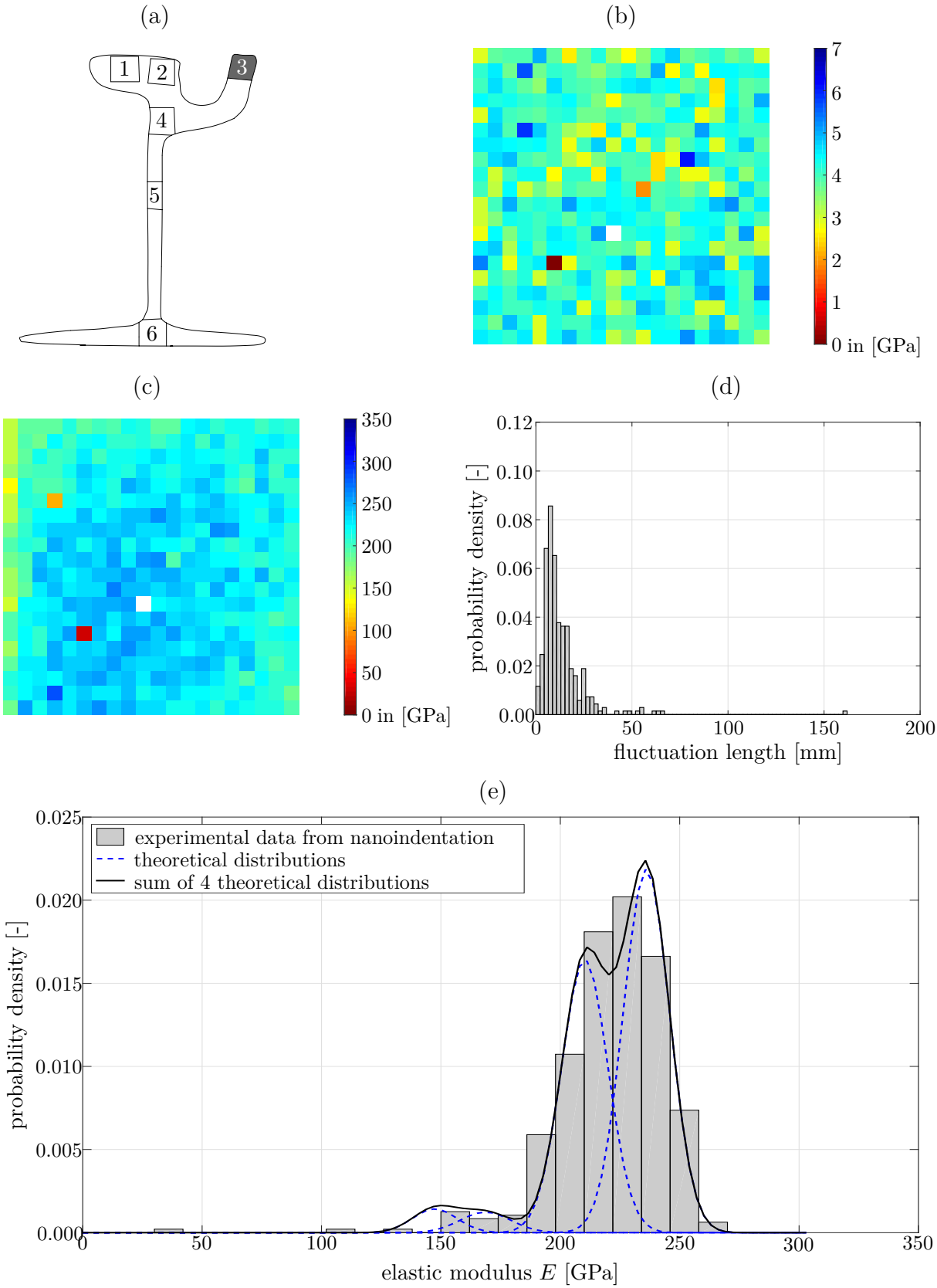

Fig. 4.22: Nanoindentation results for specimen IV-3; (a) definition of specimen position; (b) hardness and (c) Young's modulus distributions across the tested area; (d) histogram showing the fluctuation length of the Young's modulus; (e) probability density function of the Young's modulus, as well as fitting of the data by means of 4 Gaussian (theoretical) distribution

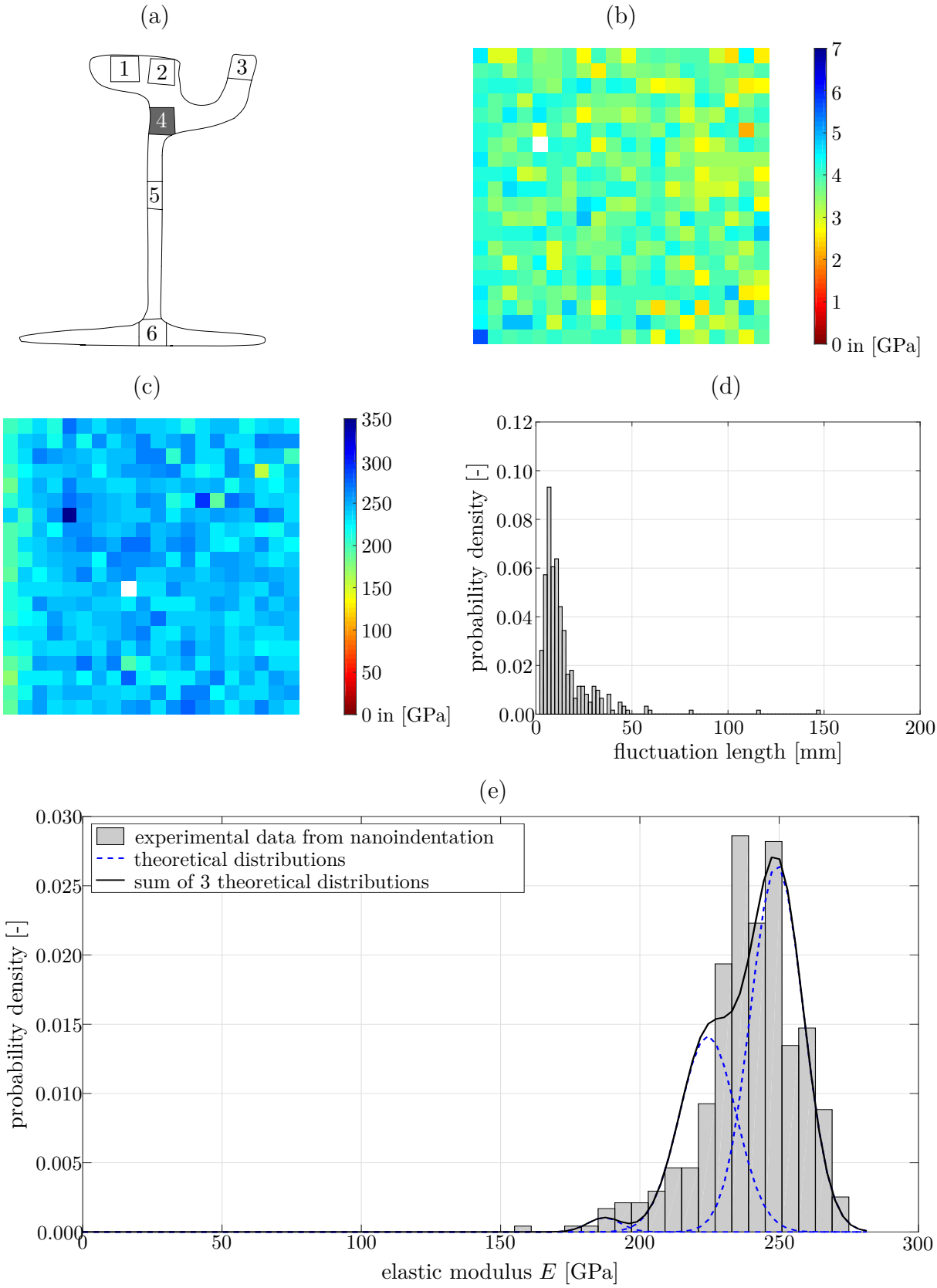

Fig. 4.23: Nanoindentation results for specimen IV-4; (a) definition of specimen position; (b) hardness and (c) Young's modulus distributions across the tested area; (d) histogram showing the fluctuation length of the Young's modulus; (e) probability density function of the Young's modulus, as well as fitting of the data by means of 3 Gaussian (theoretical) distribution

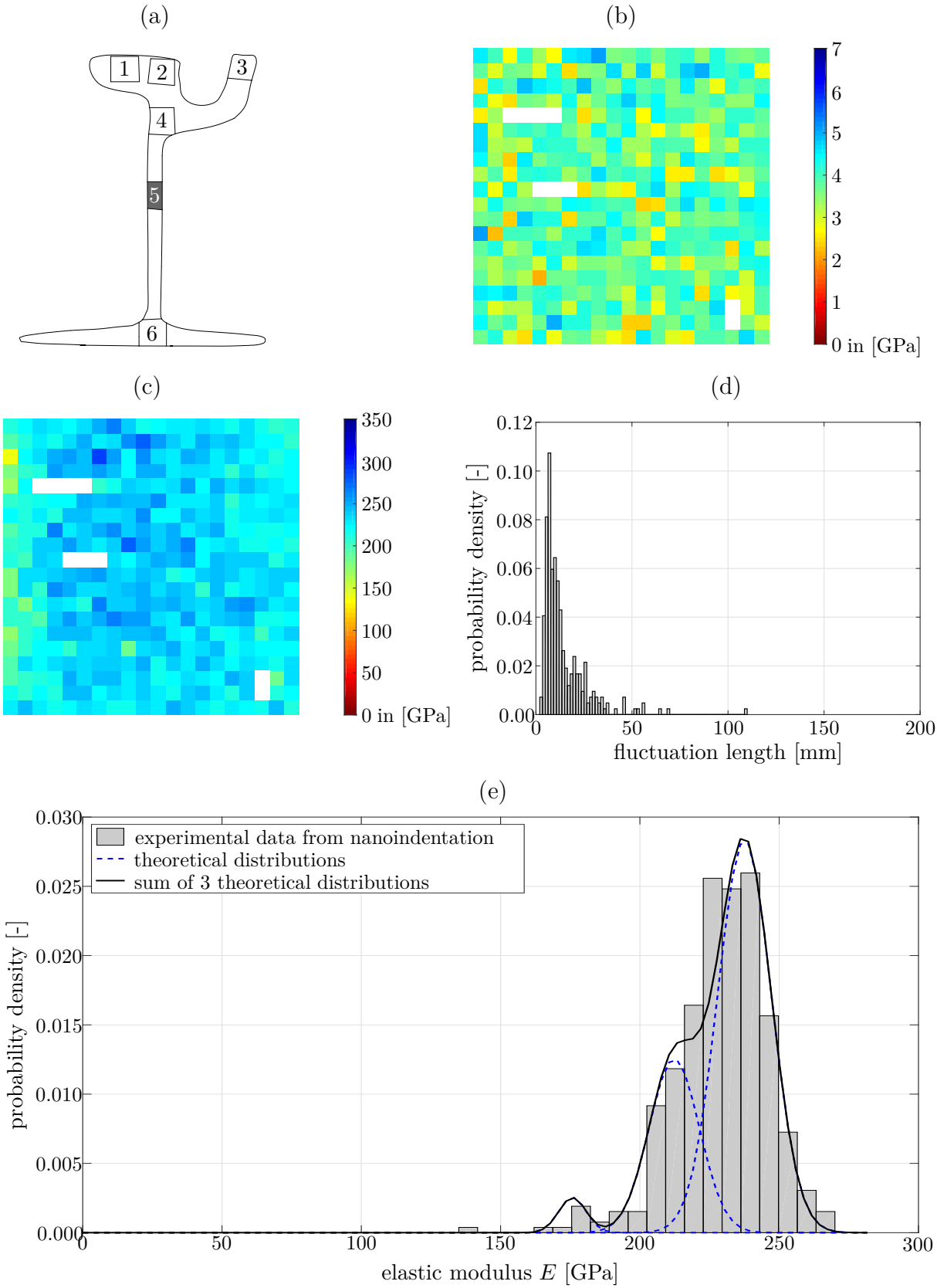

Fig. 4.24: Nanoindentation results for specimen IV-5; (a) definition of specimen position; (b) hardness and (c) Young's modulus distributions across the tested area; (d) histogram showing the fluctuation length of the Young's modulus; (e) probability density function of the Young's modulus, as well as fitting of the data by means of 3 Gaussian (theoretical) distribution

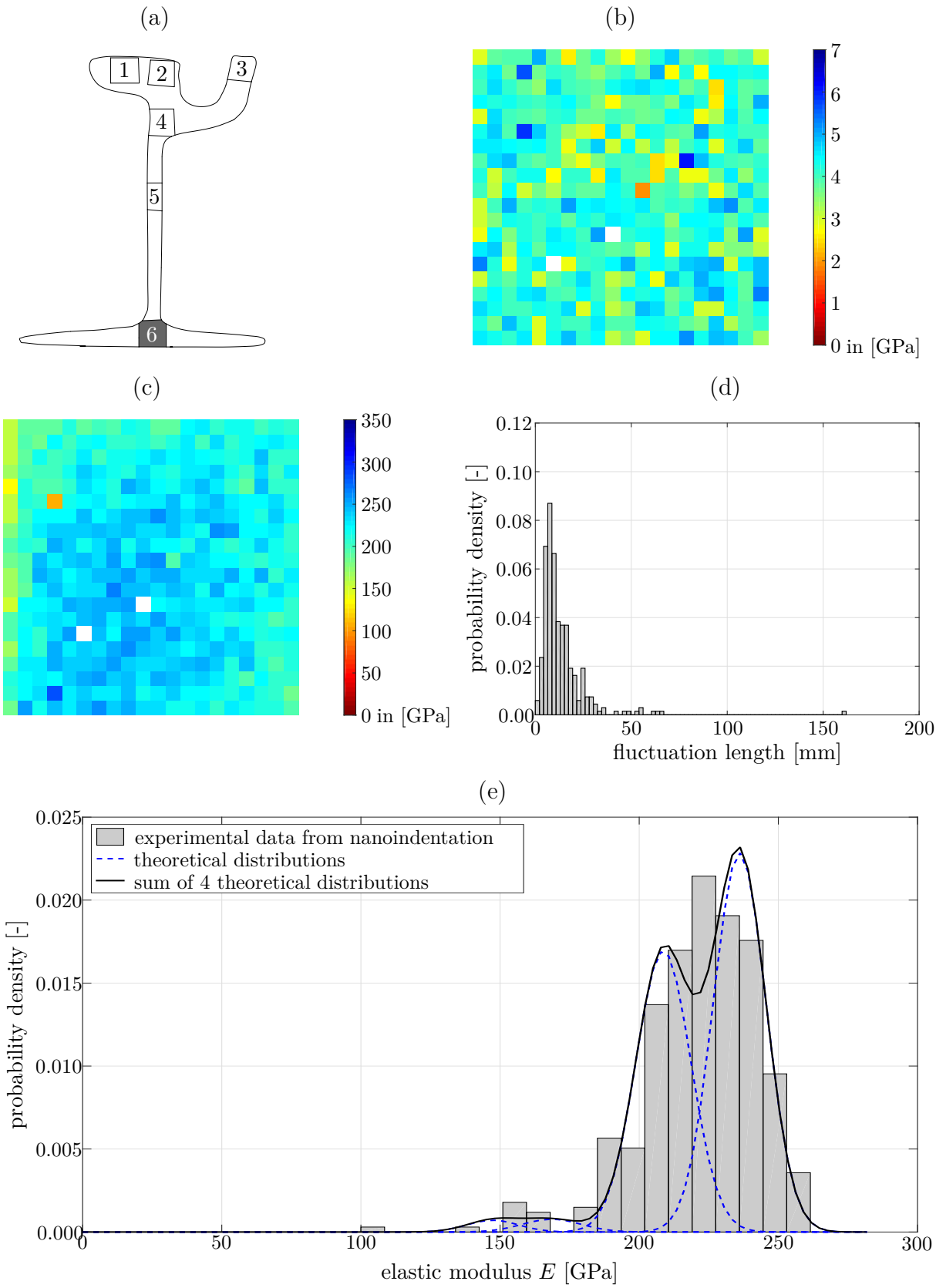

Fig. 4.25: Nanoindentation results for specimen IV-6; (a) definition of specimen position; (b) hardness and (c) Young's modulus distributions across the tested area; (d) histogram showing the fluctuation length of the Young's modulus; (e) probability density function of the Young's modulus, as well as fitting of the data by means of 4 Gaussian (theoretical) distribution

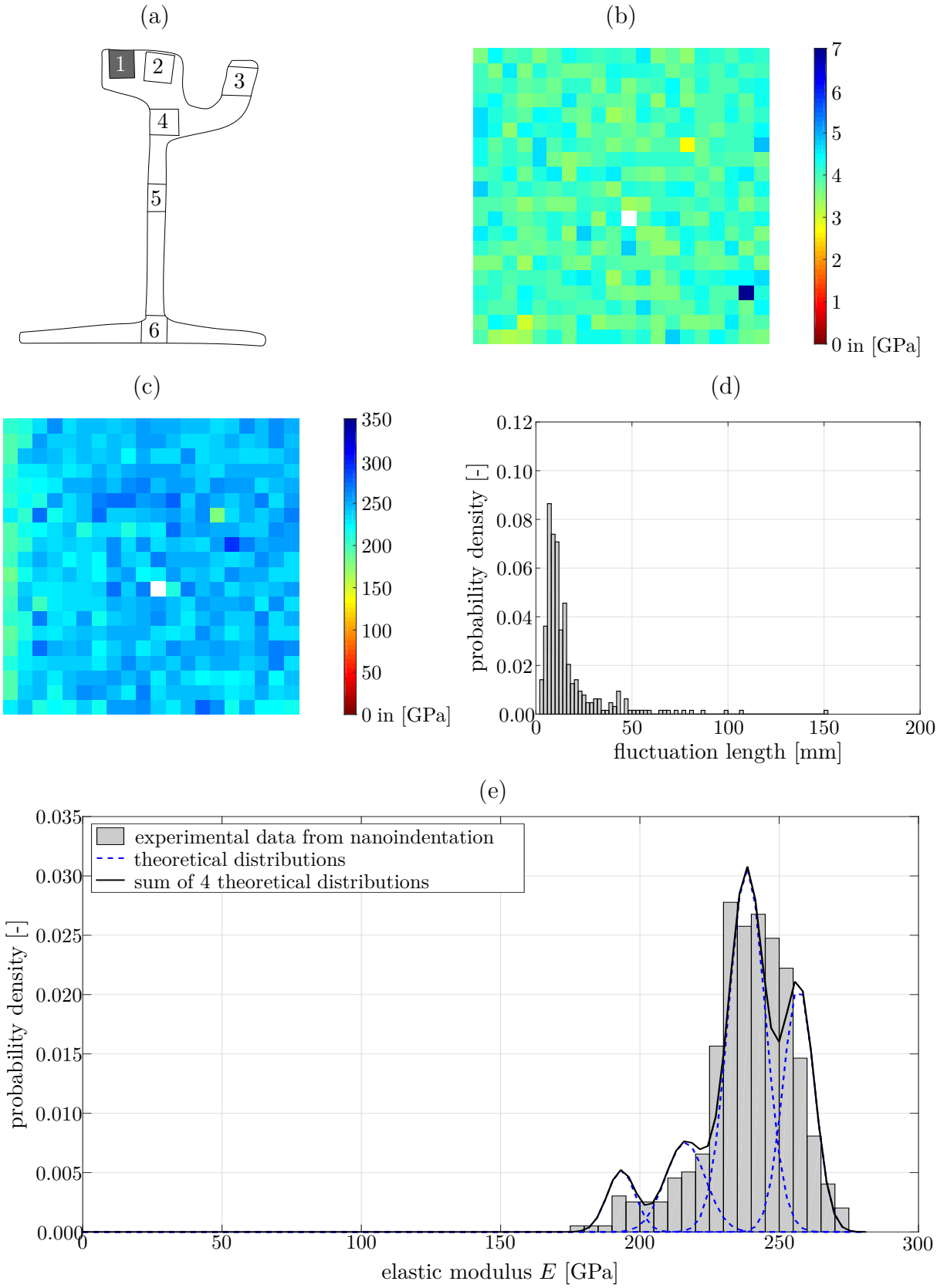

Fig. 4.26: Nanoindentation results for specimen V-1; (a) definition of specimen position; (b) hardness and (c) Young's modulus distributions across the tested area; (d) histogram showing the fluctuation length of the Young's modulus; (e) probability density function of the Young's modulus, as well as fitting of the data by means of 4 Gaussian (theoretical) distribution

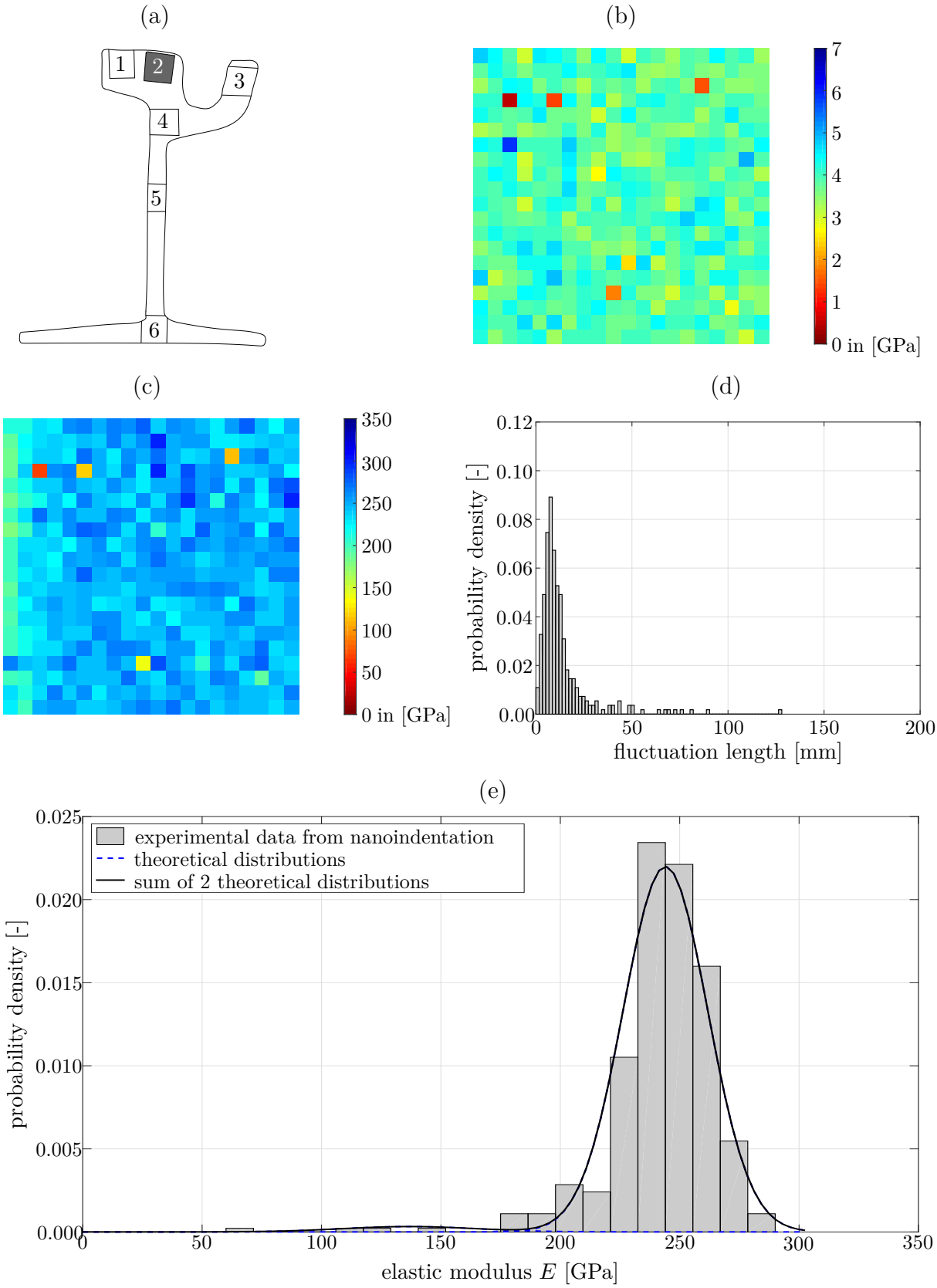

Fig. 4.27: Nanoindentation results for specimen V-2; (a) definition of specimen position; (b) hardness and (c) Young's modulus distributions across the tested area; (d) histogram showing the fluctuation length of the Young's modulus; (e) probability density function of the Young's modulus, as well as fitting of the data by means of 2 Gaussian (theoretical) distribution

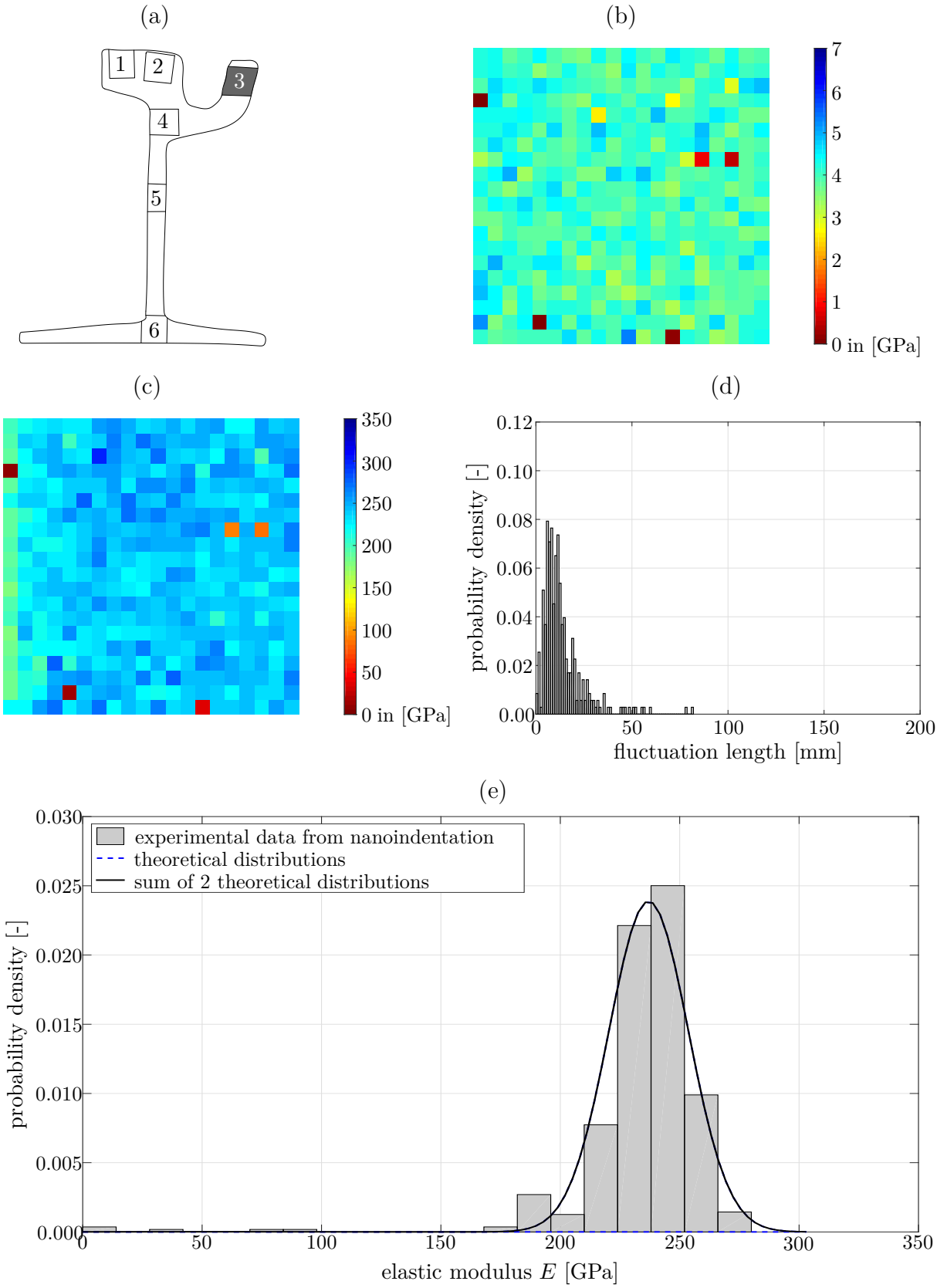

Fig. 4.28: Nanoindentation results for specimen V-3; (a) definition of specimen position; (b) hardness and (c) Young's modulus distributions across the tested area; (d) histogram showing the fluctuation length of the Young's modulus; (e) probability density function of the Young's modulus, as well as fitting of the data by means of 2 Gaussian (theoretical) distribution

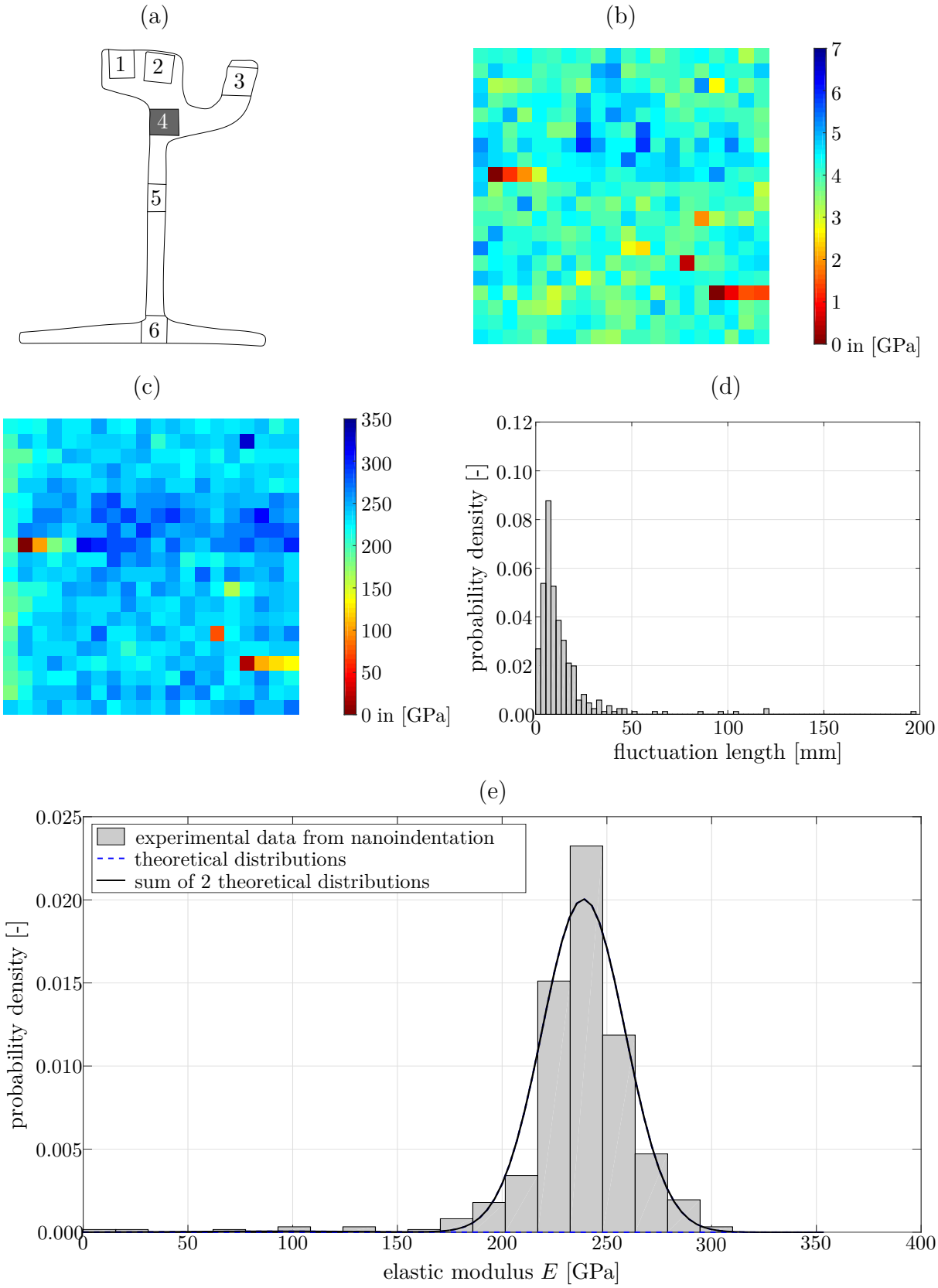

Fig. 4.29: Nanoindentation results for specimen V-4; (a) definition of specimen position; (b) hardness and (c) Young's modulus distributions across the tested area; (d) histogram showing the fluctuation length of the Young's modulus; (e) probability density function of the Young's modulus, as well as fitting of the data by means of 2 Gaussian (theoretical) distribution

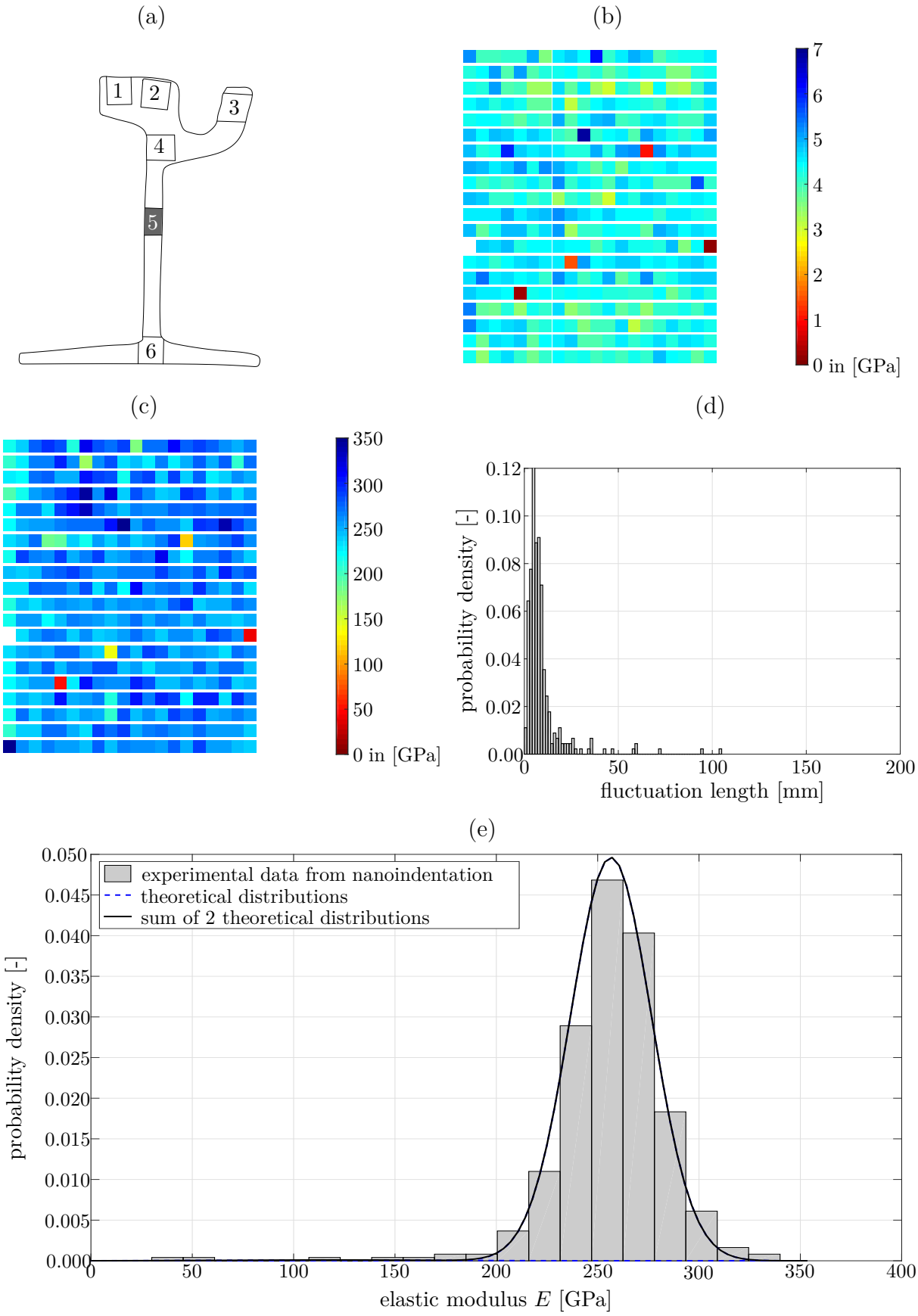

Fig. 4.30: Nanoindentation results for specimen V-5; (a) definition of specimen position; (b) hardness and (c) Young's modulus distributions across the tested area; (d) histogram showing the fluctuation length of the Young's modulus; (e) probability density function of the Young's modulus, as well as fitting of the data by means of 2 Gaussian (theoretical) distribution

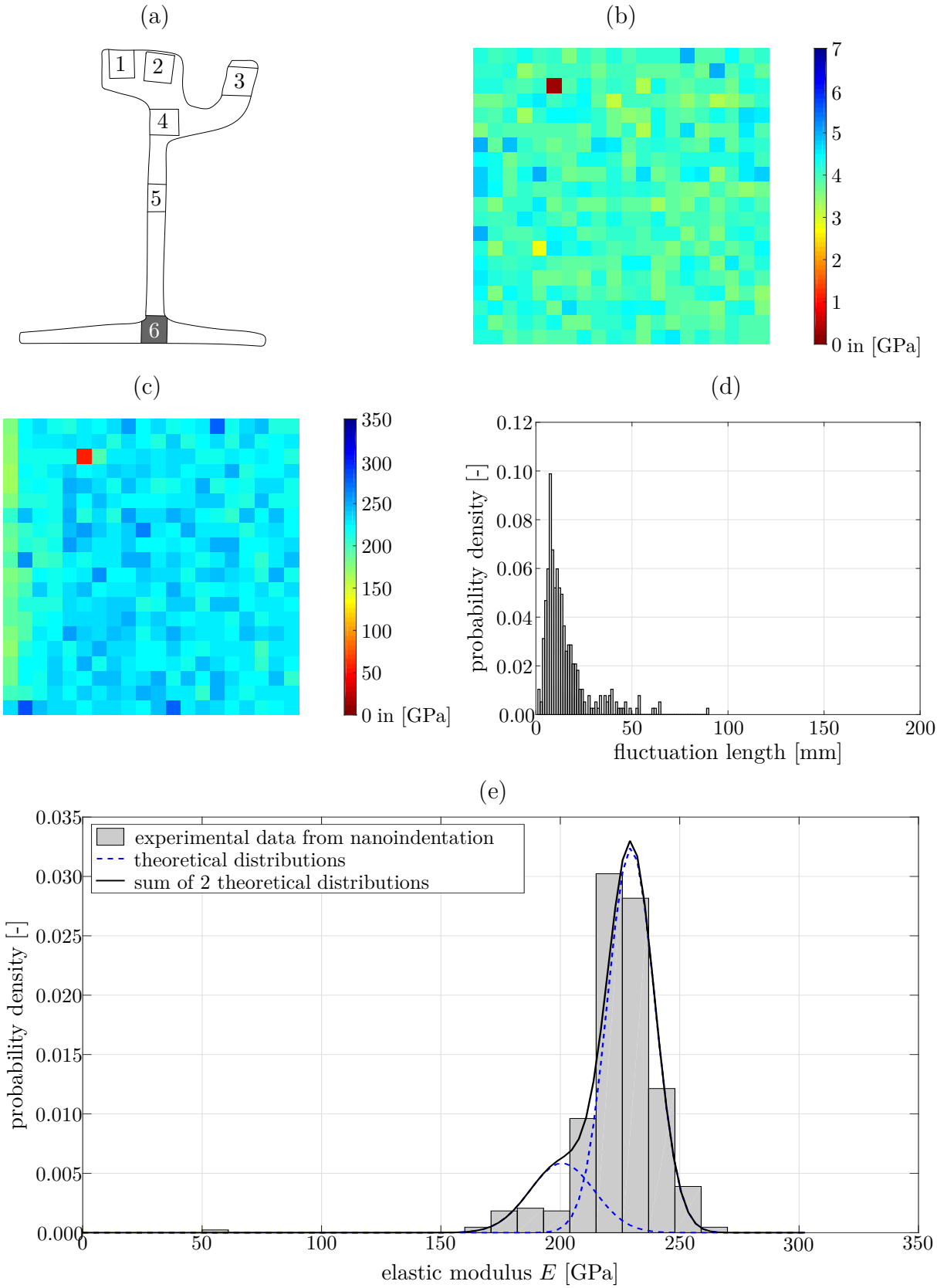

Fig. 4.31: Nanoindentation results for specimen V-6; (a) definition of specimen position; (b) hardness and (c) Young's modulus distributions across the tested area; (d) histogram showing the fluctuation length of the Young's modulus; (e) probability density function of the Young's modulus, as well as fitting of the data by means of 2 Gaussian (theoretical) distribution

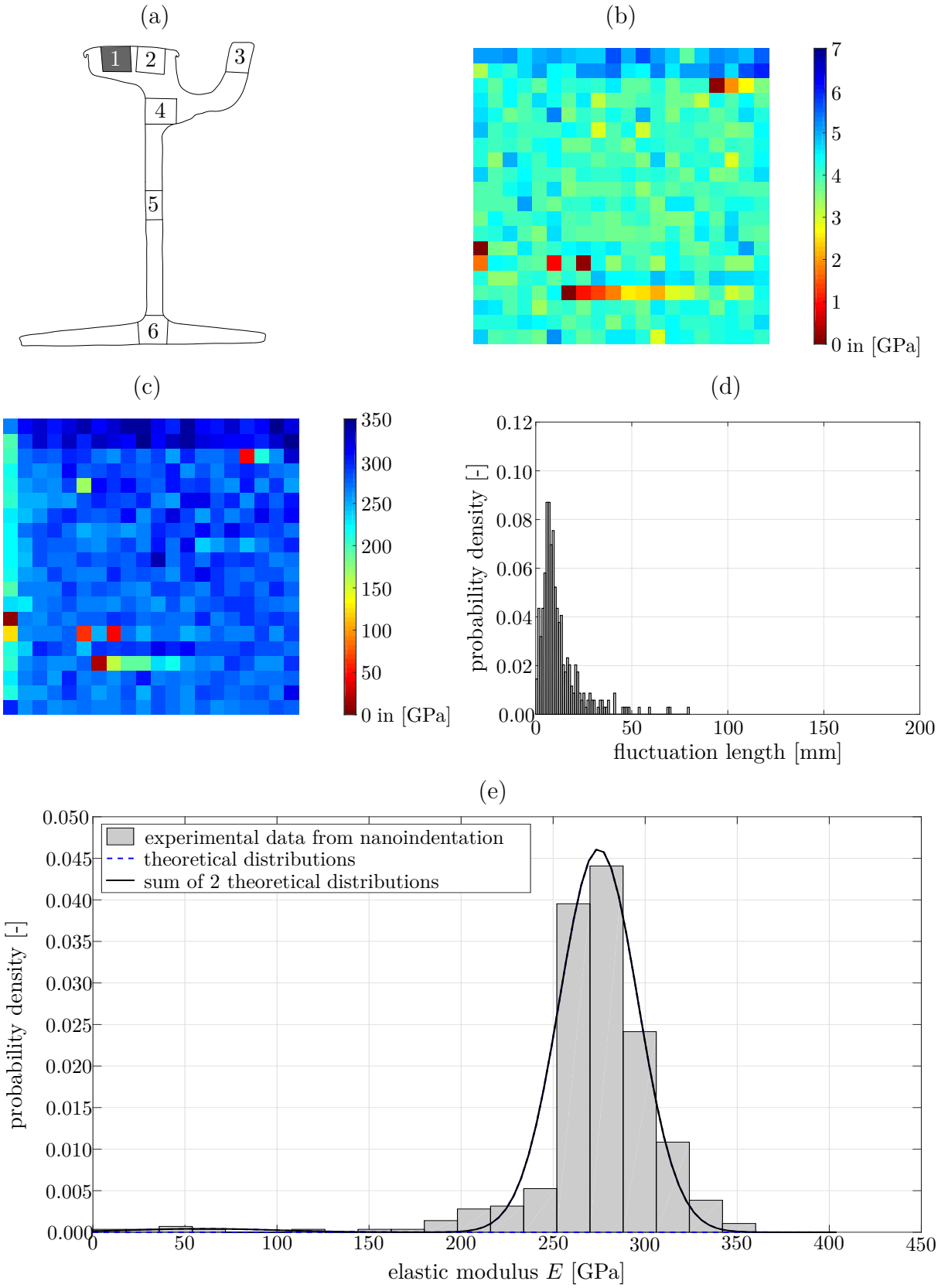

Fig. 4.32: Nanoindentation results for specimen VI-1; (a) definition of specimen position; (b) hardness and (c) Young's modulus distributions across the tested area; (d) histogram showing the fluctuation length of the Young's modulus; (e) probability density function of the Young's modulus, as well as fitting of the data by means of 2 Gaussian (theoretical) distribution

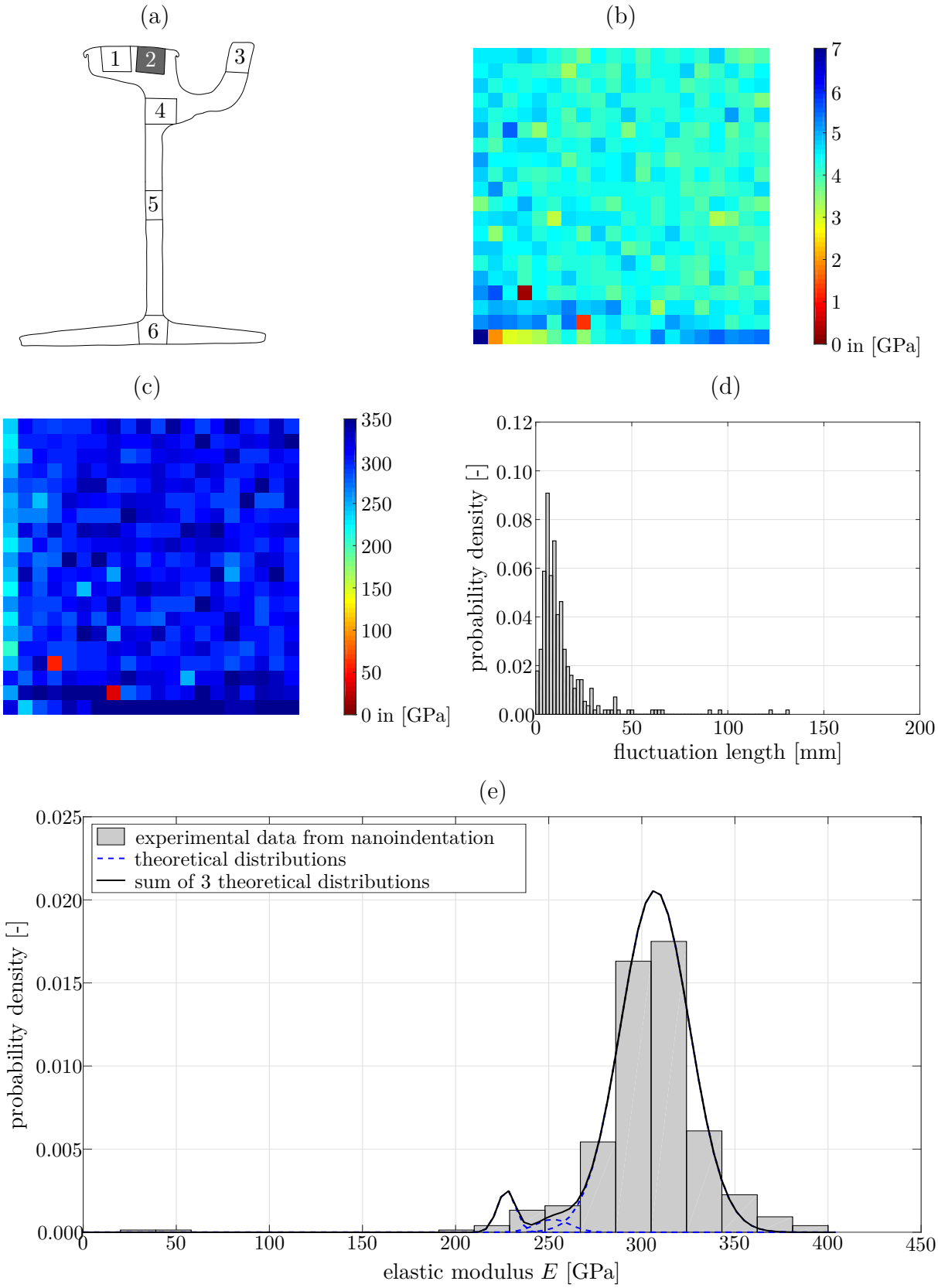

Fig. 4.33: Nanoindentation results for specimen VI-2; (a) definition of specimen position; (b) hardness and (c) Young's modulus distributions across the tested area; (d) histogram showing the fluctuation length of the Young's modulus; (e) probability density function of the Young's modulus, as well as fitting of the data by means of 3 Gaussian (theoretical) distribution

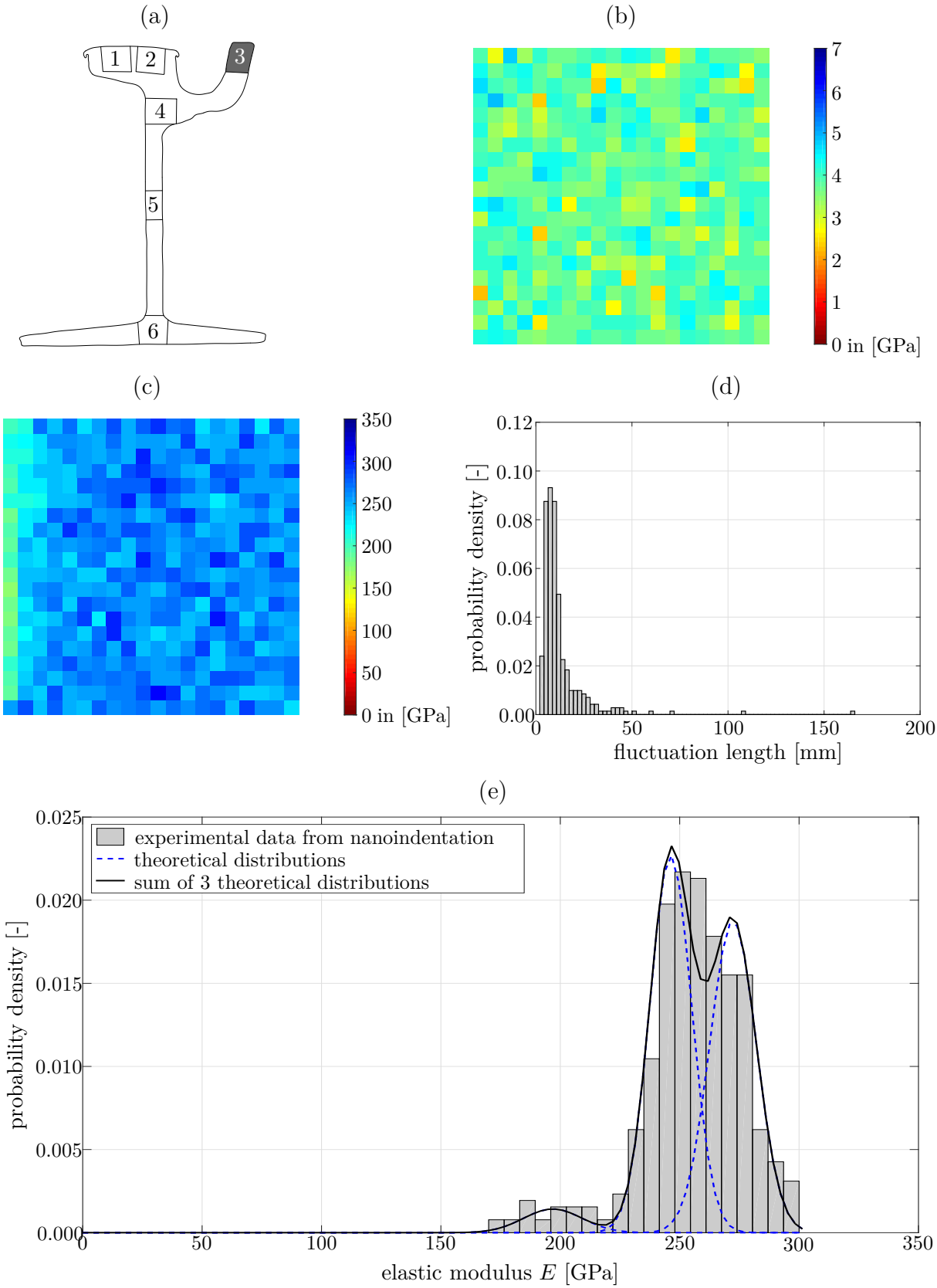

Fig. 4.34: Nanoindentation results for specimen VI-3; (a) definition of specimen position; (b) hardness and (c) Young's modulus distributions across the tested area; (d) histogram showing the fluctuation length of the Young's modulus; (e) probability density function of the Young's modulus, as well as fitting of the data by means of 3 Gaussian (theoretical) distribution

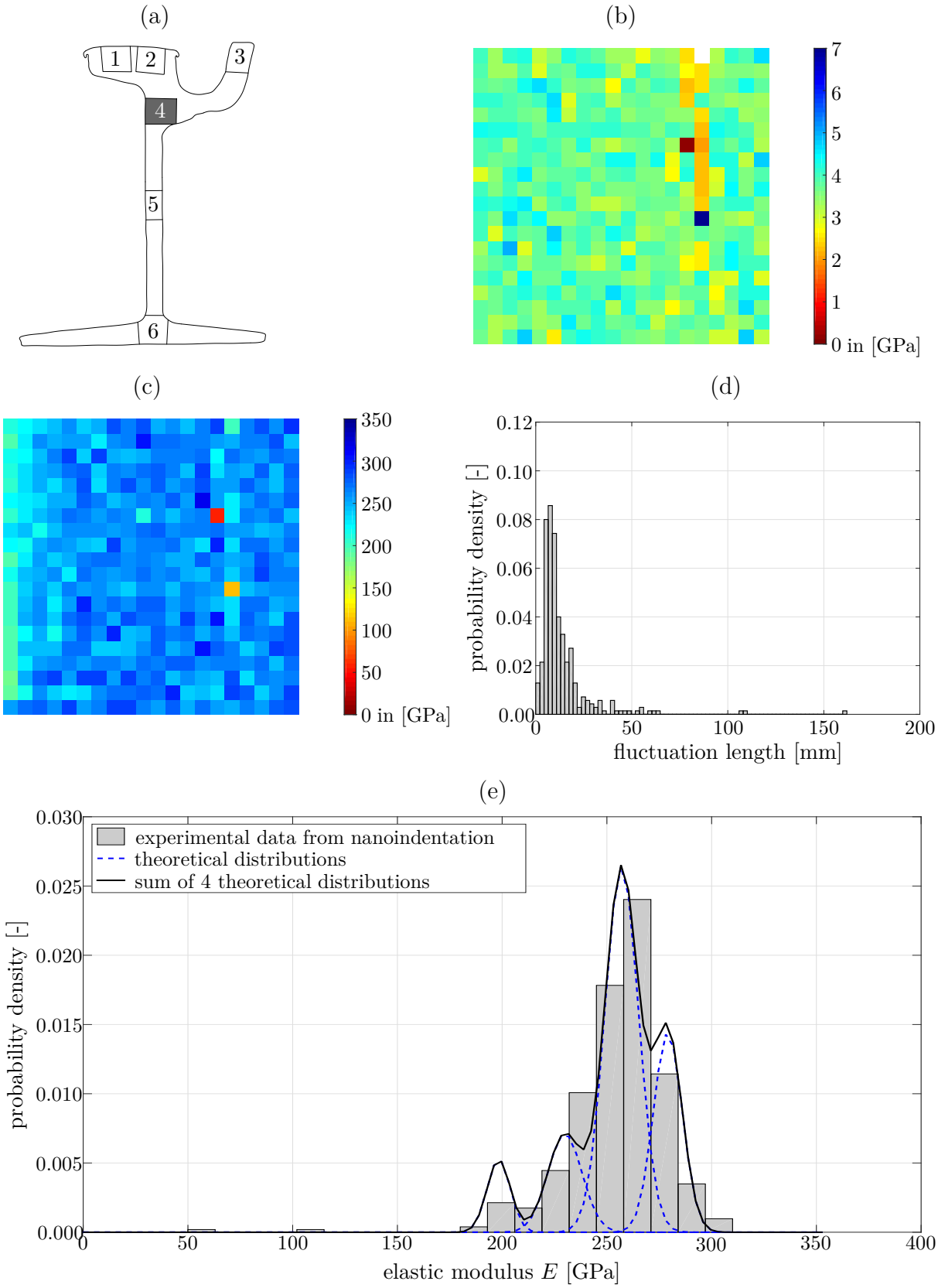

Fig. 4.35: Nanoindentation results for specimen VI-4; (a) definition of specimen position; (b) hardness and (c) Young's modulus distributions across the tested area; (d) histogram showing the fluctuation length of the Young's modulus; (e) probability density function of the Young's modulus, as well as fitting of the data by means of 4 Gaussian (theoretical) distribution

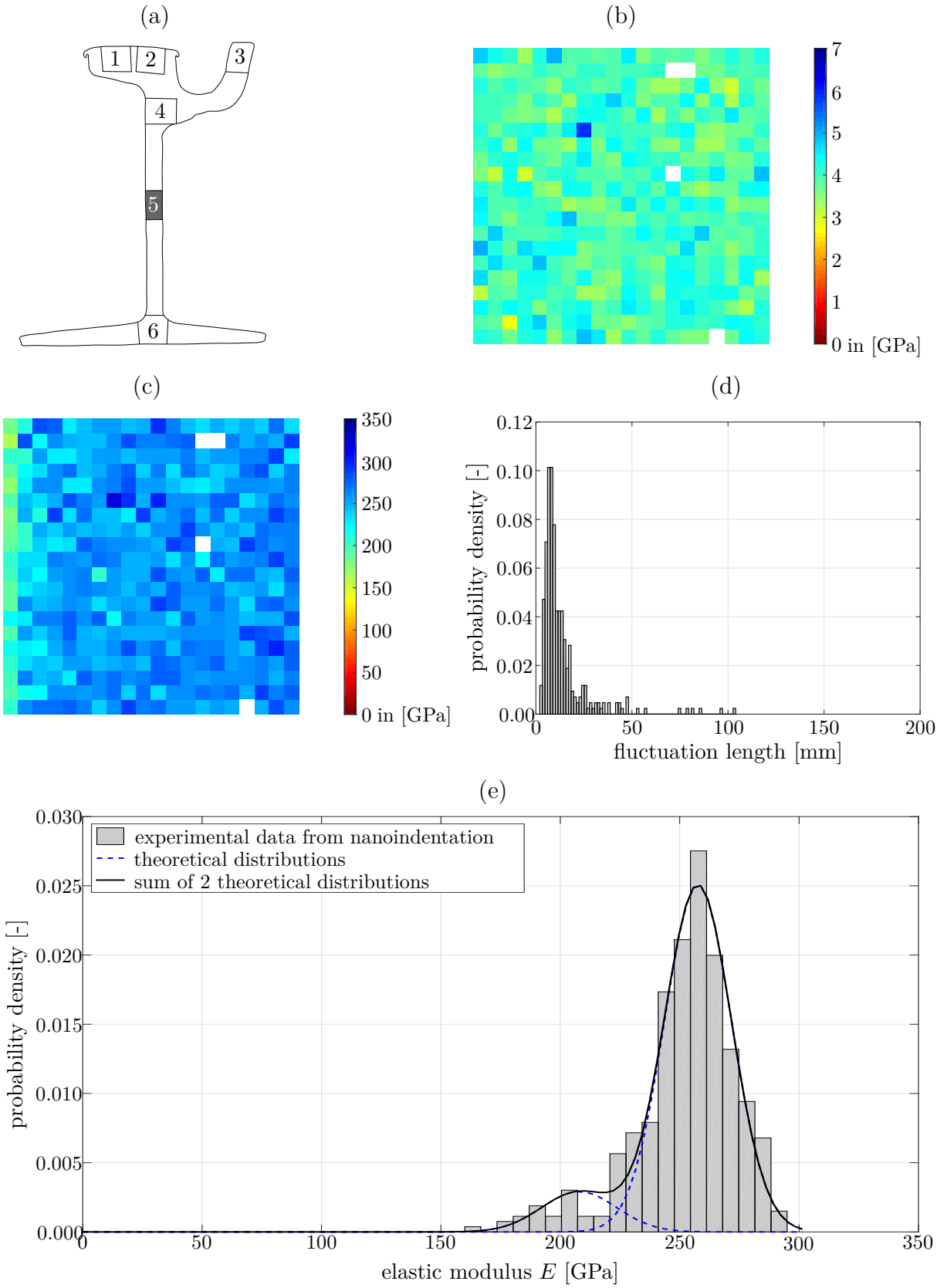

Fig. 4.36: Nanoindentation results for specimen VI-5; (a) definition of specimen position; (b) hardness and (c) Young's modulus distributions across the tested area; (d) histogram showing the fluctuation length of the Young's modulus; (e) probability density function of the Young's modulus, as well as fitting of the data by means of 2 Gaussian (theoretical) distribution

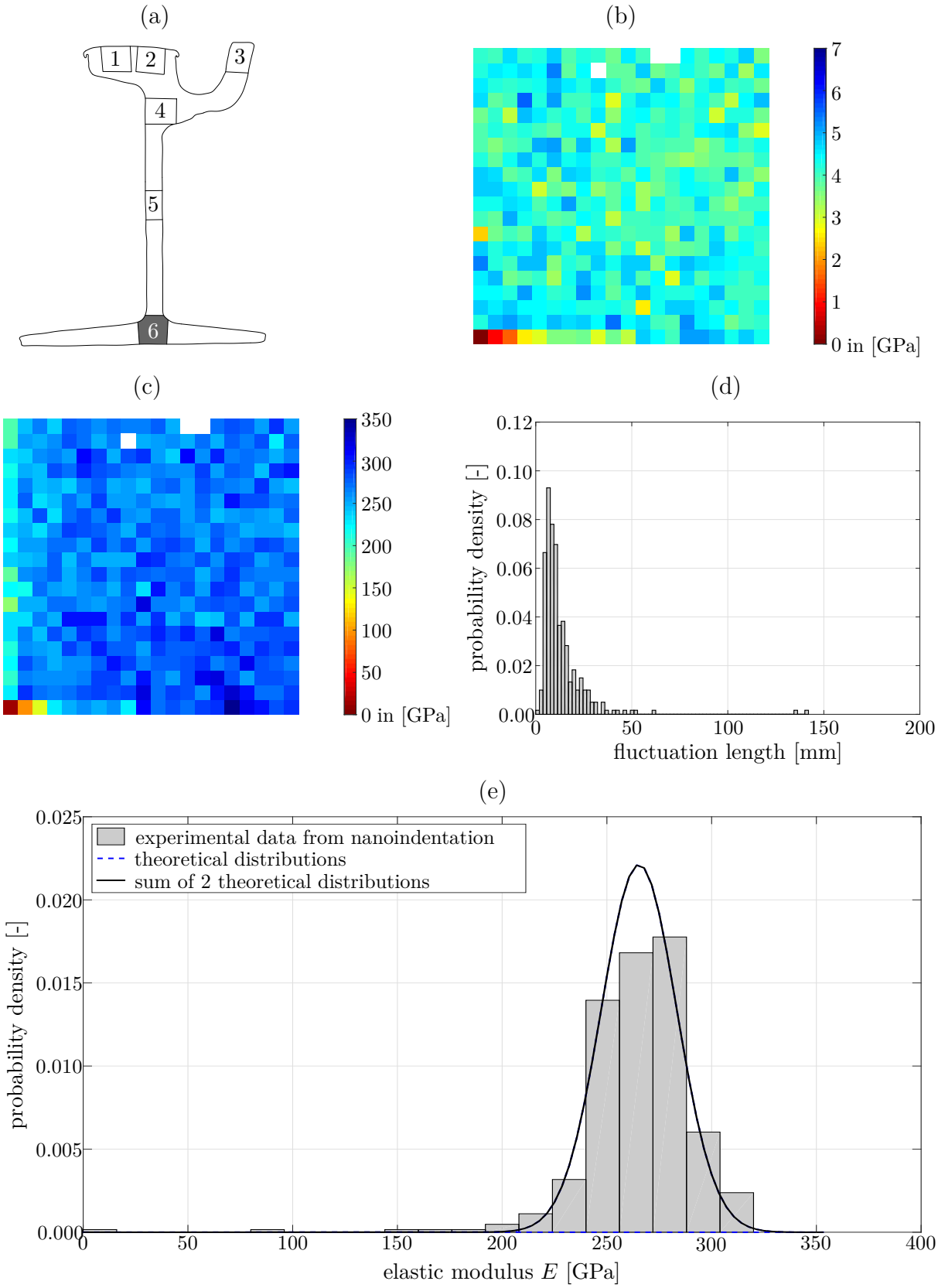

Fig. 4.37: Nanoindentation results for specimen VI-6; (a) definition of specimen position; (b) hardness and (c) Young's modulus distributions across the tested area; (d) histogram showing the fluctuation length of the Young's modulus; (e) probability density function of the Young's modulus, as well as fitting of the data by means of 2 Gaussian (theoretical) distribution

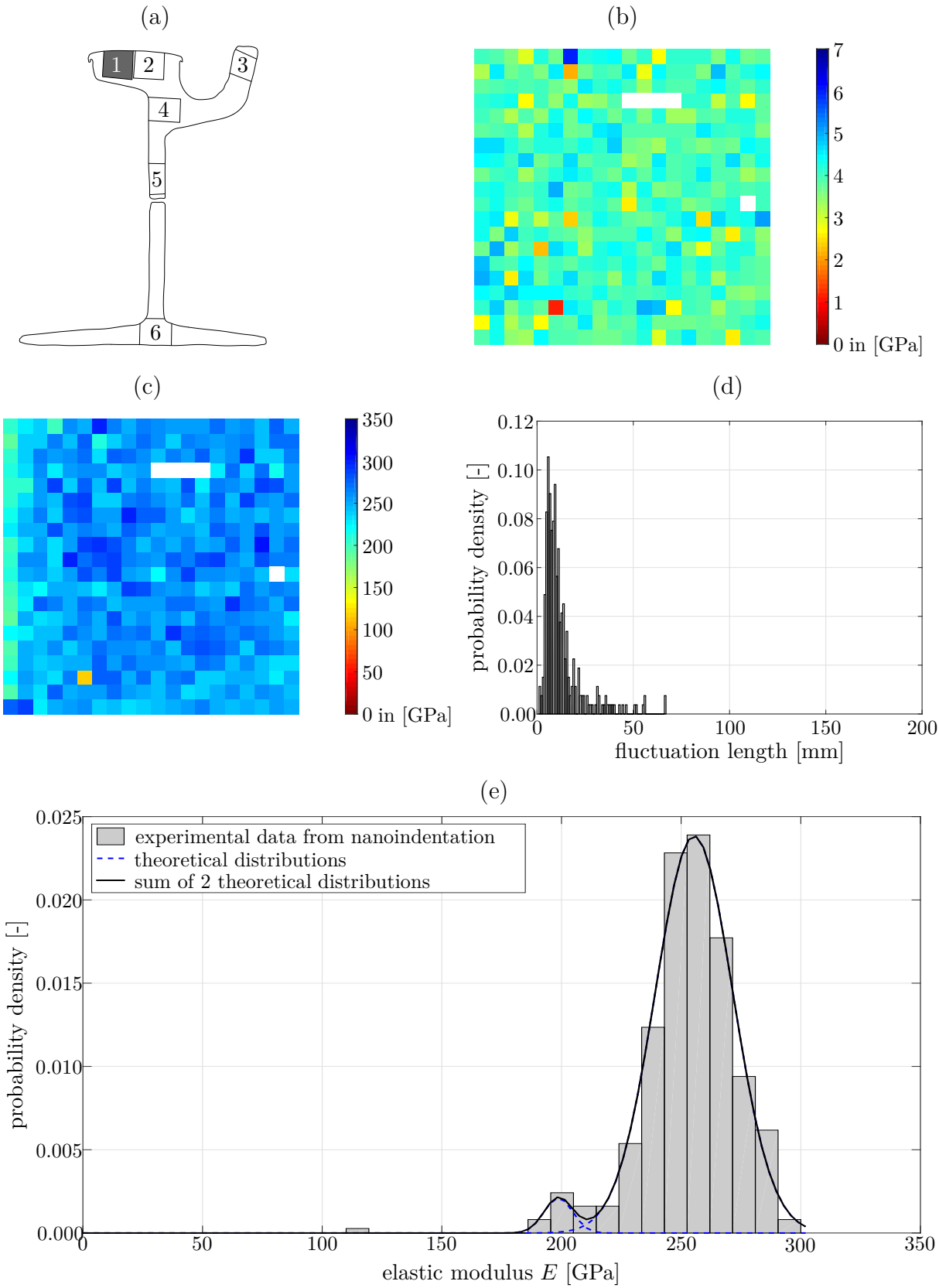

Fig. 4.38: Nanoindentation results for specimen VII-1; (a) definition of specimen position; (b) hardness and (c) Young's modulus distributions across the tested area; (d) histogram showing the fluctuation length of the Young's modulus; (e) probability density function of the Young's modulus, as well as fitting of the data by means of 2 Gaussian (theoretical) distribution

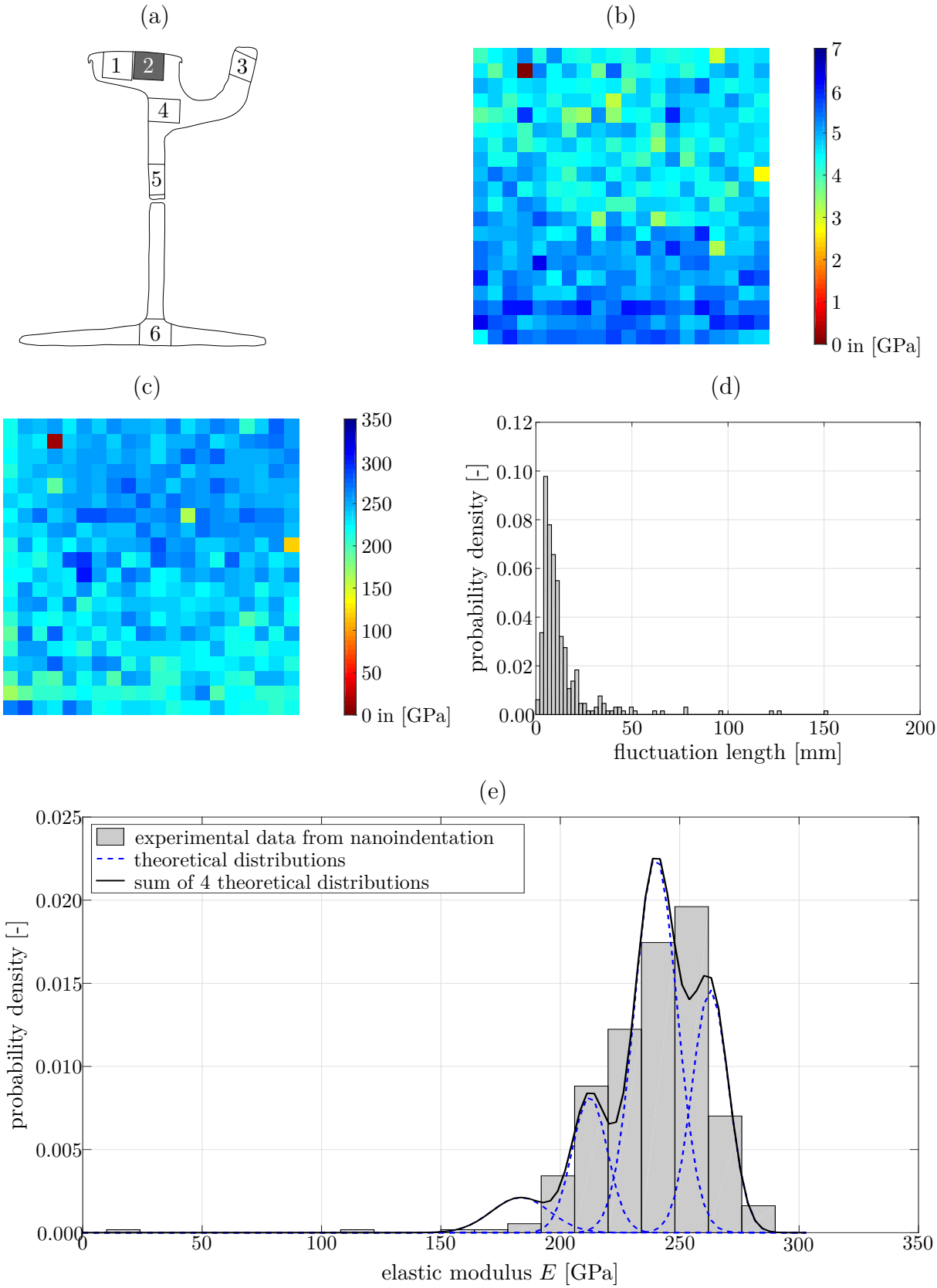

Fig. 4.39: Nanoindentation results for specimen VII-2; (a) definition of specimen position; (b) hardness and (c) Young's modulus distributions across the tested area; (d) histogram showing the fluctuation length of the Young's modulus; (e) probability density function of the Young's modulus, as well as fitting of the data by means of 4 Gaussian (theoretical) distribution

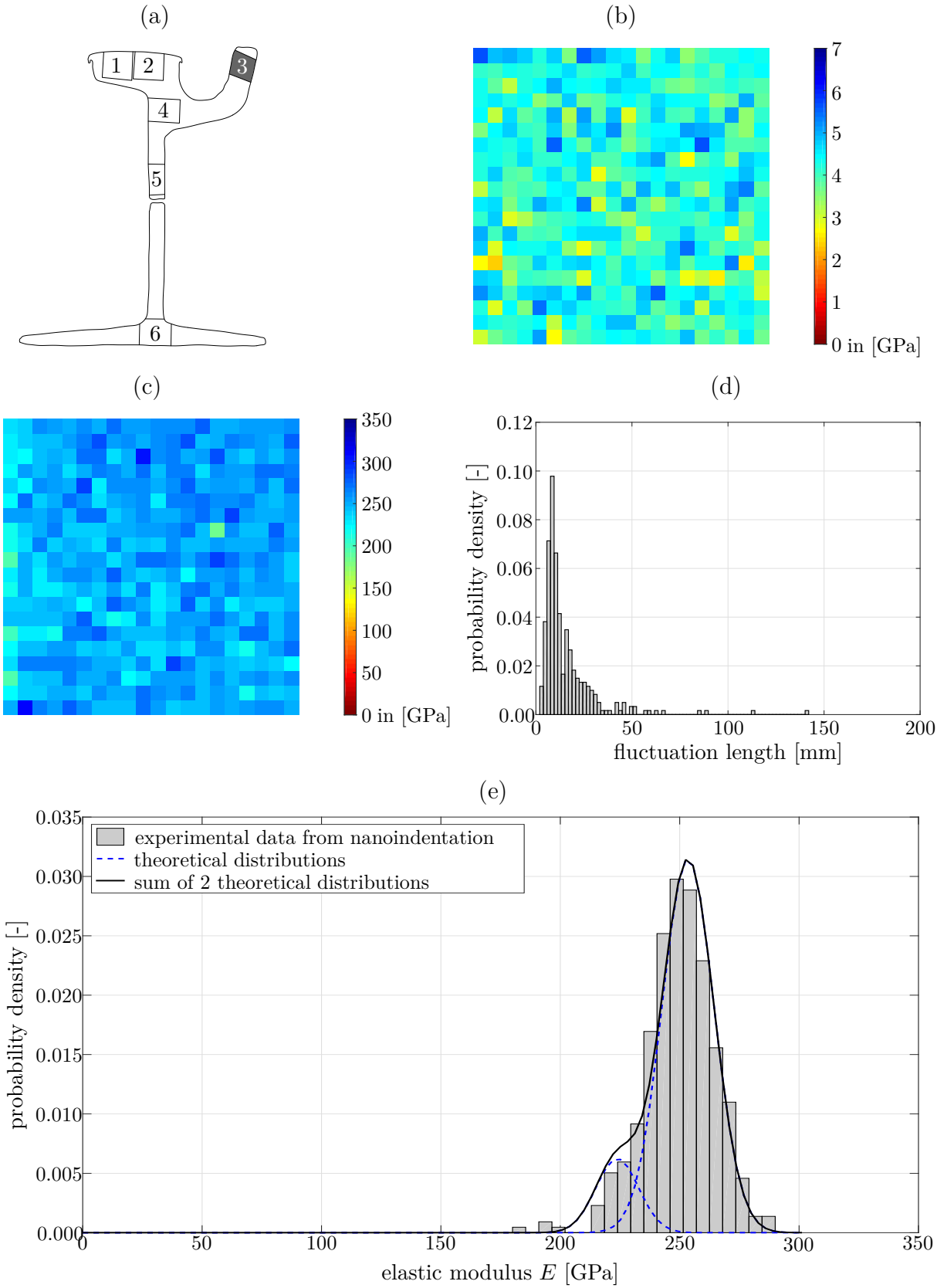

Fig. 4.40: Nanoindentation results for specimen VII-3; (a) definition of specimen position; (b) hardness and (c) Young's modulus distributions across the tested area; (d) histogram showing the fluctuation length of the Young's modulus; (e) probability density function of the Young's modulus, as well as fitting of the data by means of 2 Gaussian (theoretical) distribution

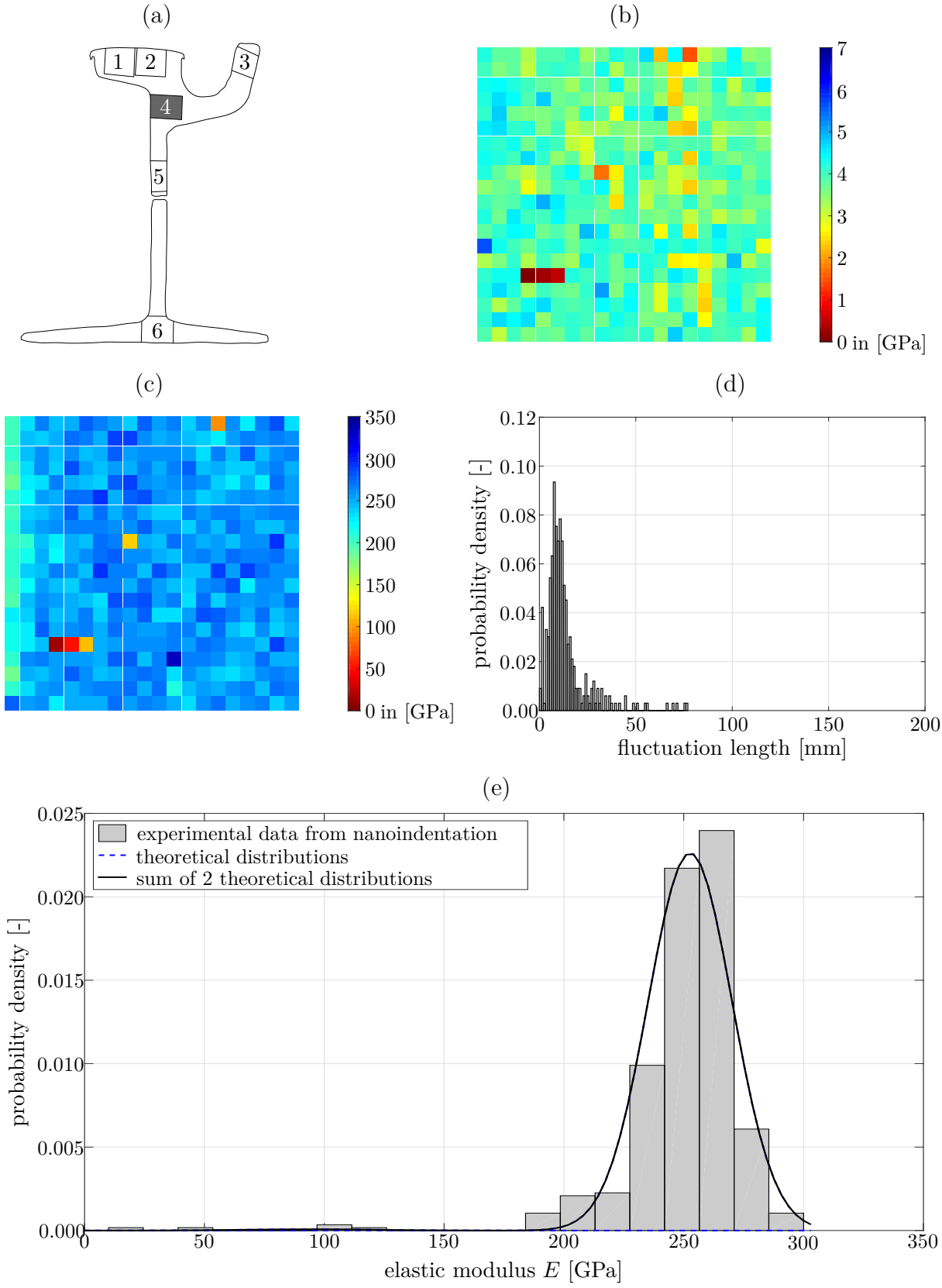

Fig. 4.41: Nanoindentation results for specimen VII-4; (a) definition of specimen position; (b) hardness and (c) Young's modulus distributions across the tested area; (d) histogram showing the fluctuation length of the Young's modulus; (e) probability density function of the Young's modulus, as well as fitting of the data by means of 2 Gaussian (theoretical) distribution

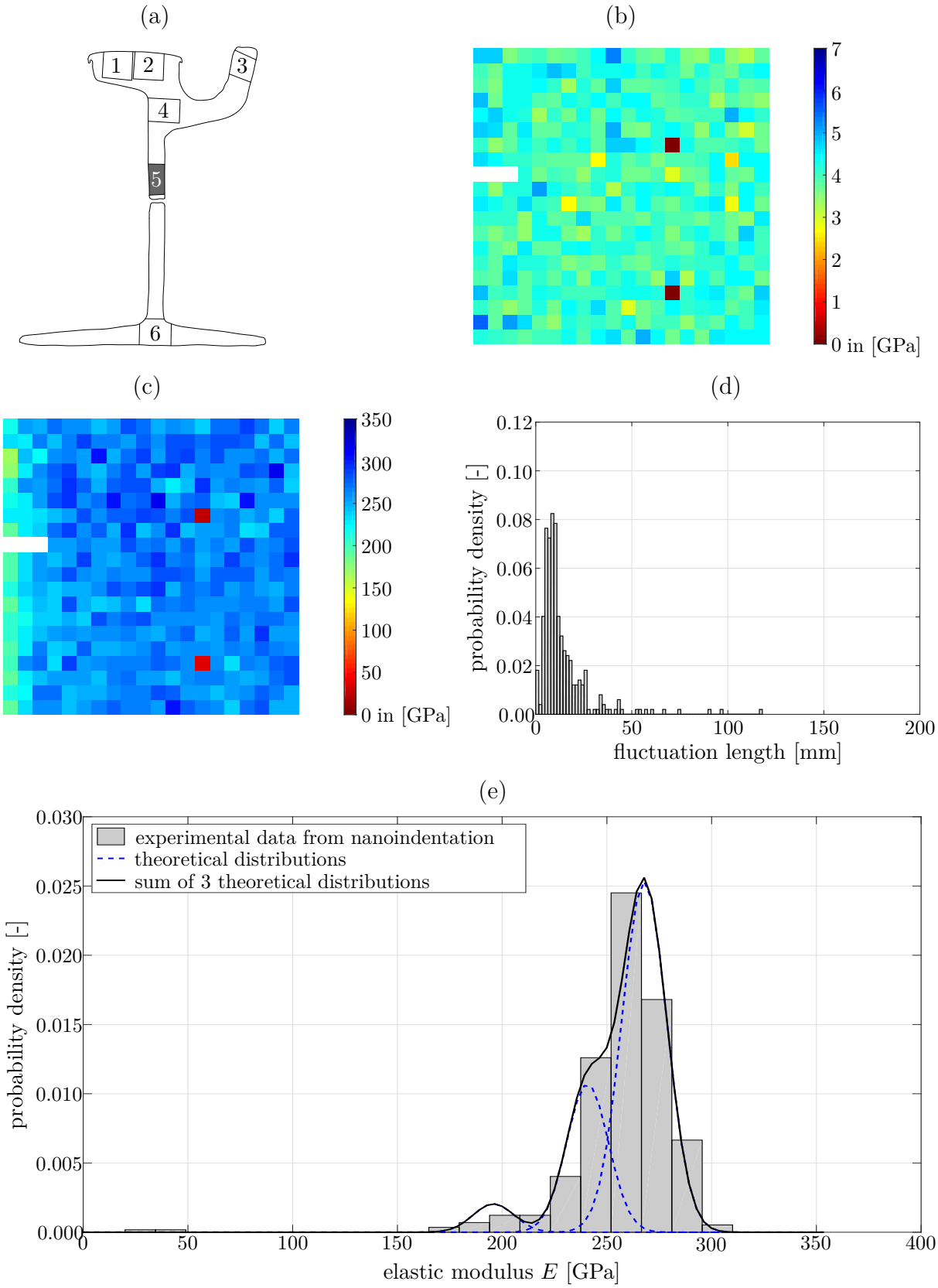

Fig. 4.42: Nanoindentation results for specimen VII-5; (a) definition of specimen position; (b) hardness and (c) Young's modulus distributions across the tested area; (d) histogram showing the fluctuation length of the Young's modulus; (e) probability density function of the Young's modulus, as well as fitting of the data by means of 3 Gaussian (theoretical) distribution

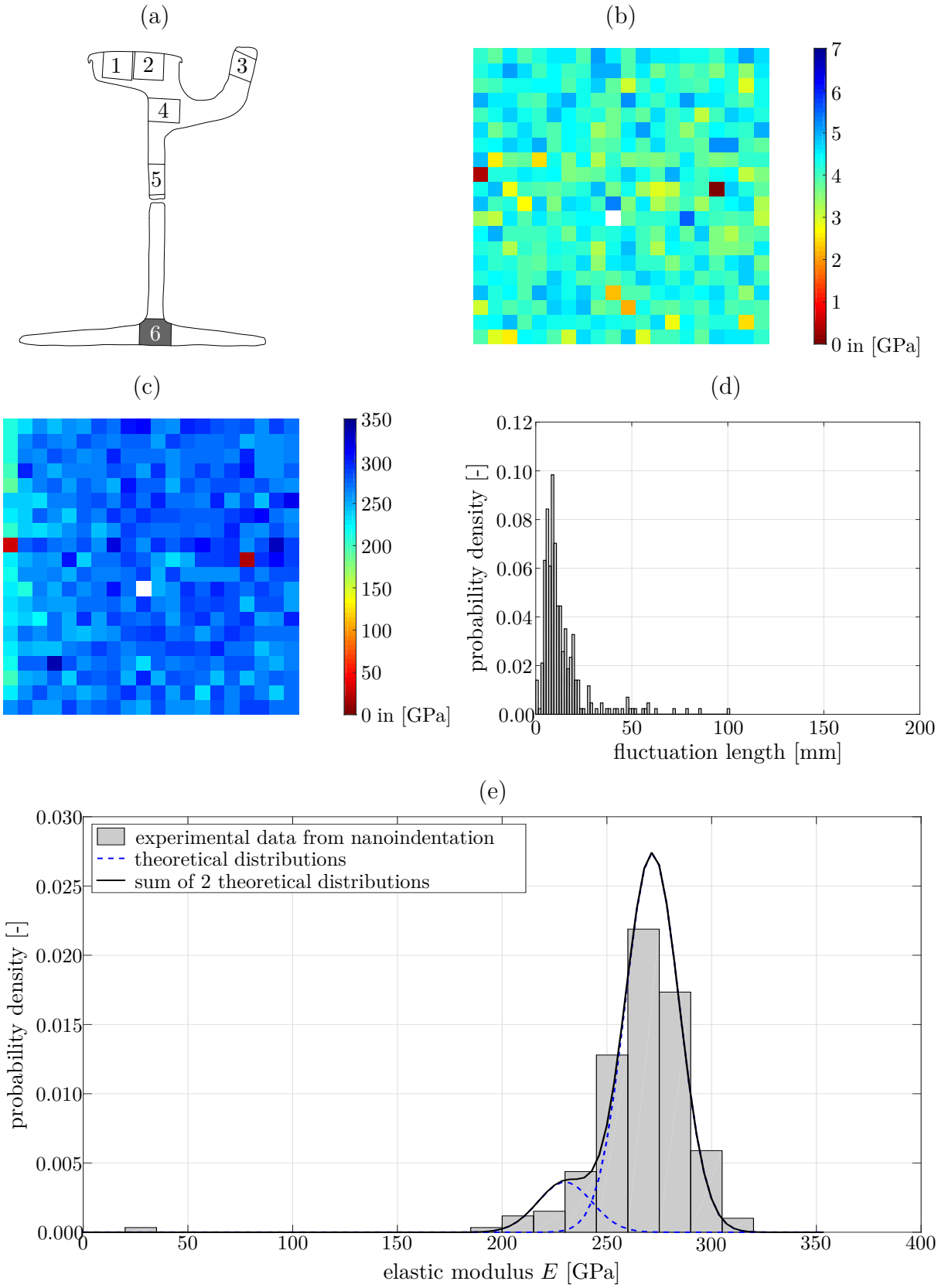

Fig. 4.43: Nanoindentation results for specimen VII-6; (a) definition of specimen position; (b) hardness and (c) Young's modulus distributions across the tested area; (d) histogram showing the fluctuation length of the Young's modulus; (e) probability density function of the Young's modulus, as well as fitting of the data by means of 2 Gaussian (theoretical) distribution

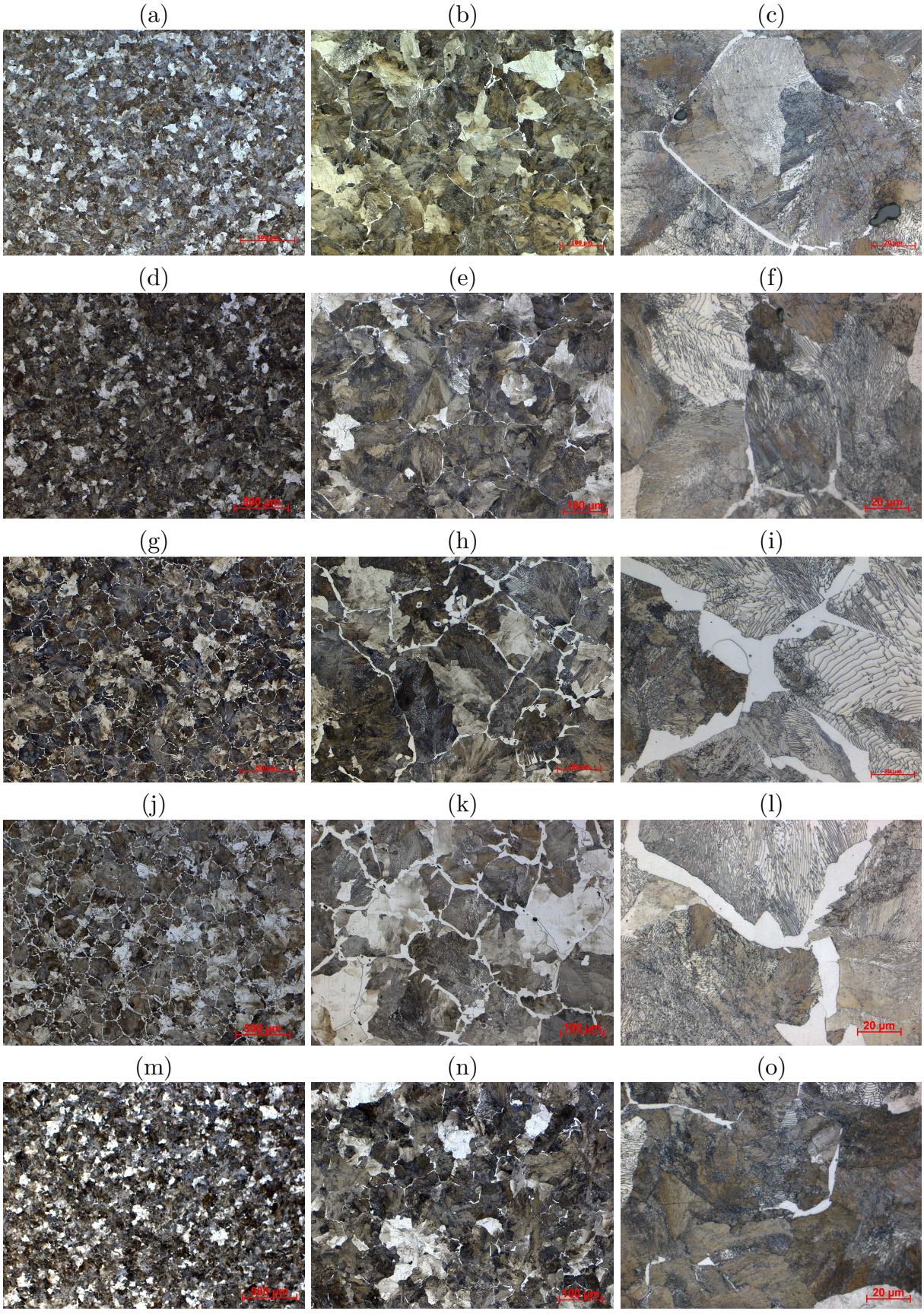

Fig. 4.44: Etched surfaces shown by light microscopy of specimen I-2 (a) – (c), of specimen II-2 (d) – (f), of specimen III-2 (g) – (i), of specimen IV-2 (j) – (l), and of specimen V-2 (m) – (o); all specimens are shown with 5-, 20-, and 100-fold magnifications

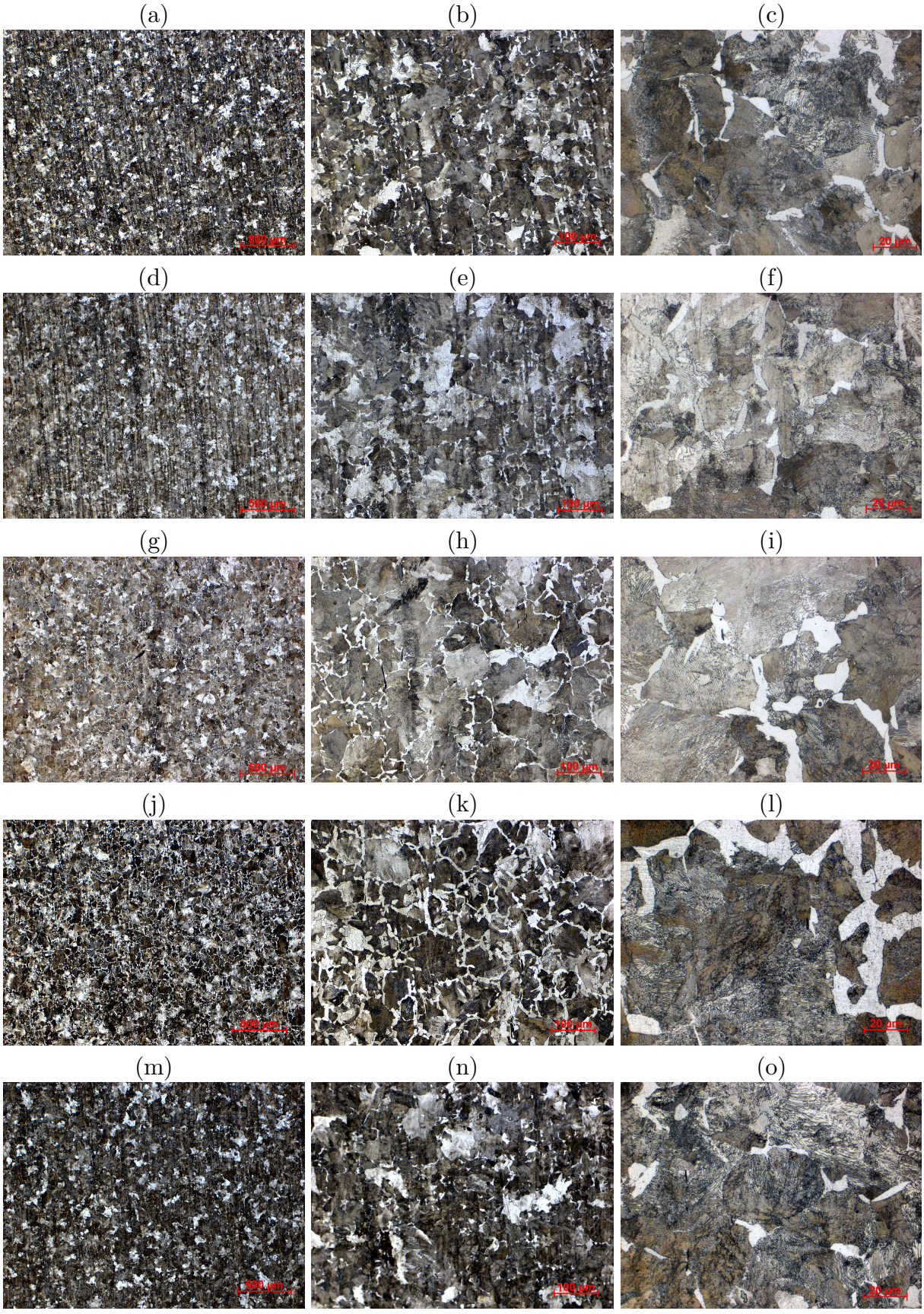

Fig. 4.45: Etched surfaces shown by light microscopy of specimen I-5 (a) – (c), of specimen II-5 (d) – (f), of specimen III-5 (g) – (i), of specimen IV-5 (j) – (l), and of specimen V-5 (m) – (o); all specimens are shown with 5-, 20-, and 100-fold magnifications

4.4 Difficulties arising during the experimental campaign

This section is devoted to elaborating on some difficulties that had to be overcome during performing the nanoindentations of this study. For example, Fig. 4.46 shows two typical load-displacement curves, which were encountered when indentation performed on the specimens. Both loading and unloading paths exhibit the expected behavior, and from

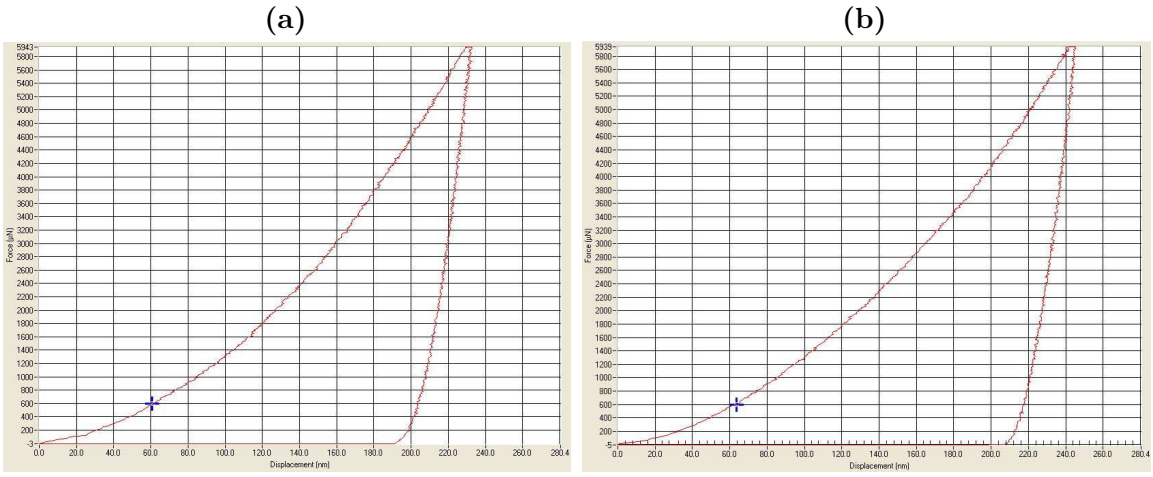

Fig. 4.46: Force displacement-curves of (a) the 33rd and (b) the 34th indent of specimen I-4

the tangent to the unloading paths reasonably Young's moduli could be back-calculated. Fig. 4.47 shows the load-displacement curves for all 400 indentations performed on specimen I-4. Obviously, while all curves are qualitatively similar, they slightly differ from each other, mainly due to varying inclinations of the loading paths.

However, considering, for example, specimen II-1, some indentations led to a rather peculiar behavior, see Fig. 4.48. Clearly, as discussed in Section 3.4.1, these outliers do not represent the stiffness of steel, but follow from disturbances in the experimental protocol, such as indentation into dust particles or similar. The number of outliers, due to that fact, per sample is, in most cases, very small - for specimen II-1, 1 % of all indentations lead to such outliers - their overall effect is negligible. On the other hand, Fig. 4.49 shows a load-displacement curve, which could not be used for calculation of a corresponding Young's modulus at all. The completely irregular behavior was probably caused by some kind of contamination. Such indentation was completely disregarded, and is reflected by white areas in some of the Young's modulus distribution, see, for example, Fig. 4.3. Fig. 4.50, in turn, shows continuous irregularities, which obviously do not relate to steel-like stiffness, but which can nevertheless be evaluated, yielding consequently a false Young's modulus. Such behavior can be explained by contaminations, which stick

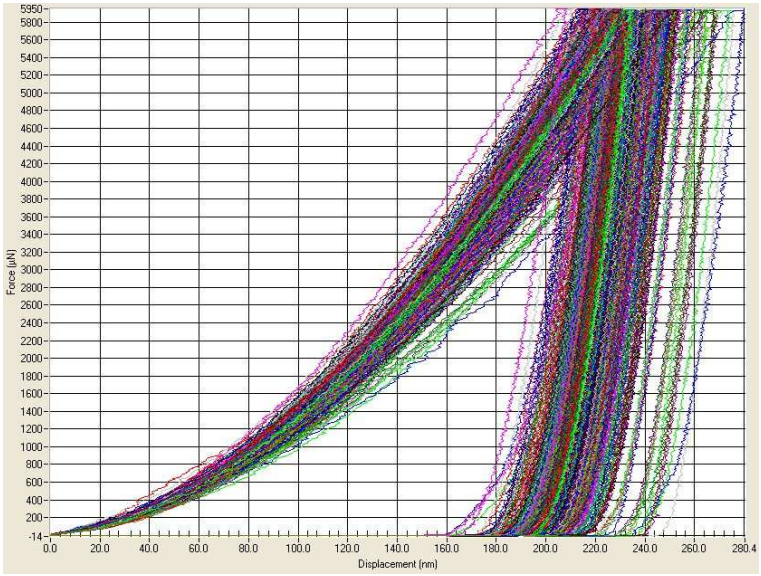

Fig. 4.47: All 400 load-displacement curves resulting from the indentations performed on specimen I-4

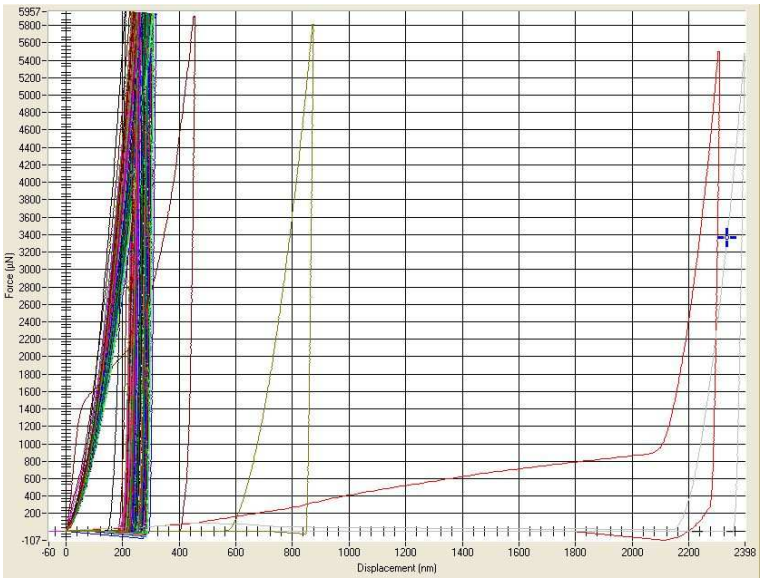

Fig. 4.48: All 400 load-displacement curves resulting from the indentations performed on specimen II-1, with 4 distinctive outliers

to the indenter tip, and thus completely distort the subsequent load-displacement curves. In such cases, the results were discarded and the specimen was tested again.

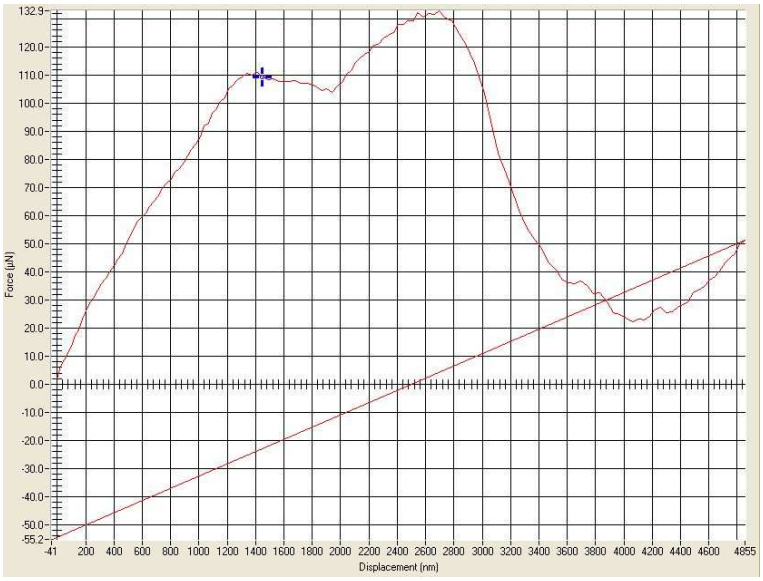

Fig. 4.49: Force-displacement curve (indentation number 96) of the sample II-1

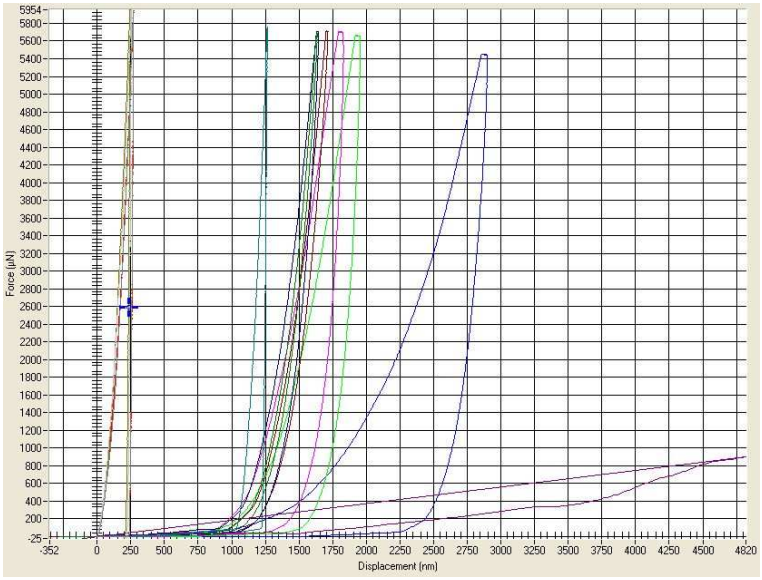

Fig. 4.50: Force displacement curves (indentation number 317 to 324) of the sample II-3

Chapter 5

Concluding remarks

Based on the nanoindentation testing campaign carried out in the course of the project leading to this thesis, some remarkable insights could be unraveled:

- For the first time, the stiffness of tramway rails was thoroughly tested instead of simply assuming some standard values.
- As also shown in previous works (Pham et al., 2014; Pham et al., 2015; Pham and Kim, 2015a; Pham and Kim, 2015b), nanoindentation gives access to the varying Young's moduli of the material phases contained in steel.
- Clear distinction between the material phases is however difficult – if the number of indentations is too low, statistical significance is not granted; if the number of indentations is too high, some kind of smearing effects leads to the apparent amalgamation of the phases in terms of their Young's moduli.
- No significant variations can be discerned between samples of different age, different history (in terms of maintenance works), or different locations.
- Thus, this study suggests that assuming that the stiffness of typical tramway steel is homogeneous and time-invariant is justified.
- The average stiffness across all tested specimens is $\approx 256\,\mathrm{GPa}$. Hence, tramway steel seems to be be considerably stiffer than typically assumed, namely by factor $(256 - 210)/210 \times 100 \approx 22\,\%$.

Bibliography

Akselsen, O., G. Rorvik, M. Onsoien, and O. Grong (1989). "Assessment and Predictions of HAZ Tensile Properties of High-Strength Steels". In: *Welding Research Supplement*, pp. 356–362.

Austrian Standards Institute (2010). *ÖNORM EN 14811 2010-05-01*.

Berkovich, E. (1951). "Three-faceted diamond pyramid for micro-hardness testing". In: *Industrial Diamond Review* 11.127, pp. 129–133.

Berns, H. (1993). *Stahlkunde für Ingenieure: Gefüge, Eigenschaften, Anwendungen*. 2nd ed. Berlin: Springer.

Bhadeshia, H. and R. Honeycombe (2006). *Steels: microstructure and properties*. 3rd ed. Amsterdam: Elsevier, Butterworth-Heinemann.

Boccaccio, A., M. Papi, M. De Spirito, L. Lamberti, and C. Pappalettere (2013). "Effect of the residual stress on soft sample nanoindentation". In: *Applied Physics Letters* 102.13, pp. 1–5.

Brenner, S. S. (1956). "Tensile Strength of Whiskers". In: *Journal of Applied Physics* 27.12, pp. 1484–1491.

Broitman, E. (2017). "Indentation hardness measurements at macro-, micro-, and nanoscale: a critical overview". In: *Tribology Letters* 65.1, pp. 1–18.

Chatterjee, A., M. Srivastava, G. Sharma, and J. Chakravartty (2014). "Investigations on plastic flow and creep behaviour in nano and ultrafine grain Ni by nanoindentation". In: *Materials Letters* 130, pp. 29–31.

Constantinides, G., K. Ravi Chandran, F.-J. Ulm, and K. Van Vliet (2006). "Grid indentation analysis of composite microstructure and mechanics: Principles and validation". In: *Materials Science & Engineering A* 430.1, pp. 189–202.

Constantinides, G. and F.-J. Ulm (2007). "The nanogranular nature of C–S–H". In: *Journal of the Mechanics and Physics of Solids* 55.1, pp. 64–90.

Dean, J., G. Aldrich-Smith, and T. W. Clyne (2011). "Use of nanoindentation to measure residual stresses in surface layers". In: *Acta Materialia* 59.7, pp. 2749–2761.

Debehets, J., J. Tacq, A. Favache, P. Jacques, J. W. Seo, B. Verlinden, and M. Seefeldt (2014). "Analysis of the variation in nanohardness of pearlitic steel: Influence of the interplay between ferrite crystal orientation and cementite morphology". In: *Materials Science and Engineering A* 616, pp. 99–106.

Doerner, M. and W. Nix (1986). "A method for interpreting the data from depth-sensing indentation instruments". In: *Journal of Materials Research* 1.4, pp. 601–609.

Furin, I., M.-I. Pastrama, H. Kariem, K. W. Luczynski, O. Lahayne, and C. Hellmich (2016). "A new nanoindentation protocol for identifying the elasticity of undamaged extracellular bone tissue". In: *MRS Advances* 1.11, pp. 693–704.

Gadelmawla, E., M. Koura, T. Maksoud, I. Elewa, and H. Soliman (2002). "Roughness parameters". In: *Journal of Materials Processing Technology* 123.1, pp. 133–145.

Gadelrab, K. R., G. Li, M. Chiesa, and T. Souier (2012). "Local characterization of austenite and ferrite phases in duplex stainless steel using MFM and nanoindentation". In: *Journal of Materials Research* 27.12, pp. 1573–1579.

Gulyaev, A. (1990). "On the iron-carbon diagram". In: *Metal Science and Heat Treatment* 32.7, pp. 493–494.

Hasslinger, P., A. Kurfürst, T. Hammer, E. Fischmeister, C. Hellmich, and S. Scheiner (2018). "Shear stress concentrations in tramway rails: results from beam theory-based, cross-sectional Finite Element analyses". In: *Engineering Structures*. In Revision.

Haušild, P., J. Nohava, and P. Pilvin (2011). "Characterisation of strain-induced martensite in a metastable austenitic stainless steel by nanoindentation". In: *Strain* 47.2, pp. 129–133.

Hellmich, C., M. Lukacevic, A. Dejaco, R. Blanchard, M. Shahidi, K. Luczynski, S. Scheiner, M. Königsberger, B. Pichler, V. Vass, M. Pastrama, and P. Godinho (2015). *Skriptum zur Vorlesung aus Festigkeitslehre*. Institut für für Mechanik der Werkstoffe und Strukturen, Technische Universität Wien.

Hernandez, B., S. Panda, M. Kuntz, and Y. Zhou (2010). "Nanoindentation and microstructure analysis of resistance spot welded dual phase steel". In: *Materials Letters* 64.2, pp. 207–210.

Hernandez, B., S. K. Panda, Y. Okita, and N. Y. Zhou (2010). "A study on heat affected zone softening in resistance spot welded dual phase steel by nanoindentation". In: *Journal of Materials Science* 45.6, pp. 1638–1647.

Hooke, R. (1678). *Lectures De Potentia Restitutiva, Or of Spring Explaining the Power of Springing Bodies*. London: John & Martin Printer to the Royal Society.

Hou, D., G. Zhang, R. R. Pant, J. S. Shen, M. Liu, and H. Luo (2016). "Nanoindentation characterization of a ternary clay-based composite used in ancient chinese construction". In: *Materials* 9.11, p. 866.

Hrivnak, I. (1992). *Theory of Weldability of Metals and Alloys*. Amsterdam: Elsevier.

Jäger, A. (2008). *Charakterisierung der viskoelastischen Eigenschaften von Bitumen mittels Nanoindentation als Grundlage für die Mehrskalenmodellierung von Asphalt*. Wien: Technische Universität Wien, Institut für Straßenbau und Straßenerhaltung.

Jaindl, M., A. Kostinger, C. Magele, and W. Renhart (2009). "Multi-objective optimization using evolution strategies". In: *Facta universitatis-series: Electronics and Energetics* 22.2, pp. 159–174.

Jirásková, Y., J. Svoboda, O. Schneeweiss, W. Daves, and F. D. Fischer (2005). "Microscopic investigation of surface layers on rails". In: *Applied Surface Science* 239.2, pp. 132–141.

Juliano, T. F., M. R. Van Landingham, T. Weerasooriya, and P. Moy (2007). *Extracting stress-strain and compressive yield stress information from spherical indentation*. Technical Report. Army research lab Aberdeen proving ground MD weapons and materials research directorate.

Kariem, H., M. I. Pastrama, S. I. Roohani-Esfahani, P. Pivonka, H. Zreiqat, and C. Hellmich (2015). "Micro-poro-elasticity of baghdadite-based bone tissue engineering scaffolds: A unifying approach based on ultrasonics, nanoindentation, and homogenization theory". In: *Materials Science and Engineering C* 46, pp. 553–564.

Kim, J., M. K. Rahman, and M. M. Reda Taha (2012). "Examining microstructural composition of hardened cement paste cured under high temperature and pressure using nanoindentation and 29Si MAS NMR". In: *Applied Nanoscience* 2.4, pp. 445–456.

Kim, S. A. and W. L. Johnson (2007). "Elastic constants and internal friction of martensitic steel, ferritic-pearlitic steel, and α-iron". In: *Materials Science and Engineering: A* 452, pp. 633–639.

Knott, J. F. (1973). *Fundamentals of Fracture Mechanics*. London: Butterworths.

Ladani, L., E. Harvey, S. F. Choudhury, and C. R. Taylor (2013). "Effect of varying test parameters on elastic-plastic properties extracted by nanoindentation tests". In: *Experimental Mechanics* 53.8, pp. 1299–1309.

Laurent-Brocq, M., E. Béjanin, and Y. Champion (2015). "Influence of roughness and tilt on nanoindentation measurements: A quantitative model". In: *Scanning* 37.5, pp. 350–360.

Lippold, J. C. (2014). *Welding Metallurgy and Weldability*. Hoboken: Wiley.

Ogi, H., T. Inoue, H. Nagai, and M. Hirao (2008). "Quantitative imaging of Young's modulus of solids: A contact-mechanics study". In: *Review of Scientific instruments* 79.5.

Oliver, W. and G. Pharr (1992). "An improved technique for determining hardness and elastic modulus using load and displacement sensing indentation experiments". In: *Journal of Materials Research* 7.11, pp. 1564–1583.

– (2004). "Measurement of hardness and elastic modulus by instrumented indentation: Advances in understanding and refinements to methodology". In: *Journal of Materials Research* 19.01, pp. 3–20.

Patnaik, S. N. and D. A. Hopkins (2004). *Strength of materials: A New Unified Theory for the 21st Century*. Amsterdam: Butterworth-Heinemann.

Pham, T., J. Kim, and S. Kim (2014). "Estimation of microstructural compositions in the weld zone of structural steel using nanoindentation". In: *Journal of Constructional Steel Research* 99, pp. 121–128.

– (2015). "Estimating constitutive equation of structural steel using indentation". In: *International Journal of Mechanical Sciences* 90, pp. 151–161.

Pham, T. and S. Kim (2015a). "Determination of mechanical properties in SM490 steel weld zone using nanoindentation and FE analysis". In: *Journal of Constructional Steel Research* 114, pp. 314–324.

– (2015b). "Nanoindentation for investigation of microstructural compositions in SM490 steel weld zone". In: *Journal of Constructional Steel Research* 110, pp. 40–47.

Pharr, G. and A. Bolshakov (2002). "Understanding nanoindentation unloading curves". In: *Journal of Materials Research* 17.10, pp. 2660–2671.

Pointner, P., A. Joerg, and J. Jaiswal (2006). *Definitive Guidelines on the Use of Different Rail Grades*. Technical Report of project TIP5-CT-2006-031415 Innovative Track Systems.

Ray, K. and D. Mondal (1991). "The effect of interlamellar spacing on strength of pearlite in annealed eutectoid and hypoeutectoid plain carbon steels". In: *Acta Metallurgica Et Materialia* 39.10, pp. 2201–2208.

Salençon, J. (2012). *Handbook of Continuum Mechanics: General Concepts Thermoelasticity*. Berlin: Springer Science & Business Media.

Schröder, R. (1985). "Influences on development of thermal and residual stresses in quenched steel cylinders of different dimensions". In: *Materials Science and Technology* 1.10, pp. 754–764.

Schwefel, H.-P. (1977). *Numerische Optimierung von Computer-Modellen mittels der Evolutionsstrategie*. Basel: Birkhäuser.

Sneddon, I. N. (1965). "The relation between load and penetration in the axisymmetric boussinesq problem for a punch of arbitrary profile". In: *International Journal of Engineering Science* 3.1, pp. 47–57.

Svensson, L.-E. (1994). *Control of Microstructures and Properties in Steel Arc Welds*. Boca Raton, Fla.: CRC Press.

Totten, G. E. (2008). *Handbook of Residual Stress and Deformation of Steel*. 3rd ed. Materials Park, Ohio: ASM International.

Ulm, F.-J., M. Vandamme, C. Bobko, J. Alberto Ortega, K. Tai, and C. Ortiz (2007). "Statistical indentation techniques for hydrated nanocomposites: concrete, bone, and shale". In: *Journal of the American Ceramic Society* 90.9, pp. 2677–2692.

Wang, X. F., X. P. Yang, Z. D. Guo, Y. C. Zhou, and H. W. Song (2007). "Nanoindentation characterization of mechanical properties of ferrite and austenite in duplex stainless steel". In: *Advanced Materials Research* 26-28, pp. 1165–1170.

Weicker, K. (2007). *Evolutionäre Algorithmen*. 2nd ed. Wiesbaden: Springer.

Weißbach, W. (2012). *Werkstoffkunde: Strukturen, Eigenschaften, Prüfung*. 18th ed. Wiesbaden: Vieweg + Teubner Verlag.

Zhu, L. N., B. S. Xu, H. D. Wang, and C. B. Wang (2010). "Measurement of residual stress in quenched 1045 steel by the nanoindentation method". In: *Materials Characterization* 61.12, pp. 1359–1362.